Statistical Techniques and Non-Destructive Testing Methods for Copper Wire Bond Reliability Investigation

by

Michael David Hook

A thesis
presented to the University of Waterloo
in fulfillment of the
thesis requirement for the degree of
Doctor of Philosophy
in
Mechanical Engineering

Waterloo, Ontario, Canada, 2018

Examining Committee Membership

The following served on the Examining Committee for this thesis. The decision of the Examining Committee is by majority vote.

External Examiner: Patrick McCluskey
Professor, Dept. of Mechanical Engineering,
University of Maryland

Supervisor(s): Michael Mayer
Associate Professor, Dept. of Mechanical
and Mechatronics Engineering,
University of Waterloo

Internal Member: Grzegorz Glinka
Professor, Dept. of Mechanical and Mechatronics Engineering,
University of Waterloo

Internal-External Member: Shoja'eddin Chenouri
Associate Professor, Dept. of Statistics and Actuarial Science,
University of Waterloo

Other Member(s): Mustafa Yavuz
Professor, Dept. of Mechanical and Mechatronics Engineering,
University of Waterloo

This thesis consists of material all of which I authored or co-authored: see Statement of Contributions included in the thesis. This is a true copy of the thesis, including any required final revisions, as accepted by my examiners.

I understand that my thesis may be made electronically available to the public.

Statement of Contributions

Section 1.7 of this thesis contains material to be published in [1], which was co-authored with Stevan Hunter and Michael Mayer and used with the publisher's permission. Chapter 2 was modified from [2] with the publisher's permission; the original manuscript was co-authored with Michael Mayer.

Abstract

Microelectronic devices require packaging for mechanical protection and electrical interconnections. Reliability challenges in microelectronics packaging are becoming more severe, as applications demand smaller package sizes and operation in harsher environments, such as in automotive applications. At the same time, manufacturers are seeking to reduce production costs by using new materials, for example in wire bonding by replacing costly gold wire with more economical copper.

Because microelectronic devices are expected to function reliably for years or even decades, depending on the application, reliability testing is commonly accelerated, e.g. by using elevated temperature and/or humidity. Even so, testing is often time consuming, requiring weeks or months for product qualification. Furthermore, although standard test conditions exist, little guidance is available in the literature to indicate how long products passing these tests will survive in operation.

Non-destructive testing methods provide a great deal of information regarding product degradation and reliability. With proper statistical analysis, strong conclusions can be made about device reliability with relatively short test durations, since testing need not continue until all samples fail. However, data analysis techniques used in the electronics packaging literature are often limited, with statistical analyses and confidence bounds rarely presented. Analysis of incomplete or censored data requires specialized techniques from the field of survival analysis.

The contributions of this thesis can be divided in two topics. The first topic is the equipment and techniques used to obtain new reliability results, including a method for temperature calibration of the miniature ovens used, a modification of those ovens for use as environmental chambers with humidity control, and procedures for optimization of wire bonding processes.

Second, statistical techniques for analysis of reliability data are demonstrated, using accelerated failure time models to analyze resistance data from copper wire bonds in high temperature storage testing. In doing so, new information was provided to answer an important open question in the field of copper wire bonding, namely, the maximum temperature at which one can expect copper wire bonds on aluminum metallization to perform reliably.

In particular, ball bonds made from 25 µm diameter palladium-coated copper wire are estimated to be highly reliable up to at least 167 °C in a clean environment without encapsulation, with failure rate of only 1 ppm after 12000 h. PCC wires were more reliable than bare Cu wires when unencapsulated or when encapsulated in silicone. Conversely, bare Cu was more reliable than PCC when encapsulated in epoxy. The best-performing encapsulated bonds tested were bare Cu wire with a highly heat tolerant epoxy, which are estimated to survive 12000 h with 1 ppm failure probability at 159 °C.

Effects of several other factors on bond reliability were also investigated, namely the cleaning process, Al bond pad thickness, and the bonded ball size. Sample and environmental cleanliness were found to be critical to good reliability. Bond pad thickness and bonded ball size had only minor effects on reliability, suggesting that these factors can be safely chosen to satisfy other requirements such as bond pad pitch or current-carrying requirements.

Acknowledgements

I am grateful to my supervisor, Professor Michael Mayer, for his guidance and support, and likewise to Dr. Stevan Hunter for motivating and guiding this work.

I also thank the following colleagues for their assistance. For Chapter 1, Nhat Ly assisted in preparing the ball bond cross-section image in Fig. 1.4. For Chapter 2, Nicholas Henriques assisted in soldering the humidity sensors. Ruijian He the designed and produced the aluminum cups with larger internal volumes, as well as the punch and die used to cut the sealing gaskets and graphite thermal interface pads. For Chapter 4, Wang Shuyue, Jang Baeg Kim, and Nicholas Kam assisted in preparing sample cross-sections. The photograph in Fig. 4.25 was taken by Nicholas Kam.

I thank the National Science and Engineering Research Council (NSERC), AMI Semiconductor Canada Company, and Microbonds, Inc for financial support, and ON Semiconductor, MG Chemicals, Wacker Chemie AG and Microbonds, Inc. for material support.

Finally, I thank my always supportive family, especially my parents, Vickie Hook and David Hook, my parents-in-law, Sue Klassen and Victor Klassen, and most of all my spouse, Sylvia Hook, for abundant emotional and practical support.

Table of Contents

List of Tables

List of Figures

Chapter 1

Introduction

1.1 Wire Bonding Process Description

Wire bonding is the most common technique used for first-level electronic packaging, i.e. making electrical connections between a semiconductor die and external circuitry [3, 4]. Fig. 1.1 shows a schematic of a simple electronic package, consisting of a die attached to a substrate or leadframe, with wire bonds between the substrate terminals or leadfingers. The die and wires are encapsulated in a polymer resin for mechanical and chemical protection. Packages of this type are typically made using processes categorized as first-level packaging. Subsequently, the packages are soldered to printed circuit boards for use in larger and more complex electronic devices; this process is known as second-level packaging.

There are two distinct wire bonding processes, known as ball-wedge bonding and wedge-wedge bonding. This thesis focuses on ball-wedge bonding, which is more commonly used due to lower equipment costs and higher throughput [3]. Specifically, the focus is on the ball bond step, without study of the wedge bond or other portions of the process.

Fig. 1.2 illustrates the ball-wedge bonding process. The process begins with a short segment of wire, known as a tail, protruding through the capillary tool. A high voltage applied to an electrode discharges through the tail, ionizing the air nearby. This discharge generates enough heat to melt part of the tail, forming a sphere known as a free air ball (FAB) at its tip. This step is called the electric flame-off (EFO). When using copper or silver wires, ambient oxygen causes oxidized and misshapen FABs, so a shielding gas of nitrogen or a nitrogen-hydrogen mixture,

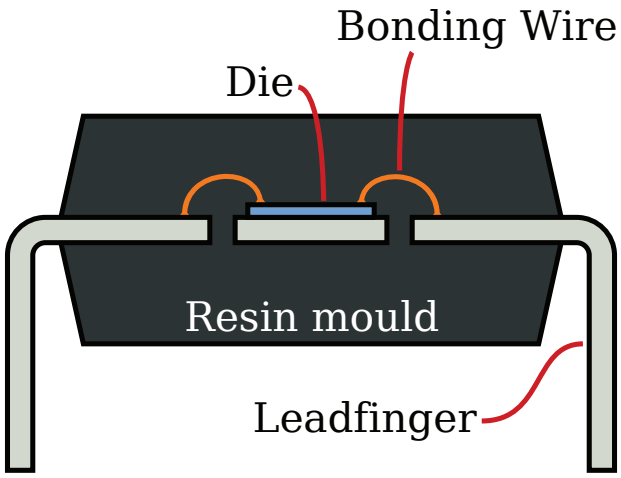

Fig. 1.1: Schematic of simple dual in-line package (DIP). Wire bonds make electrical connections between the semiconductor die and metallic leadframe. Modified from [5], original in public domain.

typically 5 % hydrogen, is directed toward the tail throughout the process. Next, the capillary moves to the first bond location, impacting with enough force to plastically deform the FAB to approximately its final shape. Then, while applying a smaller and constant downward force, the capillary vibrates ultrasonically in a horizontal direction to push away oxides and impurities at the bonding interface, exposing pure metal and forming a strong metallic bond. This first bond is called the ball bond, and is most often made on an aluminum bond pad of the semiconductor die. With the end of the wire now fixed in place, the capillary moves to the next bond location while bending the wire into the desired loop shape and allowing additional wire to pass through the capillary as needed. The second bond, known as a wedge bond or crescent bond, is made using a similar combination of impact followed by constant force with ultrasonic vibration. Once the wedge bond is complete, the capillary rises slightly, allowing a short section of wire to pass through to form a new tail. The clamp above the capillary pulls upward to break the wire away from the substrate, and the process is ready to be repeated [3].

An ESEC 3088 (ESEC now part of BE Semiconductor Industries N.V., Duiven, The Netherlands) automatic ball bonder, shown in Fig. 1.3 was used for all wire bond processes described in this thesis.

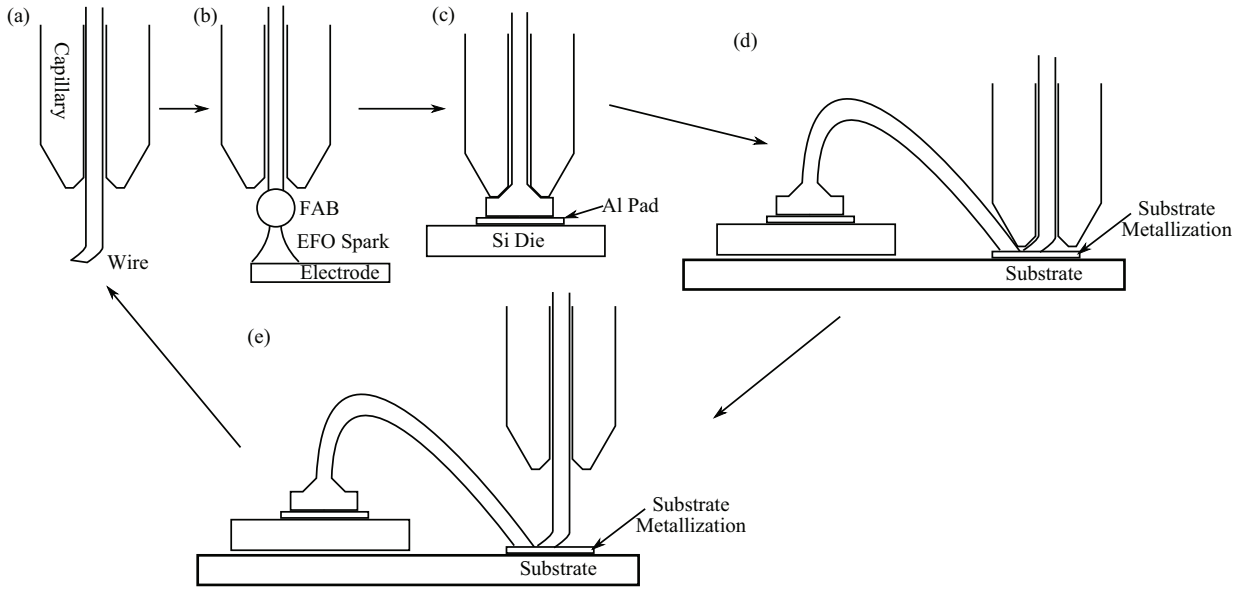

Fig. 1.2: Schematic of ball-wedge bonding process cycle. (a) Capillary with protruding wire tail. (b) Electric flame-off (EFO) spark melts tip of wire tail to form free air ball (FAB). (c) Ball bond formation. (d) Wire looping and wedge bond formation. (e) Tail formation.

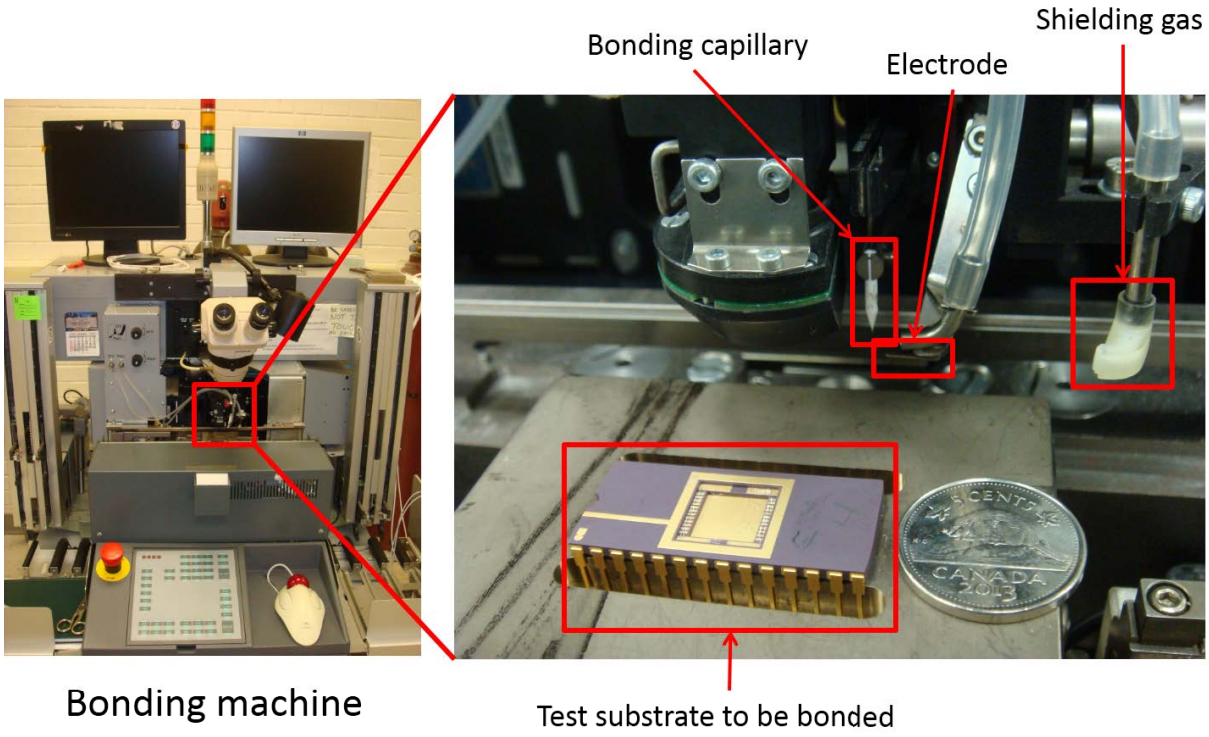

Fig. 1.3: Photographs of ESEC 3088 automatic ball bonder.

1.2 Motivation

1.2.1 Expanding Copper Wire Bond Applications

Cu wire is much less expensive than Au, so significant cost savings are possible by changing materials. Ref. [6] estimated a total packaging cost of US$0.86 for typical device with Au bond wires, including a wire cost of $0.28, corresponding to 550 mm of 25 µm wire at a typical 2018 price of $40/g. By comparison, the cost for a similar copper wire bonded device is estimated to be $0.70. The difference arises from a reduction of approximately $0.21 in wire cost, partly offset by an increase of $0.04 in other costs of the bonding process, such as the shielding gas required. Al wire is also available at low cost, but is limited to the wedge-wedge bonding process, so its use in high-volume production is limited [3]. Ag-based wires, including Ag alloys [7–20] and Pd-coated Ag [21–23], have generated major interest in recent years, with many promising results. These wires also cost much less than Au wire, but have not been widely adopted. In 2016, Ref.

[24] forecasted that, of about $26 \cdot 10^9$ m of bond wire used worldwide in 2017, 16 % would be Au, 11 % Ag, 6 % Al, 45 % Pd-coated Cu (PCC), and 22 % Cu.

Cu also has a reliability advantage in many situations. Compared to Au-Al or Ag-Al bonds, Cu-Al bonds form intermetallic compounds more slowly at high temperatures [25–28]. Furthermore, Cu-Al bonds are less vulnerable to Kirkendall voiding [27, 29]. Higher shear and pull strengths are also achievable with Cu wire than with Au wire [25].

Given the slow intermetallic growth, it may be possible to use Cu wire bonds on standard Al pads for high temperature applications, such as those required in the automotive industry. However, reported Cu bond lifetimes vary widely, and there is no consensus regarding a maximum reliable temperature.

1.2.2 Improve Methods for Reliability Characterization

Typical ball bond reliability studies in the literature report the aging condition and number of failures observed, possibly including physical analysis to identify failure modes [25, 30, 31]. Less commonly, samples may be tested in multiple aging conditions, with the results fitted to a mathematical model [32–34]. However, detailed statistical analyses of results, including systematic extrapolation techniques and confidence intervals for model parameters or failure probabilities are rarely reported in the literature relating to microelectronic reliability. In particular, predictions of maximum operating temperature are missing. It is a goal of this thesis to remedy this situation, clearly describing published methods from the statistical field of survival analysis and applying them to copper ball bond reliability data as one sample application.

1.3 Objectives

The following are the objectives chosen for this thesis:

1. Expand capabilities of UW-CAMJ Reliability Test Station
    (a) Enable humidity testing
    (b) More accurate temperature control
2. Develop improved procedures for ball bond process optimization
    (a) Include statistical methods to assess confidence in results
    (b) Enable optimization of additional parameters and responses, particularly to minimize Al bond pad splash

3. Determine effects of five parameters on Cu bond reliability at elevated temperatures:
    (a) Cleaning procedure
    (b) Al bond pad thickness
    (c) Encapsulant type
    (d) Pd coating on Cu wire
    (e) Ball bond diameter
4. Predict lifetimes for Cu ball bonds on Al pads at a elevated temperature. Equivalently, predict maximum operating temperature for Cu bonds, given a particular lifetime requirement.

1.4 Literature Study

1.4.1 Technologies and Standards for Reliability Assessment

There are three types of environmental tests in common use for evaluating wire bond reliability. These are known as high temperature storage (HTS), thermal cycling, and temperature-humidity.

HTS accelerates diffusion and the formation of intermetallic compounds (IMCs) between dissimilar metals. Au-Al bonds that are poorly welded or have impurities at the bonding interface can fail rapidly as a result, making it a good test for contaminants or poor welding for Au bonds. Temperatures range from 150 °C to over 400 °C, with times from 1 h at very high temperatures to 3000 h at lower temperatures [3]. JEDEC standard JESD-A103C [35] specifies 1000 h at temperatures of 125, 150, 175, 200, 250, 300, or 85 °C. Temperatures from 150 °C to 175 °C are common in recent publications [12, 14, 16, 23, 36].

The document AEC Q-100, published by the Automotive Electronics Council defines a set of standard reliability test conditions for Cu wire bonds [37]. For high temperature operation, four grades are defined; passing the test conditions for Grade 0, 1, 2, or 3 qualifies a device for operation at 150 °C, 125 °C, 105 °C, or 85 °C. The corresponding test conditions for encapsulated devices are:

- Grade 0: 175 °C for 1000 h or 150 °C for 2000 h
- Grade 1: 150 °C for 1000 h or 175 °C for 500 h
- Grades 2 and 3: 125 °C for 1000 h or 150 °C for 500 h

Other tests, such as temperature cycling and humidity testing are also required by the standard. The standard does not indicate durations that bonds are expected to survive at their maximum rated temperatures, though a time of 12000 h is given as an example, and is taken in Chapter 4 of this thesis as a target wire bond lifetime.

Thermal cycling also accelerates intermetallic growth and produces cyclic thermomechanical stresses that reveal brittle intermetallic compounds, since these cannot deform plastically to relieve stresses caused by thermal expansion and contraction. A total of 1000 cycles between -55 °C and 125 °C is one common condition in recent publications [36, 38] and is one of the options specified by JEDEC standard JESD22-A104D [39].

Temperature-humidity testing, often combined with electrical biasing, provides information about the cleanliness and corrosion-resistance of packaging materials, since the presence of water accelerates corrosion by ions such as Cl^- [40–42]. Early tests were performed in saturated conditions, i.e. 100 % relative humidity (RH), such as the boiling water test at 100 °C and 100 % RH and pressure cooker tests at about 120 °C and 100 % RH. Unsaturated conditions are now preferred, since they more closely simulate real operating conditions [41]. Testing is now commonly performed at 85 % RH, such as in the standard "85/85" test at 85 °C [41] and the highly accelerated stress test (HAST), with temperatures above 100 °C, often 130 °C and 85 % RH [40, 41, 43–45]. JEDEC standard JESD22-A101C [46] specifies 1000 h at 85 °C and 85 % RH; JESD22-A110-B [47] specifies 96 h at 130 °C and 85 % RH or 264 h at 110 °C and 85 % RH.

This thesis primarily considers and present data from HTS testing, but also presents a system developed for temperature-humidity testing in Section 2.1, with test results in Section 4.5.

1.4.2 Assessments of Bond Quality

Assessments of bond quality are needed in combination with the environmental tests above, to determine how the bonds are affected by the harsh environmental conditions and identify the times when failures occur. These measurements are divided into destructive and non-destructive types. The three common destructive types are the shear test, pull test, and cross-sectioning.

The shear test uses a stiff, flat-faced tool, positioned just above the chip surface, to apply horizontal force to the ball bond until it fails. The shear strength, calculated as the peak shear force divided by the area of the bonded ball, is a standard indicator of ball bond quality. Visual examination of the fracture surface also indicates the weakest part of the system. For example, the bond pad can lift from the chip, which may indicate poor pad adhesion. The failure mode for good-quality Au ball bonds is by shearing through the ball, leaving a layer of Au behind. Cu bonds in contrast, fail in the Al layer, without copper residue.

The pull test uses a hook placed under the wire loop and pulled vertically upward until the wire fails. It is useful for measuring wedge bond quality, but less useful for ball bonds, because the heat-affected zone just above the ball is normally weaker than the bond itself, so the test provides little information about the bond interface [3]. The pull test can also be used non-destructively,

Cross-sectioning, followed by high-resolution optical or electron microscope imaging, is important for understanding metallurgical changes that happen at the bond interface. In this way, the thicknesses of intermetallic layers can be measured, and their compositions can be determined by energy-dispersive X-ray spectroscopy (EDS). A typical cross-section image of a Cu ball bond on Al is shown in Fig. 1.4. Cross-section images are valuable for identifying bond failure mechanisms, as explained further in Section 1.4.3.

Many non-destructive bond quality measurements allow continuous monitoring, giving insight into different stages of bond degradation and allowing failure times to be determined precisely. Such methods include electrical resistance measurements of the bond, and stress sensors integrated into the semiconductor chip [48, 49].

Many configurations for resistance measurements are possible. One key distinction is between the two-wire and four-wire types. In a two-wire measurement, a current source applies a fixed current through the sample, and a voltmeter measures the resulting voltage difference between the terminals of the current source [50]. The major disadvantage of this method is that the measured

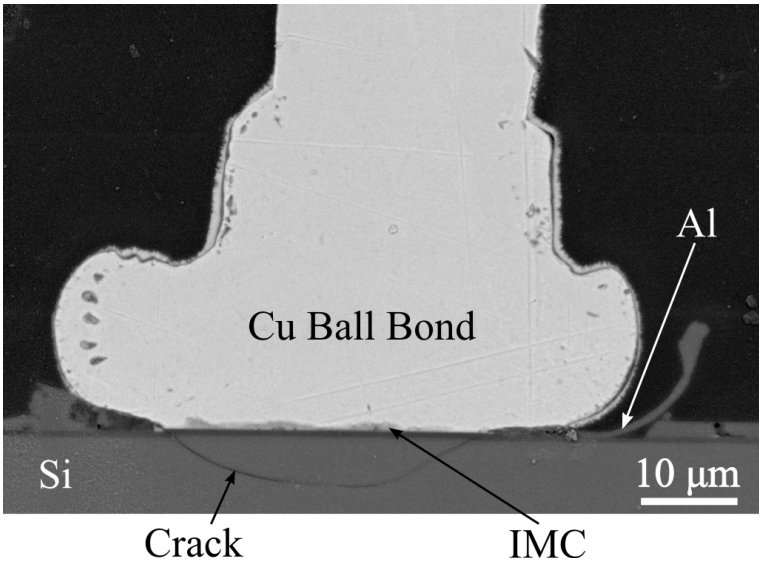

Fig. 1.4: Scanning electron microscope image of cross-section of palladium-coated Cu ball bond on Al pad over Si after HTS for 48 h at 220 °C. Crack in Si likely formed during bonding due to high force or US power. Intermetallic layer formed by HTS conditions.

value is the sum of all electrical resistances in the circuit, including the external wires connecting the meters to the sample. Thus, the true value of the wire bond resistance is unknown, and only changes in its value are observable. Furthermore, changes in other parts of the circuit, such as changes in the external wiring caused by fluctuations in ambient temperature, may mask the signals of interest or cast doubt on their validity.

A four-wire measurement avoids these problems by using four electrical connections, only joined together as close as possible to the sample. A fixed current flows through one pair of wires, and voltage is measured between the other two wires. This technique is insensitive to the resistance of the external wires, because very little current, typically 10 nA or less, flows through voltage measurement wires, meaning no significant potential difference arises along these wires [50]. This thesis uses exclusively the four-wire technique for resistance measurements.

Electrical measurements also differ in the portion of the wire included in the circuit. Most in this thesis measure two wires in series. Section 4.8 describes a novel arrangement used to test only the centre portion of each wire, excluding the interface resistances of both the ball and wedge bonds. Alternatively, a double ball bond technique has been used to measure the immediate vicinity of the ball bond, including only the intermetallic layer and small contributions from the bonded ball and the chip metallization [51].

1.4.3 Failure Mechanisms

The goal of this thesis is not to offer a detailed explanation of the physical and chemical processes by with Cu-Al wire bonds degrade and eventually fail. As this section demonstrates, such mechanisms have already been studied extensively, with the evidence suggesting that multiple different mechanisms are at work, so that no single explanation is sufficient. Sulfur or halogen contamination, intermetallic compound growth, and atmospheric oxygen each appear to contribute to bond failures under some conditions. Instead of offering an explanation for these observations, this work seeks to characterize high-temperature Cu-Al bond reliability empirically, identifying factors that influence bond lifetimes and estimating bond lifetimes given an operating temperature and values for the various process factors.

There have been many published studies examining Cu-Al bond reliability in HTS [27, 28, 34, 52–55], humid conditions [42, 56–59], or both [25, 29, 40, 60–62]; here the focus is on HTS behaviour. In HTS conditions, Cu-Al bonds form the intermetallic compounds (IMCs) identified in the phase diagram of Fig. 1.5. Most commonly, the compounds observed are $CuAl_2$, CuAl, and Cu_9Al_4, with the Al-rich $CuAl_2$ most abundant initially, and the copper-rich Cu_9Al_4 becoming more abundant as the Al of the bond pad is consumed.

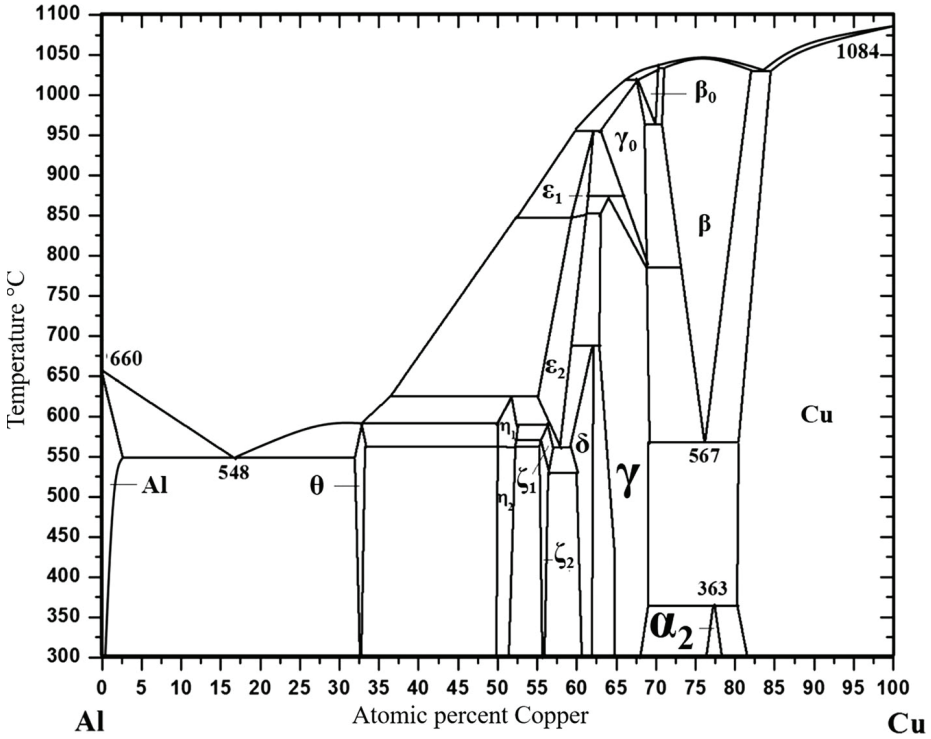

Fig. 1.5: Cu-Al phase diagram. Phases commonly observed at Cu-Al wire bond interfaces are θ: $CuAl_2$, η: CuAl, and γ: Cu_9Al_4. Ref. [63] also observed α_2: Cu_3Al. Reprinted by permission from Springer Journal of Electronic Materials [63], 2018.

When failures have been observed in Cu ball bonds on Al pads, bond cross-sections have commonly revealed cracks between the Cu ball and the Cu-Al IMC layer [27, 34, 54, 64, 65]. Small voids are also frequently observed in the IMC layer. Ref. [64] tested encapsulants with varying levels of sulfur content at 175 °C. They observed bond interface cracking for the higher-sulfur samples, and attributed the cracks to sulfur contamination found at the in the cracks and in voids at the Cu surface. Ref [66] proposed a mechanism of galvanic corrosion of PCC wires, forming voids at the surface of the Cu and at the Cu-Al interface. This corrosion is hypothesized to be activated by sulfur in encapsulants, with the Pd acting as the cathode and the Cu as the anode. Similarly, [67] also reported interface cracking, with the bond lifetime inversely related to the Cl content in the encapsulant.

Ref. [34] also reported cracking at the Cu-Al interface for encapsulated bonds. Similar to Section 4.6, they used bond lifetime data to fit an Arrhenius model based on a log-normal failure distribution, and obtained an activation energy of 0.7 eV. Refs [54] and [27] used the same analysis technique and found an activation energies of 0.91 eV and 0.85 eV, for bare Cu and PCC wire,

respectively. Using different techniques, others have reported activation energies from 0.46 eV [68] to 1.26 eV, estimated in [69] from IMC growth rates.

Using x-ray diffraction, [63] studied Cu-Al interfaces aged at 350 °C and 450 °C and observed evidence of an additional IMC phase, Cu_3Al, also observed using transmission electron microscopy in [70]. Ref. [63] concluded that Cu_3Al forms after Cu_9Al_4. Using x-ray diffraction, they concluded that this new phase has a larger equilibrium lattice spacing than the adjacent bulk Cu, so a strain develops at the interface, with Cu_3Al being under compression, and bulk Cu under tension. As the Cu_3Al layer thickens, the interfacial strain increases until the bond eventually fails, producing a crack as seen in Fig. 1.6.

Ref. [55] tested unencapsulated Cu bonds on cleaned Al pads in an N_2 atmosphere, with temperatures from 175 °C to 300 °C. The IMCs developed at the interface were typical of Cu-Al bonds, with $CuAl_2$, CuAl, and Cu_9Al_4 identified. Bond shear strength was consistently high, even after 1000 h at 250 °C and 50 h at 300 °C, with no cracks observed in cross-sections. These results suggest that Cu-Al bonds can be reliable at extreme temperature in a contaminant-free and oxygen-free environment. However, the lack of encapsulation and the nitrogen atmosphere are not representative of cost-effective mass-produced devices, which are exposed to atmospheric oxygen and are encapsulated for mechanical protection, with the encapsulant acting as a source of contamination.

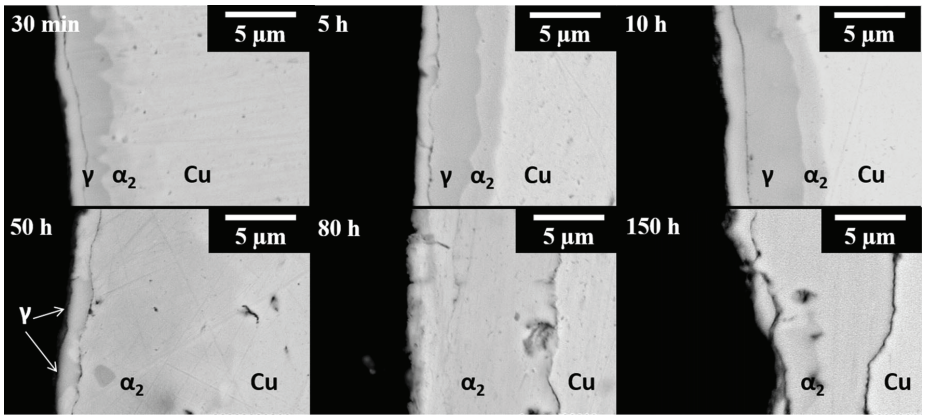

Fig. 1.6: SEM cross-section images, showing growth of Cu-Al IMCs at 450 °C. Cu_3Al (α_2) phase grew over time, producing interfacial stress and eventually a crack between the Cu and Cu_3Al phases. Reprinted by permission from Springer Journal of Electronic Materials [63], 2018.

1.5 Existing Lab Equipment

1.5.1 Mini-Ovens

Previous members of the research group developed small ovens, called mini-ovens, capable of performing HTS and TC with peak temperatures up to 200 °C [71, 72]. An example mini-oven is shown in Fig. 1.7. They are well-suited to performing non-destructive monitoring of bond quality, such as electrical resistance measurements and mechanical stress measured by on-chip sensors. Forty such ovens are available in the lab, 30 of which are divided between three racks. One of these racks is shown in Fig. 1.8. Each rack is capable of controlling 10 oven temperatures independently and performing a wide variety of electrical measurements with continuous data logging.

These ovens use a central heater block, made of a square copper tube with an outer ceramic coating, into which is embedded a resistive heating wire. Applying current to the wire yields

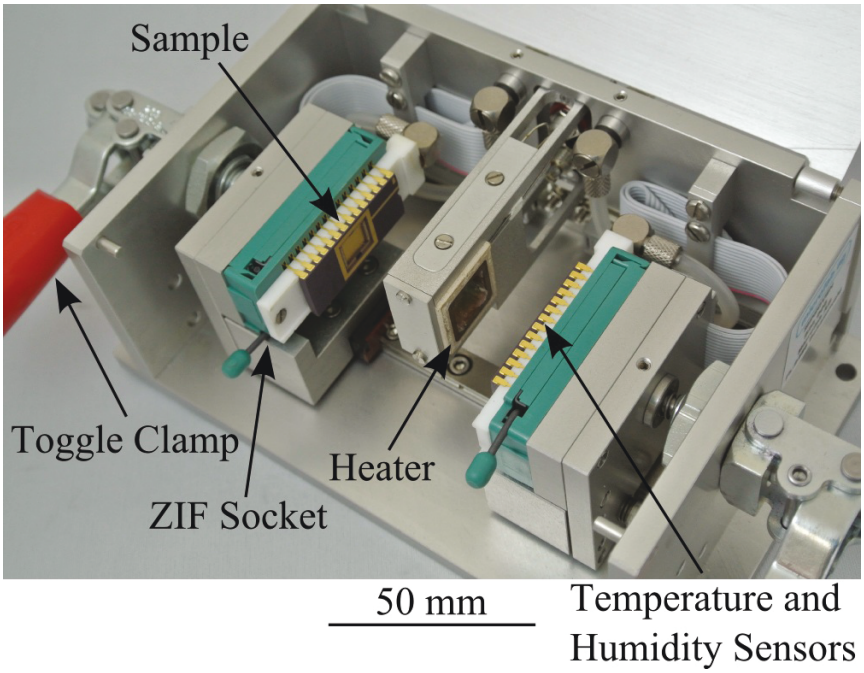

Fig. 1.7: Mini-oven with clamps open. Pt100 temperature sensor placed on right side of oven, allowing feedback control of temperature. Wires to be tested bonded to left-side substrate. Zero insertion force (ZIF) sockets hold substrates in place and make electrical connections. Own work, reproduced from [2].

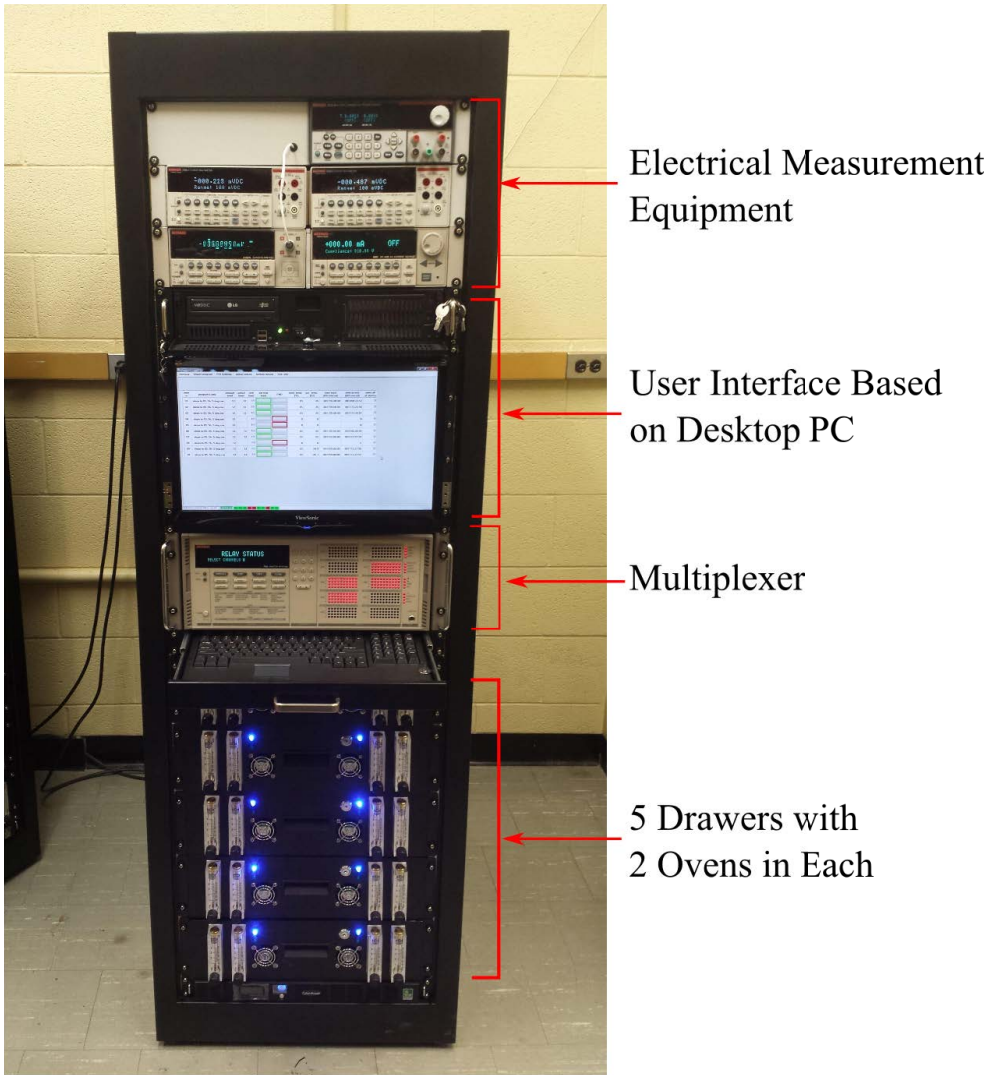

Fig. 1.8: UW custom-developed Reliability Test Station: each drawer contains 2 mini-ovens, for a total of 10. A programmable logic controller and adjustable DC power supplies allow temperature control of all ovens in parallel, and electrical equipment with multiplexers allow measurements of standard electrical properties of any sample.

temperatures up to 200 °C. Two ceramic test substrates are placed against the heater block, and held in place by toggle clamps. All 28 leads of the ceramic substrates are made available for electrical measurements and biasing during testing. Since the design is symmetric, both substrates remain at nearly the same temperature at all times. The temperature of the sample of interest, on

one side, is determined using a Pt100 resistive temperature detector that is installed on the other side. A Pt100 sensor consists of a thin film of Pt, constructed such that its resistance at 0 °C is 100 Ω to high precision. The resistance change of Pt is a well-characterized and nearly linear function of temperature, so a four-wire measurement of the Pt film's resistance can be converted to measurement of temperature. Fig. 1.9 shows a photo of one of the Pt100 sensors on its ceramic substrate.

1.6 Statistical Methods for Process Development

1.6.1 Definition of Linear Regression Model

In Chapter 3, linear models are used to describe the effects of bond process parameters such as impact force and ultrasonic power on process responses such as bonded ball diameter or shear strength. This section describes statistical procedures used to fit such models. These are published, for example, in [73, 74]. Methods are also described for generating confidence intervals for important model outputs, such as mean responses or optimized process parameters. Many software packages include implementations of these calculations, such as the MATLAB function fitlm or the Octave function LinearRegression.

In general, a linear model can be written as

$$\boldsymbol{y} = \boldsymbol{X}\boldsymbol{\beta} + \boldsymbol{\epsilon}, \tag{1.1}$$

with $\boldsymbol{y}$ an (n $\times$ 1) vector of observations, $\boldsymbol{X}$ an $(n \times p)$ matrix of independent variables, $\boldsymbol{\beta}$ a $(p \times 1)$ vector of coefficients, and $\boldsymbol{\epsilon}$ an $(n \times 1)$ vector of independent and identically distributed

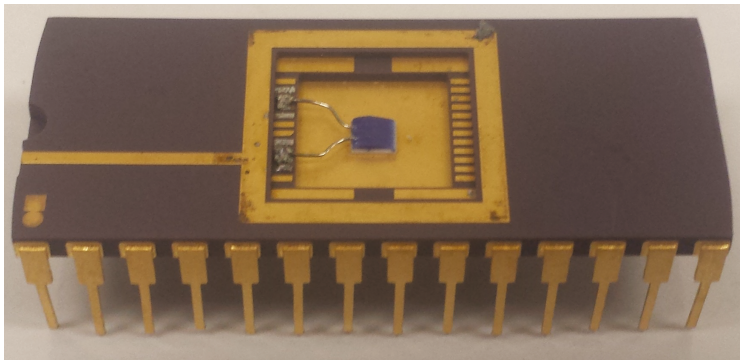

Fig. 1.9: Photograph of Pt100 sensor on ceramic substrate. Sensor leads connect to four substrate terminals, allowing four-wire resistance measurements.

errors. Here n is the number of times the response is measured, and p is the number of model coefficients, including that of the constant term.

1.6.2 Estimating Model Coefficients by Least Squares Regression

The model coefficients are determined using least squares regression, i.e. by minimizing the sum of squares of the errors,

$$L = \boldsymbol{\varepsilon}'\boldsymbol{\varepsilon} = (\boldsymbol{y} - \boldsymbol{X}\boldsymbol{\beta})'(\boldsymbol{y} - \boldsymbol{X}\boldsymbol{\beta}), \tag{1.2}$$

over all possible values for the entries of $\boldsymbol{\beta}$. Expanding Eq. (1.9),

$$\begin{aligned} L &= \boldsymbol{y}'\boldsymbol{y} - \boldsymbol{\beta}'\boldsymbol{X}'\boldsymbol{y} - \boldsymbol{y}'\boldsymbol{X}\boldsymbol{\beta} + \boldsymbol{\beta}'\boldsymbol{X}'\boldsymbol{X}\boldsymbol{\beta} \\ &= \boldsymbol{y}'\boldsymbol{y} - 2\boldsymbol{\beta}'\boldsymbol{X}'\boldsymbol{y} + \boldsymbol{\beta}'\boldsymbol{X}'\boldsymbol{X}\boldsymbol{\beta} \end{aligned} \tag{1.3}$$

L is minimized by taking partial derivatives with respect to each $\boldsymbol{\beta}$ coefficient and setting the resulting expression to zero:

$$\frac{\partial L}{\partial \boldsymbol{\beta}} = -2\boldsymbol{X}'\boldsymbol{y} + 2\boldsymbol{X}'\boldsymbol{X}\boldsymbol{\beta} = \boldsymbol{0}. \tag{1.4}$$

Solving for $\boldsymbol{\beta}$ gives the estimate

$$\hat{\boldsymbol{\beta}} = (\boldsymbol{X}'\boldsymbol{X})^{-1}\boldsymbol{X}'\boldsymbol{y}. \tag{1.5}$$

1.6.3 Estimating Error in Fitted Coefficients

To estimate the error in $\hat{\boldsymbol{\beta}}$, Eqs. (1.1) and (1.5) combine to give

$$\begin{aligned} \hat{\boldsymbol{\beta}} - \boldsymbol{\beta} &= (\boldsymbol{X}'\boldsymbol{X})^{-1}\boldsymbol{X}'(\boldsymbol{X}\boldsymbol{\beta} + \boldsymbol{\varepsilon}) - \boldsymbol{\beta} \\ &= (\boldsymbol{X}'\boldsymbol{X})^{-1}\boldsymbol{X}'\boldsymbol{\varepsilon}. \end{aligned} \tag{1.6}$$

Also from Eqs. (1.1) and (1.5), the expected value of $\hat{\boldsymbol{\beta}}$, defined as the mean value over many repeated experiments, is

$$\begin{aligned} \mathrm{E}(\hat{\boldsymbol{\beta}}) &= \mathrm{E}\left[(\boldsymbol{X}'\boldsymbol{X})^{-1}\boldsymbol{X}'(\boldsymbol{X}\boldsymbol{\beta} + \boldsymbol{\varepsilon})\right] \\ &= \boldsymbol{\beta} + (\boldsymbol{X}'\boldsymbol{X})^{-1}\boldsymbol{X}'\mathrm{E}(\boldsymbol{\varepsilon}) \\ &= \boldsymbol{\beta}, \end{aligned} \tag{1.7}$$

since the mean value of $\boldsymbol{\varepsilon}$ is assumed to be zero, i.e. $\mathrm{E}(\boldsymbol{\varepsilon}) = 0$.

The covariance matrix for $\hat{\boldsymbol{\beta}}$ is (by definition)

$$\begin{aligned}
\text{var}(\hat{\boldsymbol{\beta}}) &= \text{E}\left(\left[\hat{\boldsymbol{\beta}} - \text{E}(\hat{\boldsymbol{\beta}}) \quad \hat{\boldsymbol{\beta}}' - \text{E}(\hat{\boldsymbol{\beta}}')\ \right)\right. \\
&= \text{E}\ \ (\hat{\boldsymbol{\beta}} - \boldsymbol{\beta})(\hat{\boldsymbol{\beta}}' - \boldsymbol{\beta}')\ \ \text{, from Eq. (1.7)} \\
&= \text{E}\ \ (\boldsymbol{X}'\boldsymbol{X})^{-1}\boldsymbol{X}'\boldsymbol{\varepsilon}\boldsymbol{\varepsilon}'\boldsymbol{X}(\boldsymbol{X}'\boldsymbol{X})^{-1}\ \ \text{, from Eq. (1.6)} \\
&= (\boldsymbol{X}'\boldsymbol{X})^{-1}\boldsymbol{X}'\text{E}(\boldsymbol{\varepsilon}\boldsymbol{\varepsilon}')\boldsymbol{X}(\boldsymbol{X}'\boldsymbol{X})^{-1} \\
&= \text{E}(\boldsymbol{\varepsilon}\boldsymbol{\varepsilon}')(\boldsymbol{X}'\boldsymbol{X})^{-1} \\
&= \sigma^2(\boldsymbol{X}'\boldsymbol{X})^{-1}.
\end{aligned} \tag{1.8}$$

The standard errors for the individual model coefficients are the diagonal entries of $\text{var}(\hat{\boldsymbol{\beta}})$, with the first diagonal entry corresponding to error in the first coefficient, etc.

The next step is to calculate an estimate, $\hat{\sigma}$, for σ. Returning to Eq. (1.3), the minimum value for l is computed by substituting $\boldsymbol{\beta} = \hat{\boldsymbol{\beta}}$, giving

$$L_{\text{min}} = \boldsymbol{y}'\boldsymbol{y} - 2\hat{\boldsymbol{\beta}}\boldsymbol{X}'\boldsymbol{y} + \hat{\boldsymbol{\beta}}'\boldsymbol{X}'\boldsymbol{y} = \boldsymbol{y}'\boldsymbol{y} - \hat{\boldsymbol{\beta}}'\boldsymbol{X}'\boldsymbol{y}. \tag{1.9}$$

The quantity in Eq. (1.9) is called the sum of squared errors (SSE). Using Eq. (1.1), its expected value is

$$\begin{aligned}
\text{E(SSE)} &= \text{E}(\boldsymbol{y}'\boldsymbol{y} - \hat{\boldsymbol{\beta}}'\boldsymbol{X}'\boldsymbol{y}) \\
&= \text{E}\ \ (\boldsymbol{\beta}'\boldsymbol{X}' + \boldsymbol{\varepsilon}')(\boldsymbol{X}\boldsymbol{\beta} + \boldsymbol{\varepsilon}) - \hat{\boldsymbol{\beta}}'\boldsymbol{X}'\boldsymbol{y}\ \ \text{, from Eq. (1.1)} \\
&= \text{E}\ \ \boldsymbol{\beta}'\boldsymbol{X}'\boldsymbol{X}\boldsymbol{\beta} + \boldsymbol{\beta}'\boldsymbol{X}'\boldsymbol{\varepsilon} + \boldsymbol{\varepsilon}'\boldsymbol{X}\boldsymbol{\beta} + \boldsymbol{\varepsilon}'\boldsymbol{\varepsilon} - \hat{\boldsymbol{\beta}}'\boldsymbol{X}'\boldsymbol{y} \\
&= \boldsymbol{\beta}'\boldsymbol{X}'\boldsymbol{X}\boldsymbol{\beta} + \text{E}(\boldsymbol{\varepsilon}'\boldsymbol{\varepsilon}) - \text{E}(\hat{\boldsymbol{\beta}}\boldsymbol{X}'\boldsymbol{y}) \\
&= \boldsymbol{\beta}'\boldsymbol{X}'\boldsymbol{X}\boldsymbol{\beta} + n\sigma^2 - \text{E}[y'\boldsymbol{X}(\boldsymbol{X}'\boldsymbol{X})^{-1}\boldsymbol{X}'\boldsymbol{y}].
\end{aligned} \tag{1.10}$$

Using Eq. (1.1), the last term of Eq. (1.10) becomes

$$\begin{aligned}
\text{E}\ \ \boldsymbol{y}'\boldsymbol{X}(\boldsymbol{X}'\boldsymbol{X})^{-1}\boldsymbol{X}'\boldsymbol{y}\ \ &= \text{E}\ \ (\boldsymbol{\beta}'\boldsymbol{X}' + \boldsymbol{\varepsilon}')\boldsymbol{X}(\boldsymbol{X}'\boldsymbol{X})^{-1}\boldsymbol{X}'(\boldsymbol{X}\boldsymbol{\beta} + \boldsymbol{\varepsilon}) \\
&= \text{E}\ \ \boldsymbol{\beta}'\boldsymbol{X}'\boldsymbol{X}\boldsymbol{\beta} + \boldsymbol{\varepsilon}'\boldsymbol{X}\boldsymbol{\beta} + \boldsymbol{\beta}'\boldsymbol{X}'\boldsymbol{\varepsilon} + \boldsymbol{\varepsilon}'\boldsymbol{X}(\boldsymbol{X}'\boldsymbol{X})^{-1}\boldsymbol{X}'\boldsymbol{\varepsilon} \\
&= \boldsymbol{\beta}'\boldsymbol{X}'\boldsymbol{X}\boldsymbol{\beta} + \text{E}\ \ \boldsymbol{\varepsilon}'\boldsymbol{X}(\boldsymbol{X}'\boldsymbol{X})^{-1}\boldsymbol{X}'\boldsymbol{\varepsilon}\ \ .
\end{aligned} \tag{1.11}$$

Combining Eqs. (1.10) and (1.11),

$$\begin{aligned}
\text{E(SSE)} &= n\sigma^2 - \text{E}\ \ \boldsymbol{\varepsilon}'\boldsymbol{X}(\boldsymbol{X}'\boldsymbol{X})^{-1}\boldsymbol{X}'\boldsymbol{\varepsilon} \\
&= n\sigma^2 - \text{E}\ \ \text{tr}(\boldsymbol{\varepsilon}'\boldsymbol{X}(\boldsymbol{X}'\boldsymbol{X})^{-1}\boldsymbol{X}'\boldsymbol{\varepsilon})\ \ ,
\end{aligned} \tag{1.12}$$

where tr is the matrix trace operation. Since $\text{tr}(\boldsymbol{AB}) = \text{tr}(\boldsymbol{BA})$,

$$\begin{aligned}
\text{E(SSE)} &= n\sigma^2 - \text{E}\ \ \text{tr}(\boldsymbol{X}(\boldsymbol{X}'\boldsymbol{X})^{-1}\boldsymbol{X}'\boldsymbol{\varepsilon}\boldsymbol{\varepsilon}' \\
&= n\sigma^2 - \text{tr}\ \ \text{E}\ \ \boldsymbol{X}(\boldsymbol{X}'\boldsymbol{X})^{-1}\boldsymbol{X}'\boldsymbol{\varepsilon}\boldsymbol{\varepsilon}' \\
&= n\sigma^2 - \text{tr}\ \ \boldsymbol{X}(\boldsymbol{X}'\boldsymbol{X})^{-1}\boldsymbol{X}'\text{E}(\boldsymbol{\varepsilon}\boldsymbol{\varepsilon}') \\
&= n\sigma^2 - \sigma^2\text{tr}\ \ \boldsymbol{X}(\boldsymbol{X}'\boldsymbol{X})^{-1}\boldsymbol{X}' \\
&= n\sigma^2 - \sigma^2\ \ \boldsymbol{X}'\boldsymbol{X}(\boldsymbol{X}'\boldsymbol{X})^{-1} \\
&= n\sigma^2 - \sigma^2\text{tr}\,(\boldsymbol{I}_{p\times p}) \\
&= \sigma^2(n-p).
\end{aligned} \tag{1.13}$$

So the value of SSE calculated from the data yields an estimate for σ:

$$\hat{\sigma} = \sqrt{\frac{\text{SSE}}{n-p}}. \tag{1.14}$$

1.6.4 Computing Confidence Regions

The variance of the estimated mean response, $\hat{y}$, given a covariate vector $\boldsymbol{x}$, is

$$\begin{aligned}
\text{var}[\hat{y}(\boldsymbol{x})] &= \text{var}(\boldsymbol{x}'\hat{\boldsymbol{\beta}}) \\
&= \boldsymbol{x}'\text{var}(\hat{\boldsymbol{\beta}})\boldsymbol{x} \\
&= \sigma^2\boldsymbol{x}'(\boldsymbol{X}'\boldsymbol{X})^{-1}\boldsymbol{x}.
\end{aligned} \tag{1.15}$$

So, over many experiments, $\hat{y}(\boldsymbol{x})$ has mean $\boldsymbol{x}'\boldsymbol{\beta}$ and standard error $\sigma\sqrt{\boldsymbol{x}'(\boldsymbol{X}'\boldsymbol{X})^{-1}\boldsymbol{x}}$. Also, if the number of measurements is large, $\hat{y}$ has approximately a normal distribution. In other words, the quantity

$$\frac{y(\boldsymbol{x}) - \hat{y}(\boldsymbol{x})}{\sigma\sqrt{\boldsymbol{x}'(\boldsymbol{X}'\boldsymbol{X})^{-1}\boldsymbol{x}}} \tag{1.16}$$

has a normal distribution with a mean of 0 and standard deviation of 1. However, since σ is not known exactly and must be estimated from the data, the new quantity

$$\frac{y(\boldsymbol{x}) - \hat{y}(\boldsymbol{x})}{\hat{\sigma}\sqrt{\boldsymbol{x}'(\boldsymbol{X}'\boldsymbol{X})^{-1}\boldsymbol{x}}} \tag{1.17}$$

has a student's t distribution with $(n-p)$ degrees of freedom. So 95 % confidence bounds for $y(\boldsymbol{x})$ are

$$\hat{y}(\boldsymbol{x}) \pm t_{0.025,n-p}\hat{\sigma}\sqrt{\boldsymbol{x}'(\boldsymbol{X}'\boldsymbol{X})^{-1}\boldsymbol{x}}. \tag{1.18}$$

The bounds in Eq. (1.18) can be translated into a 95 % confidence region for $\boldsymbol{x}$ by choosing a target value y_t, and finding the set of all $\boldsymbol{x}$ for which the range $\hat{y}(\boldsymbol{x}) \pm 1.96\hat{\sigma} \quad \overline{\boldsymbol{x}'(\boldsymbol{X}'\boldsymbol{X})^{-1}\boldsymbol{x}}$ includes y_t.

An approximate joint confidence region from two models, assuming that their responses are independent, is generated using the quantity

$$\left(\frac{y_1(\boldsymbol{x}) - \hat{y}_1(\boldsymbol{x})}{\hat{\sigma}_1 \quad \overline{\boldsymbol{x}'(\boldsymbol{X}'\boldsymbol{X})^{-1}\boldsymbol{x}}}\right)^2 + \left(\frac{y_2(\boldsymbol{x}) - \hat{y}_2(\boldsymbol{x})}{\hat{\sigma}_2 \quad \overline{\boldsymbol{x}'(\boldsymbol{X}'\boldsymbol{X})^{-1}\boldsymbol{x}}}\right)^2, \tag{1.19}$$

where y_1 and σ_1 represent the mean response and error term standard deviation for model 1, respectively, and similarly for y_2 and σ_2. For large enough samples sizes, the quantity in Eq. (1.17) can be assumed to have a standard normal distribution. Then, as the sum of squares of two quantities with standard normal distributions, Eq. (1.19) has a χ^2 distribution with 2 degrees of freedom. So a joint 95 % confidence region for $\boldsymbol{x}$ is the set of values for $\boldsymbol{x}$ that result in

$$\left(\frac{y_1(\boldsymbol{x}) - \hat{y}_1(\boldsymbol{x})}{\hat{\sigma}_1 \quad \overline{\boldsymbol{x}'(\boldsymbol{X}'\boldsymbol{X})^{-1}\boldsymbol{x}}}\right)^2 + \left(\frac{y_2(\boldsymbol{x}) - \hat{y}_2(\boldsymbol{x})}{\hat{\sigma}_2 \quad \overline{\boldsymbol{x}'(\boldsymbol{X}'\boldsymbol{X})^{-1}\boldsymbol{x}}}\right)^2 \leq 5.99, \tag{1.20}$$

where the value 5.99 is obtained from the inverse of the cumulative distribution function for the χ^2 distribution. Eq. (1.20) is the formula used to estimate confidence intervals for optimized factors for ball bonding processes in Section 3.3.

1.6.5 Predicting Individual Measurements

Eq. (1.20) predicts a likely range for the mean response. To predict the likely range for a single measurement, the error term ε must also be included. Assuming that the error in a single measurement is independent of previous errors, the variance of a single measurement *i* is

$$\begin{aligned} \text{var}(y_i) &= \text{var}(\hat{y} + \varepsilon_i) \\ &= \text{var}(\hat{y}) + \text{var}(\varepsilon_i) \\ &= \sigma^2 \boldsymbol{x}'(\boldsymbol{X}'\boldsymbol{X})^{-1}\boldsymbol{x} + \sigma^2. \end{aligned} \tag{1.21}$$

So the standard error when predicting a single measurement is

$$\overline{\hat{\sigma}^2(1 + \boldsymbol{x}'(\boldsymbol{X}'\boldsymbol{X})^{-1}\boldsymbol{x})}, \tag{1.22}$$

which can be used to generate confidence intervals or regions in the same way as Eq. (1.18) or Eq. (1.20).

1.7 Statistical Methods for Reliability Analysis

1.7.1 Censoring of Lifetime Data

After carrying out reliability tests, statistical analysis is needed to ensure that any trends observed are statistically significant, i.e., unlikely to have occurred by pure chance. Reliability studies present particular challenges for statistical analysis. For example, reliability testing is often stopped before all samples being tested have failed, so the times that failures would have occurred are unknown. The failure times are said to be right-censored in this case. Other types of censoring, namely left-censoring and interval censoring, also occur in other scenarios, for instance when studying human patient survival data, but do not occur in this thesis. The branch of statistics dealing with censored data is called survival analysis.

In a standard scenario in survival analysis there are n samples tested in total. Sample i is observed until time t_i, at which point observation stops due to failure or censoring. A censoring indicator is defined as $\delta_i = 1$ if sample i failed at t_i, and $\delta_i = 0$ if observation of sample i was censored.

1.7.2 Accelerated Failure Time Models

Accelerated failure time (AFT) models are an important class of statistical models used in survival analysis. The procedure for fitting such models is summarized graphically in Fig. 1.10. Given a set of covariates x_1 to x_p, these models assume that the random failure time T has the form

$$\log(T) = u(x_1, x_2, ..., x_p) + bZ, \tag{1.23}$$

where u is a function of the covariates, b is called the scale parameter, and $Z = \frac{\log(T)-u}{b}$ is a random variable accounting for the random distribution of failure times. Covariates are measurable variables that may affect the lifetime of a sample, such as ambient temperature or relative

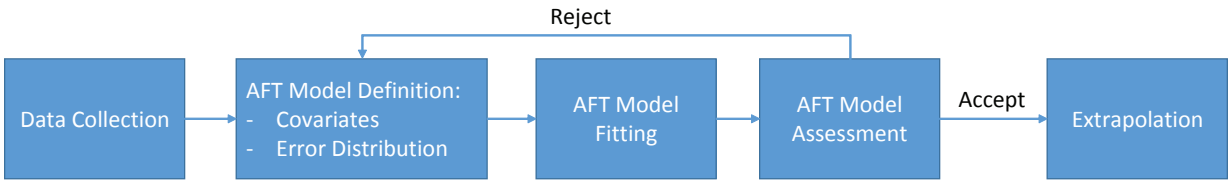

Fig. 1.10: Graphical summary of definition, fitting, and evaluating procedure for accelerated failure time model.

humidity. Specifying a particular AFT model means choosing which covariates to include, choosing the form of the function u and assuming a probability distribution for Z. This work makes the typical assumptions that u is linear and the covariates are constant in time, so that

$$\log(T) = g_0 + g_1 x_1 + ... + g_p x_p + bZ, \tag{1.24}$$

where g_0 to g_p are constants to be determined by fitting to the data. For sample i in a set of n samples, this equation is commonly abbreviated as

$$\log(T_i) = \boldsymbol{g} \cdot \boldsymbol{x}_i + bZ_i, \tag{1.25}$$

where $\boldsymbol{g} = (g_0, g_1, ..., g_p)$ and $\boldsymbol{x} = (1, x_{i1}, x_{i2}, ..., x_{ip})$ are vectors with length $p+1$.

To determine $\boldsymbol{g}$, a distribution must be chosen for Z. Typically, the model is fit to the data using several candidate distributions, and the model allowing the best fit is selected. Common choices for Z include a standard normal distribution, resulting in a log-normal distribution for T, or an extreme value distribution, resulting in a Weibull model for T. The corresponding probability density functions for Z are

$$\begin{aligned} f(z) &= \frac{1}{2\pi}\exp(-z^2) \quad \text{(Normal)} \\ f(z) &= \exp[z - \exp(z)] \quad \text{(Extreme Value)}, \end{aligned} \tag{1.26}$$

and the survival functions are

$$\begin{aligned} S(z) &= P(Z \geq z) = 1 - \Phi(z) \quad \text{(Normal)} \\ S(z) &= P(Z \geq z) = \exp(-\exp(z)) \quad \text{(Extreme Value)}, \end{aligned} \tag{1.27}$$

where $\Phi(z) = \frac{1}{\sqrt{2\pi}} \int_{-\infty}^{z} \exp\left(-\frac{u^2}{2}\right) du$ is the cumulative distribution function for the standard normal distribution.

1.7.3 Arrhenius Activation Energy

AFT models can be used to estimate activation energies for use in the Arrhenius equation. The Arrhenius equation predicts a temperature-dependent lifetime of

$$t = A \cdot \exp\left(\frac{E_a}{k_B T_K}\right), \tag{1.28}$$

where A is a constant, E_a is the activation energy, k_B is Boltzmann's constant, and T_K is the temperature in Kelvin. Taking the logarithm gives

$$\log(t) = \log(A) + \frac{E_a}{k_B T_K}. \tag{1.29}$$

Omitting the random error z, this equation has the same form as Eq. (1.24) with $g_0 = \log(A)$, $g_1 = E_a$, and a single covariate, $x_1 = \frac{1}{k_B T_K}$. So, referring to Eq. (1.24), the AFT form for the Arrhenius model is

$$\log(T) = g_0 + g_1 x_1 + bZ. \tag{1.30}$$

After fitting this model to a set of lifetime data, the fitted value of g_1 can be used as an estimate of the activation energy.

1.7.4 Model Fitting by Maximum Likelihood Estimation

Fitting the model in Eq. (1.24) to data means identifying the values of b and $\boldsymbol{g}$ that are most consistent with the data. This is generally done using the maximum likelihood estimation (MLE) method. In this method, a likelihood function is defined in terms of the observed data, the probability distribution of Z, and $\boldsymbol{g}$. The likelihood function is proportional to the probability of obtaining the measured data, given the model assumptions and coefficients.

For a general AFT model with right-censored data, as in Eq. (1.23), given the data t_i, δ_i and covariates x_{ij}, for i from 1 to n and j from 1 to p, the likelihood function (actually a partial likelihood, see [75] for details) is defined as

$$L(\boldsymbol{u}, b) = \prod_{i=1}^{n} \left[\frac{1}{b} f \quad \frac{\log(t_i) - u_i}{b} \right)\Bigg]^{\delta_i} S \quad \frac{\log(t_i) - u_i}{b} \quad {}^{1-\delta_i}, \tag{1.31}$$

where $u_i = u(x_{i1}, x_{i2}, ..., x_{ip})$, $f(z)$ is the probability density function for Z as above, and $S(z)$ is the survival function for Z.

The MLE procedure chooses $\boldsymbol{u}$ and b to maximize the likelihood function. Doing so is equivalent to maximizing the log of the likelihood function,

$$\log\left(L(\boldsymbol{u}, b)\right) = \ell(\boldsymbol{u}, b) = -r\log(b) + \sum_{i=1}^{n} [\delta_i \log(f(z_i)) + (1 - \delta_i)\log(S(z_i))], \tag{1.32}$$

where r is the number of failures observed and $z_i = \frac{\log(t_i) - u_i}{b}$. This function is maximized by setting its derivatives to zero:

$$\frac{\partial \ell(\boldsymbol{u}, b)}{\partial b} = 0, \tag{1.33a}$$

$$\frac{\partial \ell(\boldsymbol{u}, b)}{\partial g_i} = 0, \text{for } i = 1 \text{ to } p. \tag{1.33b}$$

These equations generally must be solved computationally. In MATLAB, the Accelerated Failure Time package for MATLAB [76] is a convenient implementation. The values $\hat{b}$ and $\hat{\boldsymbol{g}}_i$ that solve Eqs. (1.33a) and (1.33b) are the maximum likelihood estimates for the model Eq. (1.24).

1.7.5 Graphical Assessment of Fit

After fitting a model as in Section 1.7.4 the quality of fit is assessed graphically as follows. For each failure time t_i, by rearranging Eq. (1.30), a residual z_i is defined as

$$z_i = \frac{\log(t_i) - g_0 - g_1 x_i}{b}. \tag{1.34}$$

If the chosen model is appropriate, these residuals should be distributed according to the corresponding distribution in Eq. (1.27). For the log-normal model, Eq. (1.27) rearranges to become

$$z = \Phi^{-1}\left(1 - S(z)\right). \tag{1.35}$$

So, given an estimate $\hat{S}(z)$, a plot of $\Phi^{-1}\left(1 - S(z_i)\right)$ versus z_i gives a visual indication of the fit quality. A perfect fit would appear as a straight line with a slope of 1 and passing through the origin; any deviation indicates disagreement between the model and the observations. Similarly, for the Weibull model, Eq. (1.27) can be rewritten as

$$z = \log(-\log(S(z))), \tag{1.36}$$

so a plot of $\log(-\log(S(z)))$ versus z_i indicates the quality of the fit.

To account for censored data and avoid biasing the results, a Kaplan-Meier estimate for $\hat{S}(z)$ is used, which does not depend on the assumed error distribution. The Kaplan-Meier estimate for a given z is defined as [75]

$$\hat{S}(z) = \prod_{i:z_i<z} \frac{n_i - f_i}{n_i}. \tag{1.37}$$

Here n_i is the number of samples that were being observed at the time corresponding to $z = z_i$: those that had not yet failed or been censored, and f_i is the number of samples that failed with

$z = z_i$. Fig. 1.11 (a) shows a typical plot of $\Phi^{-1}\left[1-\hat{S}(z_i)\right]$ versus z_i, indicating that the log-normal model provides a good fit to the observed lifetimes. In contrast, the plot of $\log(-\log(\hat{S}(z)))$ for the Weibull model in Fig. 1.11 exhibits significant curvature, meaning that the Weibull model is not well-suited to this data.

1.7.6 Confidence Intervals

After fitting a model as in Section 1.7.4, it is important to assess the degree of confidence in model estimates, such as the activation energy or median lifetime. The MLE framework enables estimation of confidence intervals, which express a range of likely values for the true parameter of interest. After obtaining the estimates $\hat{b}$ and $\hat{\boldsymbol{g}}$, the observed information matrix is calculated from 1.32 as

$$I(\hat{b},\hat{\boldsymbol{g}}) = \begin{bmatrix} -\partial^2\ell/\partial\boldsymbol{g}'\partial\boldsymbol{g} & -\partial^2\ell/\partial\boldsymbol{g}'\partial b \\ -\partial^2\ell/\partial b\partial\boldsymbol{g} & -\partial^2\ell/\partial b^2 \end{bmatrix}. \tag{1.38}$$

The errors in the estimates $\hat{b}$ and $\hat{\boldsymbol{g}}$ are approximately normally distributed, with a covariance matrix $I(\hat{b},\hat{\boldsymbol{g}})^{-1}$. So, for example, $\text{se}(\hat{g}_0)$, the standard error for $\hat{g}_0$,i s the (1,1) entry of the matrix $I(\hat{b},\hat{\boldsymbol{g}})^{-1}$, and a 95 % confidence interval can be calculated as $\hat{g}_0 \pm 1.96 \cdot \text{se}(\hat{g}_0)$. More generally, a $(1-\alpha)$ % confidence interval is given by $\hat{g}_0 \pm z_{1-\alpha/2} \cdot \text{se}(\hat{g}_0)$, where $z_{1-\alpha/2} = \Phi^{-1}(1-\alpha/2)$.

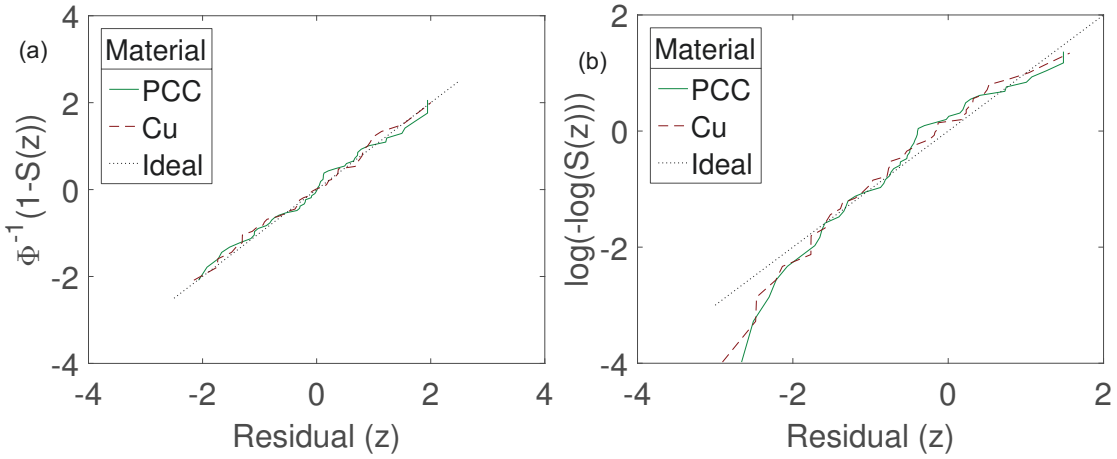

Fig. 1.11: Example of fit assessment plots for two models fitted to lifetime data for Cu wire bonds on 800 nm thick Al bond pads, aged at temperatures of 175 °C, 200 °C, and 225 °C. (a) Log-normal model fits the data well. (b) Weibull model fits poorly, showing curvature.

1.7.7 Extrapolation to Lower Temperature

From the fitted models, the survival probability can be estimated for any combination of time and temperature. With the log-normal failure distribution, the probability of a sample failing at a time less than or equal to t is

$$F(t) = \Phi \quad \frac{\log(t) - g_0 - \frac{g_1}{k_B T}}{b} \quad , \tag{1.39}$$

where Φ is the cumulative distribution function for the standard normal distribution [75]. To estimate t_p, the time until a fraction p of the samples fail, Eq. (1.39) can be rearranged to give

$$\hat{t}_p = \exp \quad \hat{b}\Phi^{-1}(p) + \hat{g}_0 + \frac{\hat{g}_1}{k_B T} \quad , \tag{1.40}$$

where $\hat{t}_p$, $\hat{b}$, $\hat{g}_0$, and $\hat{g_1}$ refer to quantities estimated from the measured data. Confidence intervals for t_p can be obtained as follows, using the variance-covariance matrix for $\hat{g}_0$, and $\hat{g}_1$, and $\hat{b}$, which is calculated as part of the fitting procedure. First, Eq. (1.40) can be written as

$$\log(\hat{t}_p) = \hat{g}_0 + \frac{\hat{g}_1}{k_B T} + \hat{b}\Phi^{-1}(p). \tag{1.41}$$

This is a linear combination of the parameters $\hat{g}_0$, $\hat{g}_1$, and $\hat{b}$, alternatively written in matrix form as

$$\log(\hat{t}_p) = c \quad \hat{g}_0, \hat{g}_1, \hat{b} \quad ', \tag{1.42}$$

where

$$c = \quad 1, \frac{1}{k_B T}, \Phi^{-1}(p) \quad . \tag{1.43}$$

So, by a standard property of variances, the variance of $\log(\hat{t}_p)$ is

$$\mathrm{var}(\log(\hat{t}_p)) = c\Sigma c', \tag{1.44}$$

where Σ is the variance-covariance matrix for $\hat{g}_0$, and $\hat{g}_1$, and $\hat{b}$. Therefore, the standard error of the estimate $\log(\hat{t}_p)$ is

$$\mathrm{se}(\log(\hat{t}_p)) = \sqrt{c\Sigma c'}. \tag{1.45}$$

Making a typical assumption that the parameter estimates are approximately normally-distributed, approximate 95 % confidence bounds for $\log(\hat{t}_p)$ are

$$c(\hat{g}_0, \hat{g}_1, \hat{b})' \pm 1.96\sqrt{c\Sigma c'}. \tag{1.46}$$

Corresponding confidence bounds for $\hat{t}_p$ are then

$$\exp \quad c(\hat{g}_0, \hat{g}_1, \hat{b})' \pm 1.96\sqrt{c\Sigma c'} \quad . \tag{1.47}$$

1.8 Recommendations for Experiment Planning

Detailed recommendations for test conditions and sample size required for a given requirement of precision are found in [77], based on numerical tables. Methods for estimating the experimental precision from simulations are discussed in [78]. Generally, pilot studies or data from similar devices are required for preliminary estimates of b and the mean lifetimes at the operating temperature and at maximum testing temperature. The maximum test temperature should be chosen as the highest value that does not change the mode of failure, since a wide range of temperatures improves the precision of the coefficient estimates.

A general recommendation made in [77] is to use three test temperatures, with larger sample sizes for the lower temperatures, in the ratio 4:2:1 for the low, medium and high temperatures, respectively. Although recommended against in [77] due to poorer statistical precision, this thesis used a traditional experimental plan, with equal numbers of samples at each temperature, to allow an adequate number of samples at each temperature for physical analysis at intermediate times.

Chapter 2

Experimental Setup

This chapter consists of two sections, with 12 subsections. Section 2.1 is adapted from [2] and describes a novel system developed for temperature and humidity control. The system is introduced in Subsection 2.1.1. Subsection 2.1.2 describes the basic operating principle of the chamber. Subsection 2.1.3 presents the solution to challenges of heat transfer and sealing. Subsection 2.1.4 describes the sensors used to monitor humidity in the chamber. Subsection 2.1.5 describes a problem of condensation forming on the samples, and how it was resolved. Subsections 2.1.6 and 2.1.7 characterize the behaviour and performance of the chambers. Subsection 2.1.8 demonstrates an application of the system to reliability testing, and subsection 2.1.9 concludes the section.

Section 2.2 describes investigation and improvement of the temperature accuracy of the miniature ovens used for reliability testing. Subsection 2.2.1 finds that there are temperature inconsistencies in the oven systems and demonstrates that they are not explained by asymmetries in the ovens. Subsection 2.2.2 uses the known melting point of Sn-Pb to quantify temperature inaccuracy and demonstrates that sensor calibration also does not account for the full inaccuracy. Subsection 2.2.3 describes a solution to these problems using graphite pads to improve heat transfer.

2.1 Modification of Mini-Oven to Achieve Humidity Control

2.1.1 Introduction

This section presents humidity control modifications developed for the small, low-cost ovens of Section 1.5.1. These ovens allow parallel environmental testing by using multiple identical chambers, each of which can be controlled separately. The oven system was developed by previous students and private companies. The humidity control modifications made to the ovens are reversible. Stable operation is demonstrated from 30 °C to 85 °C, at humidities from 44 % to 90 %. It provides full electrical connectivity between the device under test (DUT) and external instruments, allowing electrical bias, device operation, and a variety of non-destructive monitoring techniques during testing [26, 49, 79]. Electrical connections are located outside the chamber at ambient humidity and moderate temperatures, eliminating the likelihood of connection failures.

2.1.2 Generating Target Humidity with Aqueous Glycerol Solutions

A desired humidity value is generated inside the chamber by using aqueous glycerol solutions placed inside the chamber, based on the method of ASTM Standard D5032 [80]. Glycerol, also known as glycerine, is an organic compound consisting of a chain of three carbon atoms with a hydroxyl (OH) group bonded to each, with hydrogen atoms filling the remaining available bonds [81], as shown in Fig. 2.1. It is commonly added to foods and to skin care products, since it attracts and retains moisture, and also adds a sweet flavour to foods. It is mainly produced by reacting triglycerides, found in plant or animal fats, with sodium hydroxide. This reaction is known as saponification and also produces sodium stearate, a common soap.

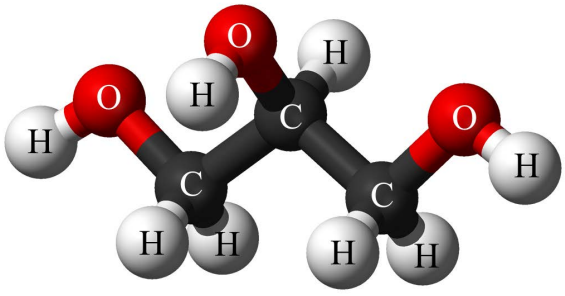

Fig. 2.1: Chemical structure of glycerol. Modified from [81] (public domain).

Glycerol is miscible with water, but has a much lower saturation vapor pressure than water at a given temperature: about 0.01 Pa (10^{-7} atm) at 20 °C, and 20 Pa ($2 \cdot 10^{-4}$ atm) at 100 °C. Corresponding vapor pressures for water are about 2300 Pa (0.023 atm) and 10^5 Pa (1.0 atm), respectively [82, 83]. Its boiling point, 290 °C, is correspondingly higher than water's. Aluminum cups, described further in Section 2.1.5, were used to hold the liquid solutions and fit inside the chamber heaters, as shown in Fig. 2.2.

The humidity generated by a glycerol-water mixture is approximately described by Raoult's law, which gives the partial pressure of component i generated by a binary solution as [84]

$$p_i = p_i^* x_i, \tag{2.1}$$

where p_i^* is the vapor pressure of component i in a pure form and x_i is the mole fraction of component i in the solution. Since the relative humidity (RH) is defined as the partial pressure of water vapor, p_{water}, divided by the saturation vapor pressure, p_{water}^*, Eq. 2.1 can be written as

$$\text{RH} = x_{\text{water}}. \tag{2.2}$$

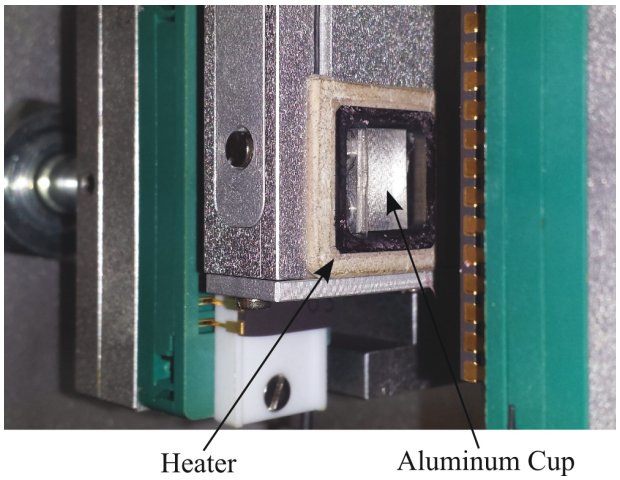

Fig. 2.2: Photograph of 11 mm × 11 mm × 7 mm aluminum cup placed inside humidity chamber. See Fig. 2.7 for details of cup. Own work, reproduced from [2].

In this work, the solutions are concentrations are measured in terms of the concentration of glycerol by weight, w_G, so Eq. 2.2 must be converted accordingly:

$$\begin{aligned} \mathrm{RH} &= \frac{n_W}{n_W + n_G} \\ &= \frac{m_W/M_W}{m_W/M_W + m_G/M_G} \\ &= \frac{w_W/M_W}{w_W/M_W + w_G/M_G} \\ &= \frac{(1-w_G)/M_W}{(1-w_G)/M_W + w_G/M_G} \end{aligned} \tag{2.3}$$

where n_W, m_W, M_W, and w_W are the number of moles, mass, molar mass, and weight fraction, respectively, for water, and similarly for glycerol. M_G and M_W are the molar masses of 92.1 g/mol and 18.0 g/mol for glycerol and water, respectively. The humidity as a function of glycerol concentration predicted by this formula is shown in Fig. 2.3.

In reality, the humidity depends on temperature as well as concentration; Eq. 2.3 fails to predict this temperature dependence because it is based on an oversimplification of the interactions

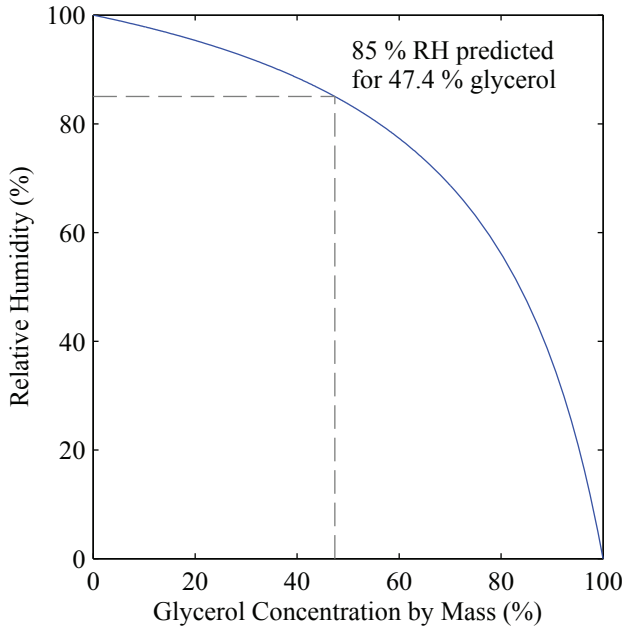

Fig. 2.3: Humidity as a function of glycerol concentration according to Raoult's law. Own work, reproduced from [2].

between atoms in the liquid. Therefore Raoult's law serves as an approximate guideline for this work. The measured dependence of humidity on concentration and temperature is reported in [80]. However, because of temperature gradients, the humidity measured in the chamber may differ from the value expected from [80] so the humidity behaviour of this chamber is characterized independently, with the results presented in Section 2.1.6.

2.1.3 Moisture Seal that Transfers Heat Effectively

Sealing gaskets are required between the heater and the test substrates to prevent moisture escaping and a gradual decrease of humidity. It is also important to minimize temperature differences between interior surfaces of the chamber to ensure uniform humidity and prevent condensation on cold surfaces. Therefore, in addition to their role of sealing the chamber, the gaskets must have high thermal conductivity to avoid cold surfaces, as they provide the primary path for heat flow between the heater and the ceramic substrates.

The product Tflex SF600 from Laird PLC (London, UK), sold as a thermal interface material for heat transfer between an IC package and a metal heat sink, was found to be suitable. It is supplied in 23 cm $\times$ 23 cm sheets in a variety of thicknesses. It has a high thermal conductivity of 3 W/(m K) and allowed long operating times before excessive moisture loss, as demonstrated in Section 2.1.7. All characterization results were obtained using 0.5 mm thick gaskets cut from this material. A punch and die set were produced for fast and reproducible production of these gaskets from large sheets. An example gasket, cut using the punch and die, is shown in Fig. 2.4. Set screws, one on each side of the oven, allow adjustment of the gasket compression provided by the toggle clamps. This seal cannot maintain a large pressure difference between the interior and exterior, limiting conditions to those with water vapor pressures below the ambient air pressure, so that the interior pressure does not exceed the exterior pressure.

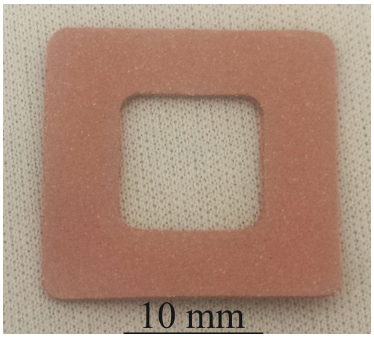

Fig. 2.4: Gasket punched from larger sheet of Laird TFlex SF600 using custom punch and die.

2.1.4 Custom-Packaged Temperature and Humidity Sensor

The humidity inside the chamber was monitored using commercial sensors, model HIH9130-021 produced by Honeywell International Inc., Morris Plains, NJ, USA. Each device combines humidity and temperature sensing, signal conditioning, and digital communication functions into a single package. They have a rated operating range of -40 °C to 125 °C and 0 % to 100 % relative humidity, although the accuracy is only specified for temperatures up to 50 °C. Most importantly, they have a small physical size, 6 mm × 4.9 mm × 2.1 mm, allowing one sensor to fit on one of the substrates, together with a Pt100 sensor, inside each chamber. Electrical connections to the sensors were made by soldering fine Sn-coated Cu wires between the sensor leads and the ceramic substrates, as shown in Fig. 2.5.

Early tests indicated large upward drifts in humidity readings at temperatures significantly above 85 °C. These sensors were replaced, and subsequent experiments were limited to near or below 85 °C and 85 % RH, in order to avoid degradation of the replacement sensors. To calibrate the sensors, 8 sensors were placed in a standard commercial humidity chamber (model Espec BTL-433, in Prof. Pearl Sullivan's lab at UW) at nominal conditions of 85 °C and 85 % RH. After waiting 12 h for equilibration, the chamber's sensor reported 84.6 % RH and the Honeywell sensors reported an average of 88.3 % RH, with a standard deviation of 1.2 % RH. The offset for each sensor was subtracted its nominal reading when characterizing the humidity response in Subsection 2.1.6.

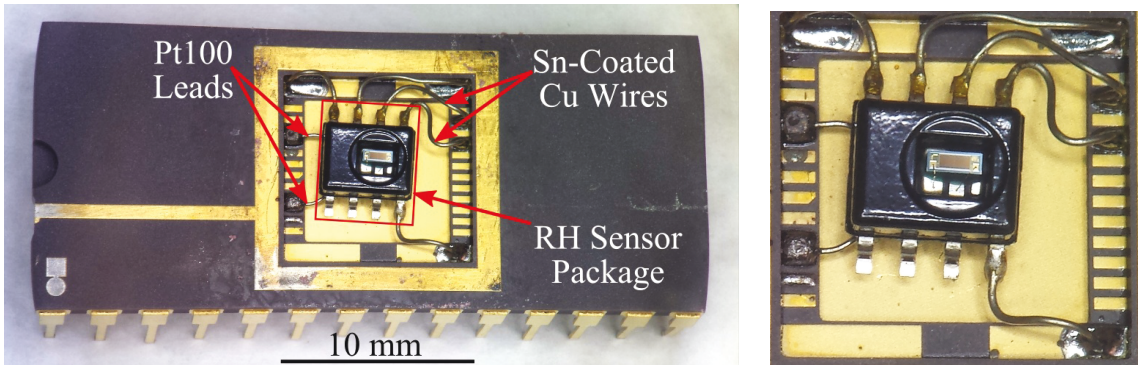

Fig. 2.5: Humidity sensor with Sn-coated Cu wires connecting sensor leads to leadfingers of ceramic substrate. Underneath the humidity sensor is a Pt100 temperature sensor, used in the temperature control feedback loop of the mini-oven rack. Own work, reproduced from [2].

2.1.5 Prevention of Condensation Using Silicone Membranes

On multiple occasions, condensation was observed on test samples, as shown in Fig. 2.6, after several days of chamber operation. Such condensation risks invalidating experimental results, since failure mechanisms may be different when liquid water is present in addition to water vapor and the accompanying microscopic surface film. Further investigation indicated that the condensation did not boil when heated above 100 °C, but dissolved quickly in water, leading to the conclusion that glycerol was a main constituent of the droplets. Therefore a selective barrier is needed to prevent glycerol transport to the sample, while letting water vapor pass through.

The selective barrier was achieved by placing a 0.25 mm thick cover of high-purity silicone over the glycerol-water solution, as shown in Figs. 2.7 (a) and (b), since silicone is known to be permeable to water vapor [85]. An aluminum plate with a central hole was used to clamp the membrane against the cup, ensuring no vapor could escape the cup without passing through the membrane. The central hole in the top plate allowed for an open path through the membrane. All humidity test data presented in this thesis used this system, with no further condensation observed during characterization.

No data was available regarding the permeability of glycerol vapor through silicone. However, Robb [86] reports permeabilities for water vapor and many other chemicals through silicone, which may be used for comparison. Compared to that of water vapor, the organic compounds listed have permeabilities ranging from 27 % less for ethylene to 97 % less for methane, so the value for glycerol is likely within this range, making it smaller than the value for water vapor. The precise permeability value is not necessary for this work: if no condensation is observed after multiple long-duration tests, then the silicone membrane is adequate for this purpose.

The presence of the silicone membrane is assumed to have only a small effect, if any, on the relative humidity produced in the chamber, based on the following thermodynamical argument involving the chemical potential, μ, which describes the potential energy of a specific type of particle in a given system. When particles can be exchanged between two systems, the particles spontaneously move to the system where their chemical potential is lower [87] until the systems reach equilibrium with equal chemical potentials.

The chemical potential of one component in a mixture of ideal gases is described by the formula [88]

$$\mu = \mu_0(T, P_0) + k_B T \ln(P_i/P_0), \tag{2.4}$$

where $\mu_0(T, P_0)$ is the chemical potential of the pure component at temperature T and reference pressure P_0, P_i is the partial pressure of the component of interest, and k_B is Boltzmann's constant.

Viewed in these terms, the effect of mixing glycerol with water is to lower the chemical potential of the water molecules in the solution. Since the liquid and vapor phases are in equilibrium,

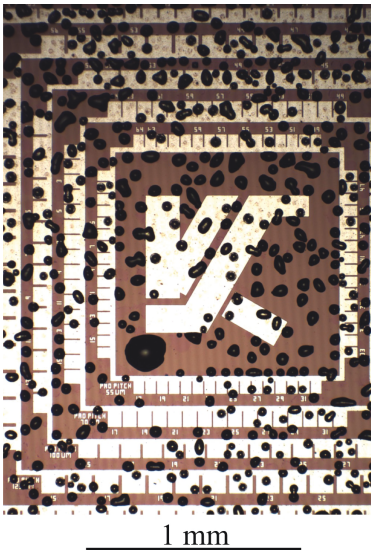

Fig. 2.6: Glycerol condensation on test chip after 59 h of operation at 85 °C with a 52.9 % glycerol solution and no silicone membrane. Own work, reproduced from [2].

their chemical potentials are equal, and the reduction of the chemical potential is demonstrated by the reduction of the relative humidity, corresponding to a reduction in the vapor pressure term in Eq. 2.4.

Water molecules are able to pass through the silicone membrane, meaning that after sufficient time, the chemical potentials on both sides of the membrane are equal, i.e. $\mu_{\text{outside}} = \mu_{\text{inside}}$. So, from Eq. 2.4,

$$\mu_0(T,P_0) + k_B T \ln(P_{\text{water, outside}}/P_0) = \mu_0(T,P_0) + k_B T \ln(P_{\text{water, inside}}/P_0). \tag{2.5}$$

The term $\mu_0(T,P_0)$ and the factor $k_B T$ are the same on both sides of the equation and can be eliminated, leaving

$$\ln(P_{\text{water, outside}}/P_0) = \ln(P_{\text{water, inside}}/P_0), \tag{2.6}$$

which is only possible if $P_{\text{water, outside}} = P_{\text{water, inside}}$, and therefore the relative humidity is the same on both sides of the membrane. Assuming no transport of glycerol through the membrane, the total pressures in the two volumes differ slightly, since glycerol vapor is present inside the cup but not outside, and the partial pressures of other gases are the same on both sides. At 85 °C, this pressure difference is at most 8 Pa (0.00008 atm), the vapor pressure of glycerol at that temperature [82]. The above argument assumed ideal gas behaviour; in reality, interactions between water and glycerol molecules in the vapor phase may alter the equilibrium, but this effect can be assumed negligible, given the low vapor pressure of glycerol.

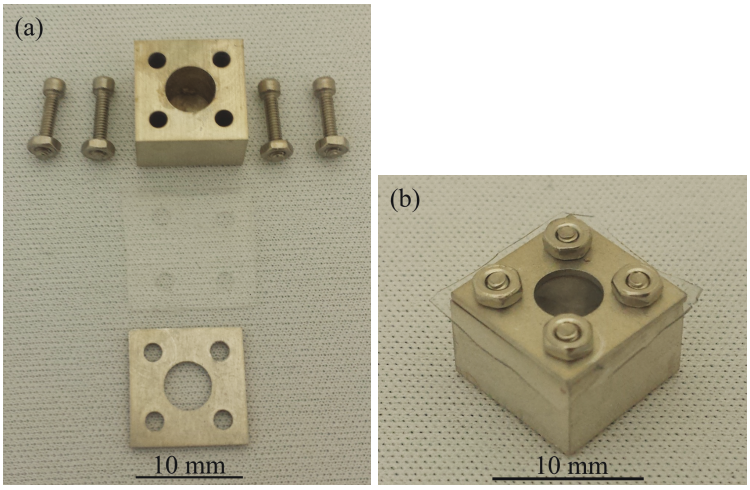

Fig. 2.7: Aluminum cup with silicone membrane and aluminum top plate. Cup is filled with glycerol-water mixture, assembled, and placed inside the heater as shown in Fig. 1.7. (a) Disassembled. (b) Assembled. Own work, reproduced from [2].

2.1.6 Dependence of Humidity on Glycerol Concentration and Temperature

A series of tests was performed to determine the humidity produced by a given glycerol concentration and temperature. Each test consisted of an upward temperature ramp from 25 °C to 85 °C in 5 °C, 5 h steps, with the humidity recorded continuously. A typical result is shown in Fig. 2.8 (a). At each temperature step, RH decreases sharply because additional moisture must diffuse through the silicone membrane to reestablish equilibrium as the saturation vapor pressure of water rises.

For each temperature step, the equilibrium recorded humidity was determined by an exponential fitting between 0.2 h and 4.8 h after the start of the temperature increase. Steps where equilibrium was not reached, with a difference of more than 0.1 % RH between the fitted value and the mean of the last 100 measurements, were excluded from the analysis. Steps where the exponential function fitted the data poorly, classified by having a coefficient of determination $r^2 < 0.85$, were also excluded. The results are shown in Fig. 2.8 (b). Interpolation of the data indicates that the standard condition of 85 °C and 85 % RH can be achieved using a solution of 53 % glycerol. Mean time constants for reaching humidity equilibrium, determined by the same exponential fitting procedure, ranged from 0.5 h at 85 °C to 1.2 h at 30 °C. Typical time constants without silicone membranes were about 0.03 h, indicating that the time for diffusion through the

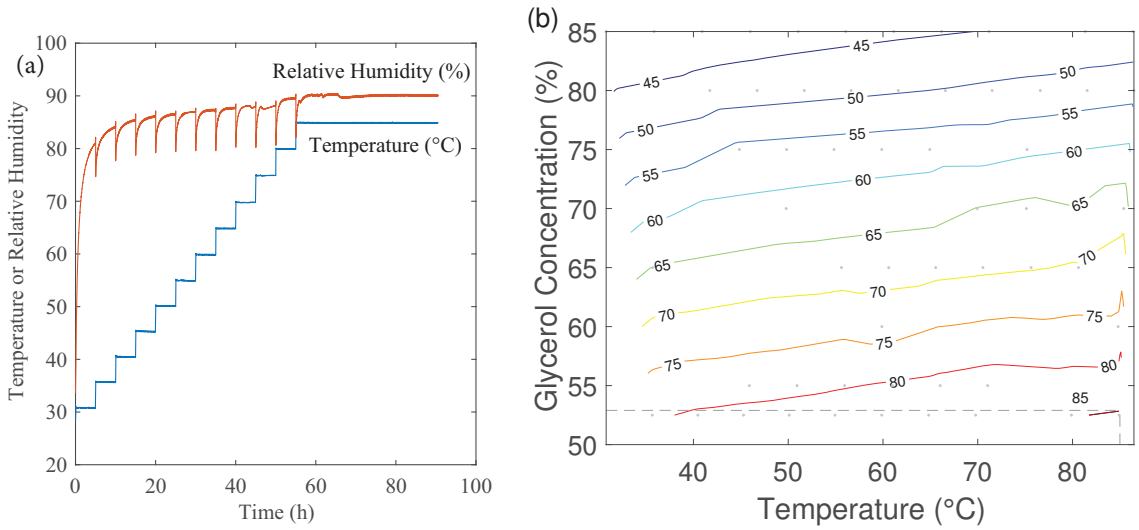

Fig. 2.8: (a) Typical behaviour of chamber. Temperature and nominal humidity over time resulting from a 52.5 % glycerol solution. Own work, reproduced from [2]. (b) Contour plot showing dependence of humidity on temperature and glycerol concentration. Dots indicate temperature and concentration combinations for which data was included. Contour lines were obtained in MATLAB using natural neighbour interpolation. Dashed lines indicate that 85 °C and 85 % RH are achieved with a 53 % glycerol solution. Own work, reproduced from [2].

membranes was the primary contribution to the equilibrium time. Therefore the time constants could be reduced by using thinner membranes or by increasing the exposed membrane area.

2.1.7 Stability of Humidity over Time

The stability of the chamber of long durations was tested by monitoring humidity while keeping temperature constant at 85 °C. The glycerol concentration was 55 %, chosen to achieve humidity near 85 %. As shown in Fig. 2.9 (a), the humidity was between 84 % and 85 % in the first 150 h, then gradually decreased, remaining within the range of 85 ± 5 % for 653 h. This time may be extended by using a modified glycerol cup design, providing a larger internal liquid reservoir. Alternatively, the partially depleted cup may be removed and replaced with a new one, restoring the chamber to a higher humidity, as shown in Fig. 2.9 (b).

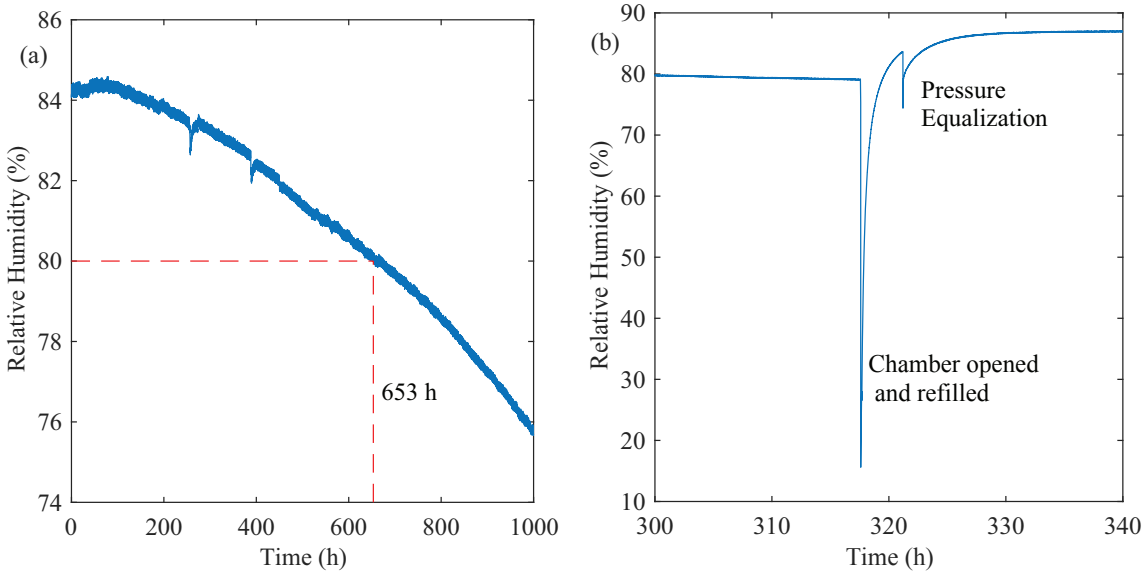

Fig. 2.9: Demonstrations of chamber performance over long time intervals. (a) Test of humidity changes over 1000 h, using 55 % glycerol concentration. After reaching equilibrium, humidity remains within limits of ±5 % prescribed by JEDEC standard JESD22-A101C for 653 h. Own work, reproduced from [2]. (b) Demonstration of chamber refilling with a 55 % glycerol solution in a second long-term test after a significant drop in RH. The second, smaller drop in humidity is believed to be caused by a brief expulsion of gas from the chamber, due to increasing internal pressure as the partial pressure of water vapor increased. This expulsion reduced the partial pressures of nitrogen and oxygen, balancing the internal and external pressures. Own work, reproduced from [2].

2.1.8 Example Application: Wire Bond Resistance Monitoring

The utility of the chambers by monitoring the electrical resistance of Pd-coated Ag wire bonds, produced as described in [89]. The bonds were tested inside the chamber at 85 °C, using a glycerol concentration of 58 %. The resulting RH and resistance measurements are shown in Fig. 2.10. Bond failures were easily detectable as large increases in resistance.

2.1.9 Conclusions from Humidity System Development

A humidity system and method have been developed, based on pre-existing thermal chambers, well-suited to environmental testing of microelectronics. They are especially suitable for testing the reliabilities of different material combinations, with extrapolation to device working conditions. The system is able to maintain 85 °C and 85 % humidity, a standard condition for microelectronics testing, for extended periods of time. The system is useful to age microelectronic wire bonds while simultaneously measuring bond contact resistance values.

The system is limited by inability to maintain pressure differences, so it is not capable of HAST testing, which uses temperatures about 100 °C and requires pressures above 1 atm. Test durations are also limited by gradual moisture leakage from the chamber; the glycerol cup design has since been modified to increase the liquid capacity by 133 %, from 0.18 mℓ to 0.42 mℓ, which is expected to increase the time maximum time between refills by the same percentage.

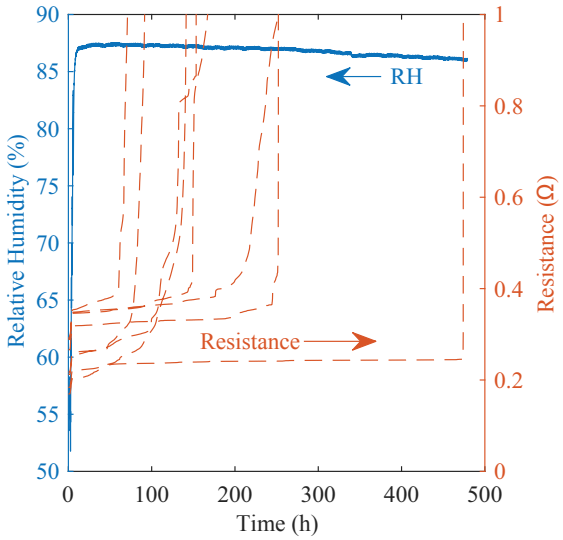

Fig. 2.10: Example application of chamber. Solid line: relative humidity inside chamber at 85 °C with 58 % glycerol solution. Dashed lines: electrical resistance measurements of wire bonds in chamber. Own work, reproduced from [2].

2.2 Temperature Calibration of Mini-Ovens

Early experiments using the mini-oven racks of Section 1.5.1 showed significant variation between identically-prepared samples in different ovens. For example, Figs. 2.11 (a) and (b) show resistance measurements from Au and PCS wire samples, respectively. Such discrepancies indicate an uncontrolled factor in sample preparation or testing that would degrade statistical precision and weaken or invalidate any conclusions drawn from the data.

A possible explanation for inconsistencies in the aging results is inaccuracy in sample temperatures during testing. Therefore, a temperature calibration procedure was performed for each mini-oven prior to beginning experiments on large numbers of samples in Chapter 4.

The mini-oven design is vulnerable to temperature inaccuracies from three different sources:

- Source 1: Asymmetry in oven construction
- Source 2: Temperature sensor miscalibration
- Source 3: Inconsistent contact between heater and ceramic substrate

The following sections first show that there is inconsistency between the temperatures of different ovens, given the same nominal temperature. Then each of the three causes is investigated

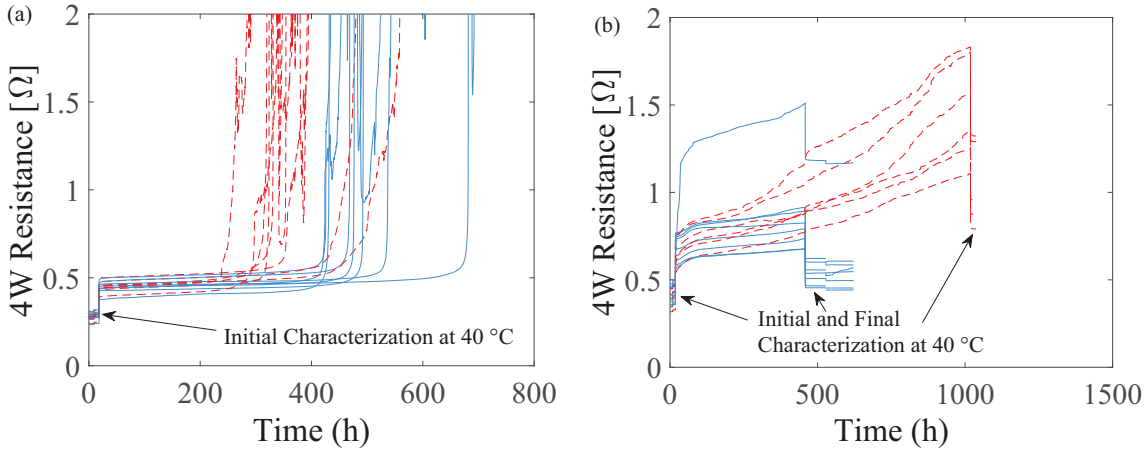

Fig. 2.11: Wire pair resistance data curves showing discrepancy between equivalent samples tested in different ovens at 200 °C. Two different colours correspond to wire pairs in two different ovens. (a): Au wires. Six of eight red samples failed before any blue samples. (b): PCS wires. Initial resistances were similar between the two ovens, but resistances increased consistently faster for samples shown in red.

to determine whether it can account for the observed inconsistency. Finally, an improvement in temperature accuracy is presented, using graphite thermal interface pads between the heater and the ceramic substrates. With this improvement, the ovens could reliably operate at 225 °C, which had not previously been possible.

2.2.1 Left-Right Temperature Offset Measurements

To test for oven temperature inconsistency, two temperature sensors were placed in the same oven, and values from both sensors were recorded over a range of nominal temperatures from ambient to 225 °C, following the temperature profile shown in Fig. 2.12 (a). In the ideal case, the difference between left and right side measurements would be small. However, after testing 20 ovens, there were differences up to 8 °C at 225 °C, with example data shown in Fig. 2.12 (b). For a typical activation energy of 1 eV, an 8 °C temperature change from 225 °C to 233 °C corresponds to a 28 % decrease in lifetime according to the Arrhenius Eq. (1.28), which could severely influence reliability results.

To investigate the causes of the temperature offsets, the temperature sensors in each oven were interchanged, and experiments repeated. If the offsets were caused only by oven asymmetry, the

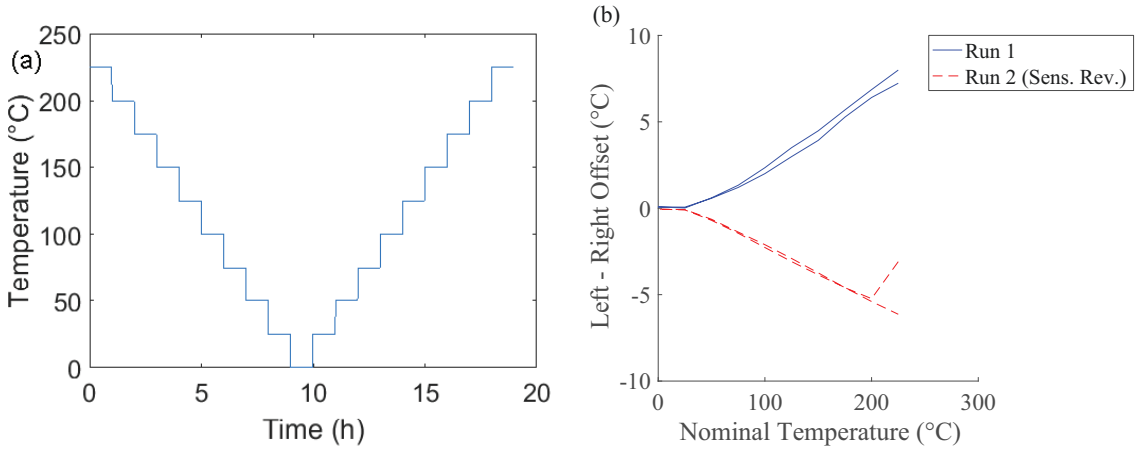

Fig. 2.12: (a) Temperature program for measurement of left-right temperature offset in mini-ovens. Temperature setting of 0 °C at 9 h disables heating, allowing oven to reach ambient temperature. (b) Worst-case temperature offset of up to 8 °C between sides of one mini-oven (left minus right). Experiment performed twice, with sensors interchanged for run 2 (red data). Two near-parallel lines appear for each run, corresponding to heating and cooling phases of the experiment, as described in Fig. 2.12.

measured offsets would be the same as in the previous tests. Fig. 2.12 (b) clearly shows a change in the offset after interchanging the sensors, indicating that oven asymmetry (Source 1) does not sufficiently account for the temperature inconsistency between ovens.

2.2.2 Calibration Using Melting Point of Sn-Pb Eutectic Solder

The next step was to test whether temperature sensor miscalibration (Source 2) can explain the temperature inconsistencies. The Pt100 sensors used are Class B, which implies a temperature error of at most 1.3 °C below 200 °C, which would not explain the 8 °C difference in Subsection 2.2.1. However, verification is still worthwhile, since the electrical system used to measure the Pt100 sensors may be inaccurate. Therefore temperature measurement accuracy was tested based on the melting point of Sn-Pb eutectic solder.

Three samples of Sn-Pb eutectic solder on ceramic substrates were produced as part of [90]. One of these samples is shown in Fig. 2.13. On each of these samples, a small amount of solder spanned four leadfingers of the substrate. Each sample was placed in one of the ovens and a precise four-wire resistance measurement was taken across the solder during heating and cooling. From a plot of resistance vs. time, as in Fig. 2.14 (a), the times of melting and solidification were identified by sharp changes in resistance. For more precise identification, the measured resistance was plotted against measured temperature, with MATLAB's smoothing spline function used to interpolate the data. The transition point was identified as the temperature corresponding to the maximum slope of the spline curve, as illustrated in Fig. 2.14. The measured transition temperatures were compared to the known melting point of 183 °C for the Sn-Pb eutectic composition, which consists of 61.9 % Sn by weight [91]. Such comparisons are shown in Fig. 2.15. The melting point was used rather than the solidification point these comparisons, since solidification may be delayed by nucleation effects, resulting in an inaccurately low measurement.

Such trials were performed 16 times in 9 ovens, including several repetitions in some ovens to assess reproducibility. The solder samples were removed and replaced between trials to test for variation in contact between the heaters and substrates. Fig. 2.15 demonstrates that the observed melting and solidification temperatures vary significantly between multiple trials in the same oven, indicating that sensor miscalibration (Source 2) also does not account for the inconsistent temperatures observed in 2.2.1, so that inconsistent contact (Source 3) must be the dominant contributing factor.

2.2.3 Graphite Thermal Interface Pads for Consistent Heat Transfer

Sections 2.2.1 and 2.2.2 demonstrate that the temperature inconsistencies were likely due to poor reproducibility of the contact between the heaters and ceramic substrates. To eliminate this

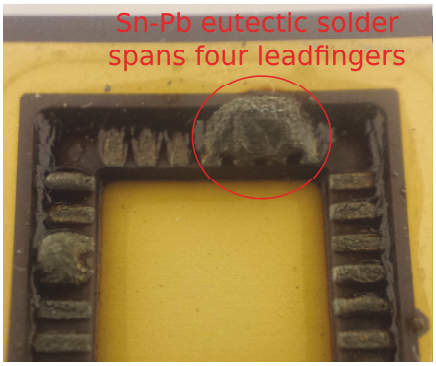

Fig. 2.13: Sample of Sn-Pb eutectic solder on ceramic substrate, used for calibration of mini-oven temperatures. Sudden increase in electrical resistance is detected by four-wire measurement and indicates known melting point of 183 °C.

problem, thermal interface pads were added between the heaters and ceramic substrates, similar to the elastomer material described in Section 2.1.3, but with no moisture sealing requirement. The elastomer was not suitable in this case, because its maximum temperature rating is 125 °C, much less than the 225 °C planned for high-temperature aging. Instead, 0.51 mm thick sheets of graphite with at least 98 % purity (manufactured by Laird PLC, London, UK, part #A10464-01) were used, which have a temperature rating of 300 °C. The sheets were cut using the same punch and die as in 2.1.3, with a typical pad shown in Fig. 2.16 (a). The set screws of the mini-oven clamps were adjusted so that the graphite was compressed to 80 % of its original thickness.

Repeating the melting procedure and the spline fitting illustrated in Fig. 2.14 (b), for 19 ovens, the temperature repeatability was greatly improved compared to Sections 2.2.1 and 2.2.2, with a mean value of 180.6 °C for the measured melting point, and a standard deviation of 0.6 °C, illustrated in Fig. 2.16 (b). In the remainder of this thesis, since testing several sensors in an ice water bath made from deionized water gave readings of 0 °C, the remaining error is compensated by assuming perfect accuracy at 0 °C and an offset of 2.4 °C at an actual temperature of 183 °C, then linearly interpolating or extrapolating this error to other temperatures as required.

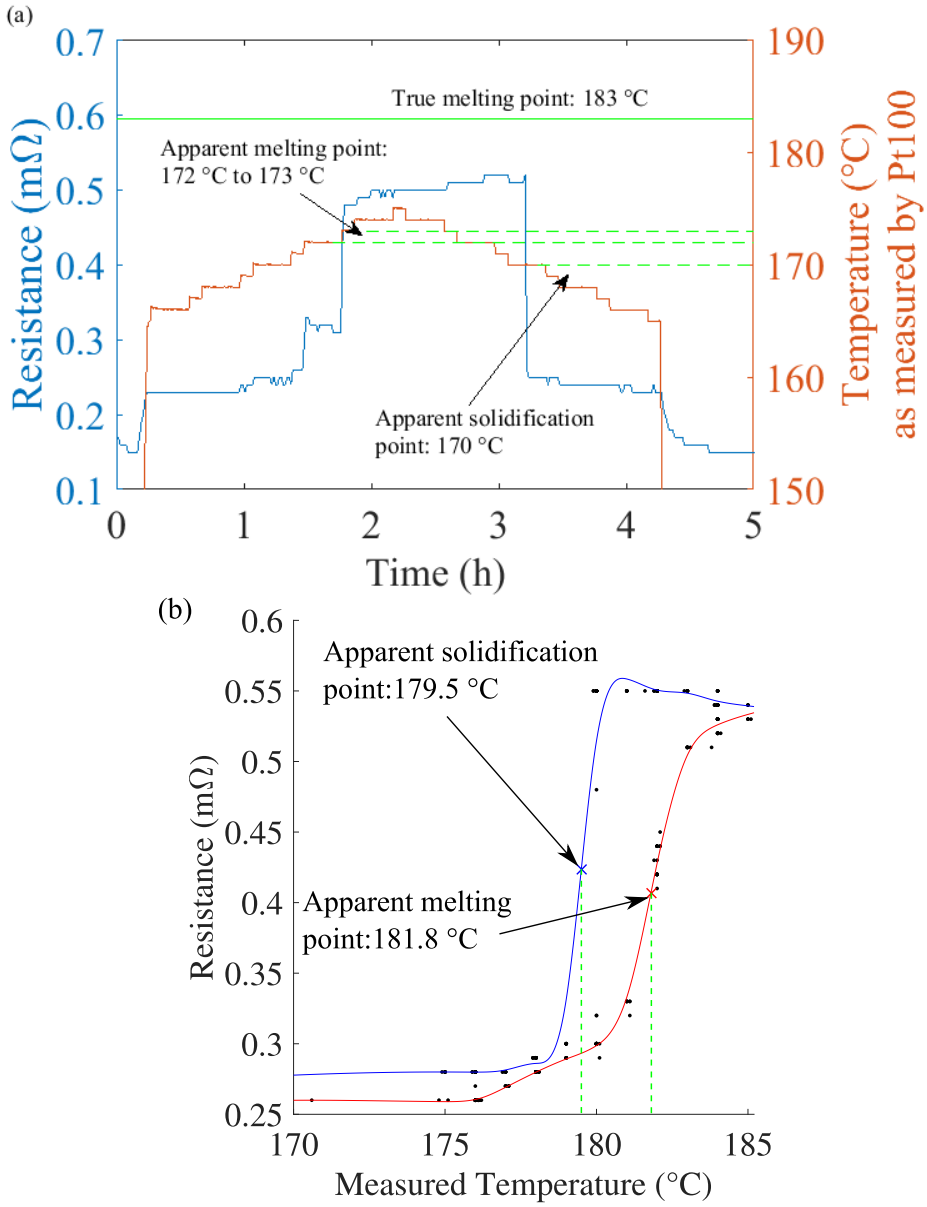

Fig. 2.14: (a) Resistance and temperature curves for a single calibration trial with eutectic Sn-Pb solder. Sharp increase in resistance indicates approximate observed melting point between 172 °C and 173 °C, well below the true melting point of 183 °C. (b) Resistance vs. temperature plot with smoothing spline fit for a different calibration trial. Melting and solidification points are identified as the points of maximum slope of the fitted spline and indicated with "x" markings.

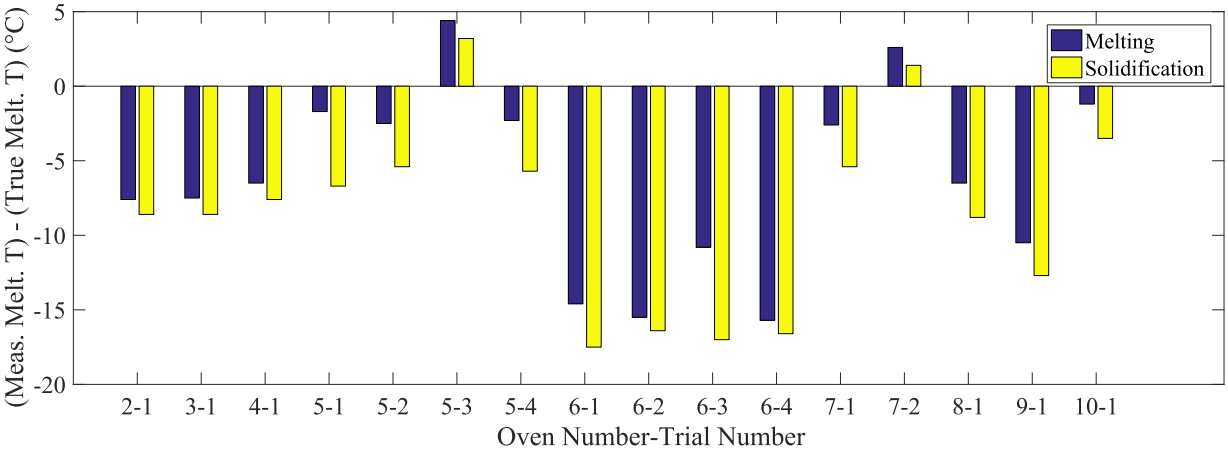

Fig. 2.15: Differences between measured and true melting temperatures for each of 16 calibration trials. Inconsistencies between different trials in the same oven demonstrate that Sources 1 and 2 of inaccuracy together are insufficient to explain the temperature inconsistencies between ovens.

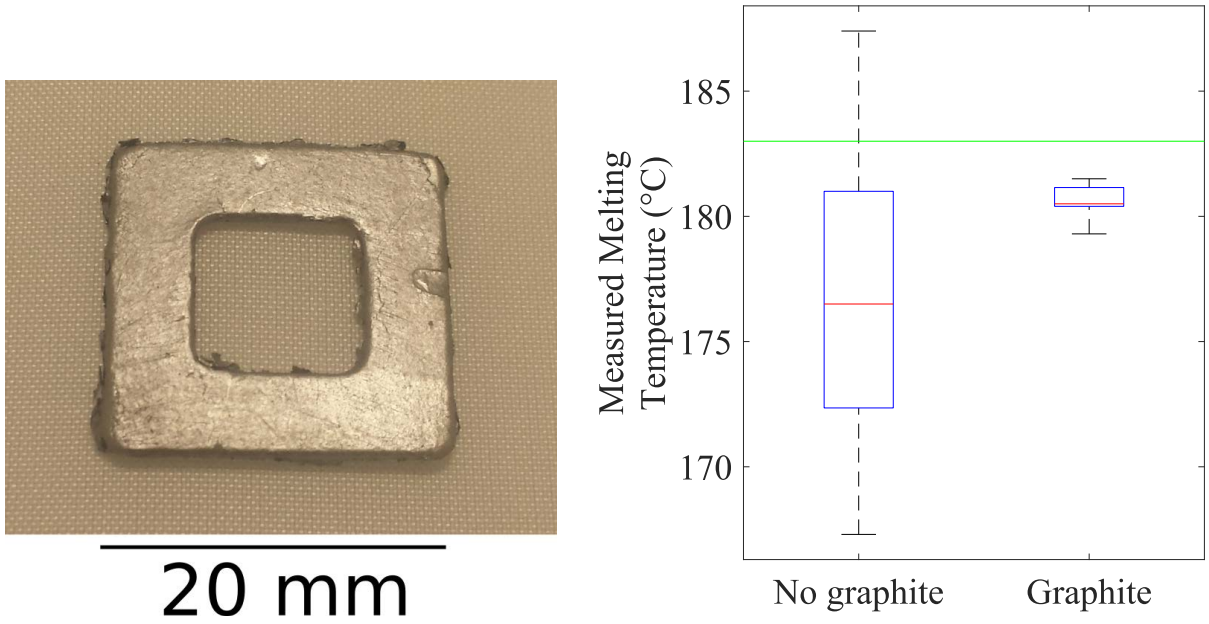

Fig. 2.16: (a) Graphite thermal interface pad, used to ensure good thermal contact between mini-oven heater block and ceramic substrates. (b) Box plots of measured melting points. Left: 16 trials without graphite pads. Right: 19 trials with graphite pads, demonstrating greatly improved repeatability. No outliers removed.

Chapter 3

Process Development

This chapter describes the development of ball bonding processes used to produce the results in Chapter 4. These processes were developed in four stages: first, Section 3.1 describes a simple optimization of a PCC bonding process using the Gomes method [92] for the pilot study in Section 4.2. Section 3.2 augments this method with additional statistical analysis. Section 3.3 describes a more detailed optimization procedure for PCC bonds, including additional process parameters and minimizing the diameter of the Al pad splash. Finally, to compare reliabilities for PCC and bare Cu bonds and for different bond sizes, Section 3.4 describes the development of four additional bonding processes. Section 3.5 concludes the chapter and summarizes the six processes developed, including their use in Chapter 4.

This section presents the development of a first bonding process used in the reliability experiments of Chapter 4. The procedure used is based on the Gomes method [92], so the first subsection serves to illustrate the method before various extensions are described in the following subsections.

3.1 Pilot Experiment

3.1.1 Description of Gomes Optimization Process

In the Gomes method, three process responses are considered: bonded ball diameter (defined as the ball diameter at the capillary imprint, or BDC), ball height (BH), and shear strength (SS). Shear strength is defined as the force measured by a standard ball shear test divided by the bond area,

$$\mathrm{SS} = \frac{F}{\pi(\mathrm{BDC}/2)^2}. \tag{3.1}$$

Simultaneous optimization of three responses is challenging, so knowledge of the process mechanisms is used to guide and simplify the procedure.

There are two main steps involved in bonding the FAB to the pad metallization. First is the impact step, with a large downward force and little or no ultrasonic vibration. During impact the large force applied causes deformation of the FAB. Second is the bonding step, which uses a lower downward force than the impact step, and uses ultrasonic vibration to make a strong bond. Although the force during the bonding step is low, deformation can still occur if the US power is sufficiently large; if this happens, it is known as ultrasonically-enhanced deformation (UED) [93]. For good bonding, UED is not essential and is often a sign of excessive US power. Thus, optimization of these two process steps can be separated into two different optimization stages, resulting in a set of optimized factors that constitute a candidate process. The factors are introduced on the next paragraph. After the two optimization stages, additional bonds are produced with the candidate process to confirm that the responses meet the requirements. These process steps are summarized visually in Fig. 3.1.

In stage 1, the EFO and impact processes are optimized to produce the desired geometry, defined in terms of the BDC and BH, which are measured using an optical microscope. The US power at this stage is low to avoid UED, but high enough so that the bonds stick reliably to the pads. The machine parameters to be optimized are the impact force (IF), and either the EFO time (t_{EFO}) or the EFO current (I_{EFO}). Gomes optimized two parameters, EFO time and IF, to achieve a target BDC and BH simultaneously. In this work, EFO current was optimized with EFO time

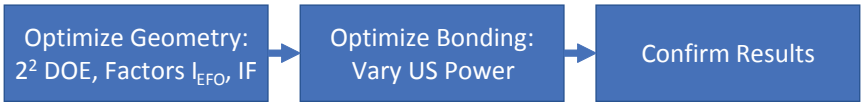

Fig. 3.1: Diagram of three main steps in the Gomes optimization procedure [92]. First, the geometry is optimized using a 2^2 full factorial experiment to obtain the correct BDC and BH. Second, the US power is increased until the desired (or maximum) shear strength is reached. Finally, additional bonds are made to confirm the results.

held constant, since these two parameters have similar effects, and the wire bonder used here was an ESEC 3088, which allows adjustment of EFO current in finer increments than EFO time.

The factors I_{EFO} and IF are optimized using a 2^2 full-factorial design of experiment (DOE). The notation of an x^y DOE means that y factors are tested, with x levels for each. In a full-factorial experiment, all possible combinations of factor levels (runs) are tested, usually with multiple samples per run. The number of runs required is x^y. Fractional factorial experiments, with a smaller number of runs, are also possible, and are discussed in Section 3.3.2. Using a 2^2 DOE allows the responses to be estimated for a given parameter combination, anywhere within the two-dimensional range of levels tested.

In stage 2, the US power is varied to obtain a maximum or target value of shear strength. Typically, there is a threshold value below which UED does not occur, so that the geometry obtained in Stage 1 remains consistent, and the maximum SS is obtained near this threshold. Particularly with Cu wire, shear strength should not necessarily be maximized, since the high US power required can reduce yield due to cratering of the Si substrate or short-circuits caused by excessive pad splash.

After finding a set of candidate process using this procedure, additional bonds are made to verify that the target geometry and shear strength are reached.

3.1.2 Materials, Process Targets, and Constant Factors

Bonds for this optimization procedure were made on 800 nm thick pad metallization on Si dies. The bonding capillary used was model SBNE-35BD-AZM-1/16-XL (Small Precision Tools, Inc., Petaluma, CA, USA). The target BDC was chosen as 58 µm to match Gomes' work [92] using the same capillary model. In this preliminary study, a target BH was not immediately set. Instead, after producing geometry data in Stage 1, a judgment was made regarding the most suitable BH value, from those attainable within the range of parameters tested, as explained further in Subsection 3.1.3.

The second column of Table 3.1 shows the starting process parameters used for the geometry optimization, including two levels for IF and I_{EFO}. The heating stage temperature was chosen to be 175 °C. Bond force was chosen by first considering bond stress (BS), the bond force (BF) divided by target bond area,

$$\mathrm{BS} = \frac{\mathrm{BF}}{\pi(\mathrm{BDC}/2)^2}. \tag{3.2}$$

Following Gomes [92], a bond stress of 75 MPa is chosen, giving a bond force of 198 mN. Nitrogen shielding gas was used to prevent oxidation during FAB formation. The shielding gas flow rates through the machine's front nozzle and wand nozzle were 0.35 ℓ/min and 0.5 ℓ/min, respectively, giving good quality FABs as seen in Fig. 3.2.

3.1.3 Stage 1: Geometry Optimization

To optimize the geometry, five bonds were produced and measured for each of the four factor combinations. A contour plot showing lines of fixed BDC and BH as functions of I_{EFO} and IF is shown in Fig. 3.3. The MATLAB code used to generate this plot was based on that used in [92] and is given in Appendix C.1 as DOE_Complete_Program.m. At this stage, a BDC of 57.5 µm was chosen on the plot, to allow a small amount of UED in the final process. From this plot, a target BH of 22 µm was chosen, since this was the lowest value attainable within the parameter range tested; production processes typically use even lower values of BH [3]. Given these targets, values of 63.41 mA and 596 mN for I_{EFO} and IF, respectively, were identified from the intersection of the appropriate contours in Fig. 3.3.

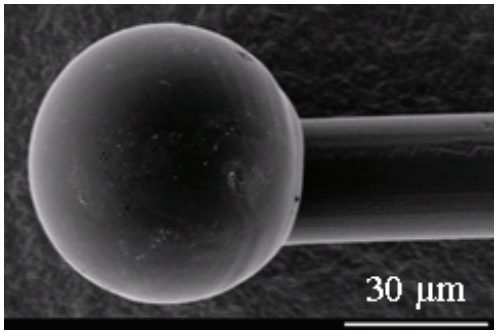

Fig. 3.2: SEM image of typical PCC FAB.

Table 3.1: Bond parameters for pilot experiment.

Parameter Name	Initial	Final
Temperature (°C)	175	175
Ball Impact Force (mN)	**400/1000**	**596**
Ball Bond Force (mN)	198	198
Bond Stress (MPa)	75	75
Ultrasonic Time (ms)	15.2	15.2
Ultrasonic Power (%)	**27.99**	**28.63**
Pre-Ultrasonic Power (%)	6.5	6.5
EFO Current (mA)	**63.14/70.00**	**63.41**
EFO Time (ms)	0.7	0.7
Tail Length (µm)	500	500
N_2 Gas Flow Rate (L/min, each nozzle)	0.3	0.3

3.1.4 Stage 2: Bond Strength Optimization

Using the optimized geometry parameters found in Section 3.1.3, four US power settings were tested, starting from the initial value of 27.99 %, and increasing in steps of approximately 3 %: 27.99 %, 31.02 %, 34.00 %, and 36.98 %. The shear testing machine used was a Dage 4000 (Nordson DAGE, Aylesbury, UK), with a BS250 shear testing cartridge. The measured shear strengths are plotted in Fig. 3.4. A target shear strength of 120 MPa was chosen for this process, so the optimum US was taken to be 28.63 %, which was the intersection between the horizontal line at 120 MPa and the interpolating line joining the mean shear strength for each measurement group.

The final bond parameters are shown in the third column of Table 3.1. Fourteen bonds were made using these parameters; the mean resulting shear strength was 114 MPa, with a standard deviation of 8 MPa.

3.2 Application of Linear Regression Analysis to Process Development

This section demonstrates an application of the statistical concepts in Section 1.6 to ball bond process development, extending the Gomes optimization procedure [92]. The data set used is a subset of the data published in [94] and presented again in Section 3.3; portions of the full data set are omitted from this section for clarity of presentation.

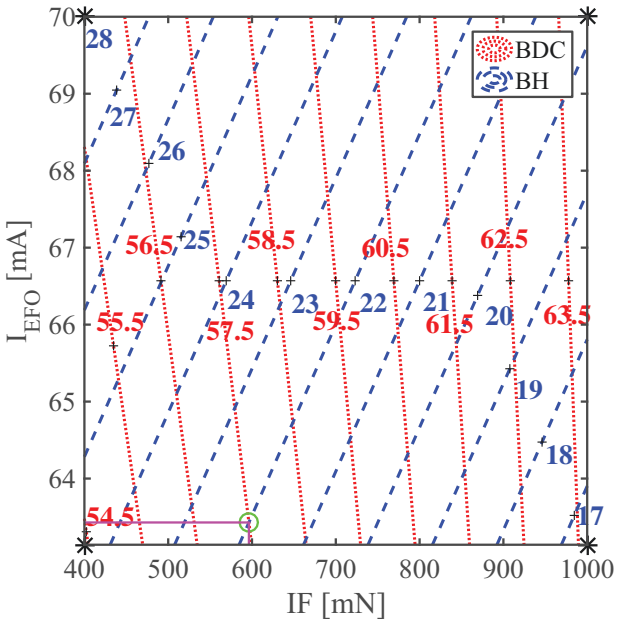

Fig. 3.3: Contours of fixed BDC and BH as I_{EFO} and IF vary, calculated using DOE_Complete_Program.m in Appendix C.1. Target values of 57.5 µm BDC and 22 µm BH are indicated with contour lines, and their intersection is marked with a circle, located at the predicted factor values I_{EFO} = 63.41 mA and IF = 596 mN.

3.2.1 Stage 1: Optimizing FAB Size, Impact

In Stage 1 of the process, the electric flame-off current (I_{EFO}), which determines FAB size, and the impact process were adjusted to achieve the target ball bond geometry. A BDC target of 61 µm was determined by referring to [3]: first, a 90 µm pitch process was chosen as suitable for 25 µm diameter wire and the ESEC 3088 wire bonder used in these studies. Next, the target BDC of 61 µm was chosen, given by [3] as a typical value for such a process. The target height for this demonstration is 14 µm; Section 3.3 explains why this value was chosen. The substrate heating block temperature was 175 °C.

The parameters, US, BF, and UT were held constant in stage 1, since they are applied after impact, and therefore do not affect the geometry if ultrasound enhanced deformation (UED) is avoided [8]. A 2^2 factorial experiment was performed, with IF and I_{EFO} as the factors. The parameters used at this stage are listed in Tables 3.2 and 3.3. Initially, four bonds were produced for each of the 4 factor combinations. Diameter and height were measured for each bond, with a typical diameter measurement shown in Fig. 3.5. The factor settings and resulting geometry measurements are given in Table 3.4.

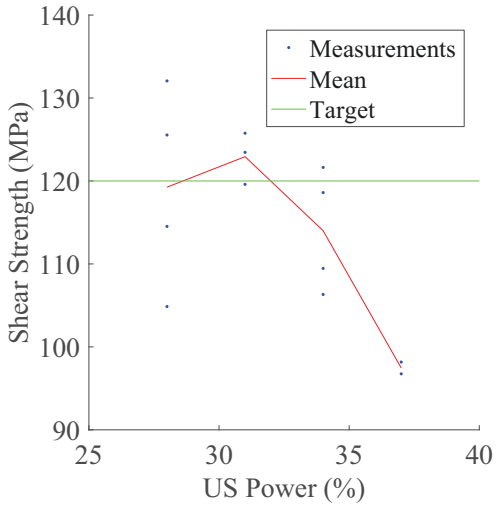

Fig. 3.4: Dependence of shear strength on US power for pilot experiment. The target value was 120 MPa; a US setting of 28.63 % is estimated from the plot to achieve this target.

Bond Geometry Models

Linear regression models with interaction terms were used to describe the influence of the two factors on diameter and height. The procedure for applying these models is illustrated in Fig. 3.6. For a single measurement, the model for BDC is

$$\mathrm{BDC} = d_0 + d_1 \cdot I_{\mathrm{EFO}} + d_2 \cdot \mathrm{IF} + d_3 \cdot I_{\mathrm{EFO}} \cdot \mathrm{IF} + \varepsilon_{\mathrm{BDC}}, \tag{3.3}$$

and likewise for BH,

$$\mathrm{BH} = h_0 + h_1 \cdot I_{\mathrm{EFO}} + h_2 \cdot \mathrm{IF} + h_3 \cdot I_{\mathrm{EFO}} \cdot \mathrm{IF} + \varepsilon_{\mathrm{BH}}, \tag{3.4}$$

where ε is a normally-distributed error term. The mean of ε is assumed to be zero, with standard deviations σ_{BDC} and σ_{BH}, respectively, for the two models.

The coefficients d_0 to d_3 are determined by least squares regression, as follows. The general procedures and equations are given in Section 1.6. Here the procedure is demonstrated for this particular BDC model; the same procedure applies for the BH model. These calculations are also implemented in many mathematical software packages, for instance using the fitlm function in MATLAB or the LinearRegression function in Octave.

For the full set of 16 measurements, Eq. (3.3) can be rewritten in a matrix form as

$$\mathbf{BDC} = \mathbf{X} \cdot \mathbf{D}, \tag{3.5}$$

Table 3.2: Parameters held fixed during optimization procedure.

Parameter	Value
Heater Temperature (°C)	175
EFO Time (ms)	0.7
Tail Length (μm)	400
Electrode to Wire distance (μm)	350
Ball PUS (%)	0
Wedge IF (mN)	700
Wedge BF (mN)	700
Wedge UT (ms)	9.8
Wedge US (%)	35
Wedge PUS (%)	6.5
Bond Pad Thickness (nm)	3000

Table 3.3: Parameter settings for 2^2 factorial geometry DOE. The ball US, BF, and UT were held constant for this stage of the optimization.

DOE Parameters	Low	High
IF (mN)	500	1000
I_{EFO} (mA)	54.9	65.06
Fixed Parameters		
US (%)	0	
BF (mN)	700	
UT (ms)	15.2	

with

$$\mathbf{X} = \begin{bmatrix} 1 & I_{\text{EFO}}(1) & \text{IF}(1) & I_{\text{EFO}}(1)\cdot\text{IF}(1) \\ 1 & I_{\text{EFO}}(2) & \text{IF}(2) & I_{\text{EFO}}(1)\cdot\text{IF}(2) \\ \vdots & \vdots & \vdots & \vdots \\ 1 & I_{\text{EFO}}(16) & \text{IF}(16) & I_{\text{EFO}}(1)\cdot\text{IF}(16) \end{bmatrix}, \tag{3.6}$$

$$\mathbf{D} = \begin{bmatrix} d_0 \\ d_1 \\ d_2 \\ d_3 \end{bmatrix}, \tag{3.7}$$

and **BDC** is a 16×1 column vector of measured diameters, given as the third column of Table 3.4.

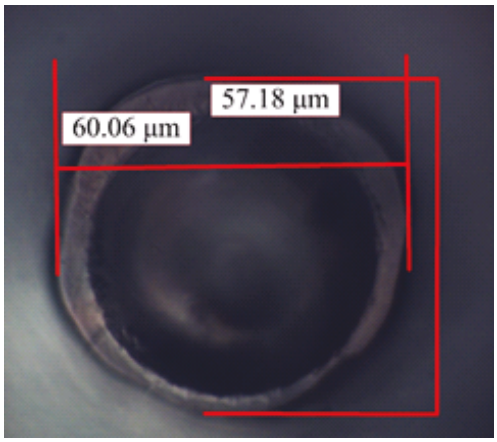

Fig. 3.5: Typical measurement of BDC from optical micrograph.

Table 3.4: I_{EFO} and IF settings, and corresponding geometry responses, for 16 bonds produced in 2^2 factorial experiment for geometry characterization. Values are presented in order of production.

I_{EFO} (mA)	IF (mN)	BDC (µm)	BH (µm)
65.06	500	54.270	25
65.06	1000	61.815	18
54.90	500	54.195	16
54.90	1000	60.470	12
54.90	1000	60.465	10
65.06	1000	62.440	19
54.90	500	53.115	14
65.06	500	54.510	24
65.06	500	55.305	25
65.06	1000	62.825	18
54.90	1000	60.585	11
54.90	500	52.830	15
65.06	500	54.580	25
54.90	500	53.755	15
54.90	1000	61.055	10
65.06	1000	63.815	19

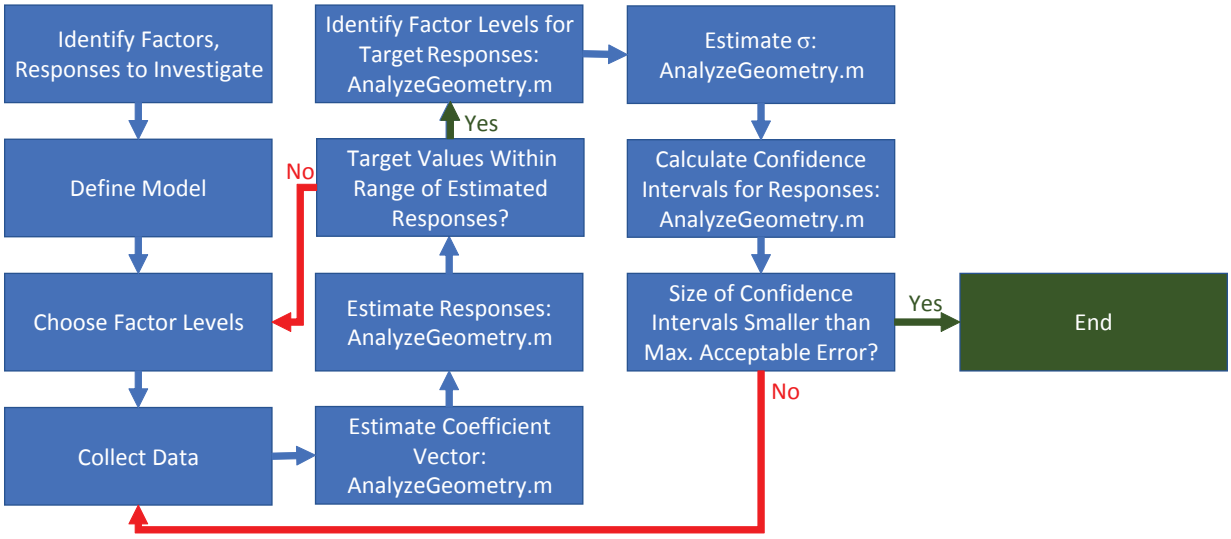

Fig. 3.6: Process flow diagram for defining, fitting, and evaluating linear models. The MATLAB file AnalyzeGeometry.m in Appendix C.2 implements the calculations required.

Linear Regression by Least Squares

The least squares estimate for D is

$$\hat{\mathbf{D}} = (\mathbf{X}'\mathbf{X})^{-1}\mathbf{X}' \cdot \mathbf{BDC} = \begin{bmatrix} 44.7 \\ 0.0300 \\ 0.00475 \\ 0.000175 \end{bmatrix}, \tag{3.8}$$

with values measured in μm. Using this estimate, the mean diameter response can be predicted for a given combination of I_{EFO} and IF. Defining a vector

$$\mathbf{x} = \begin{bmatrix} 1 & I_{EFO} & \text{IF} & I_{EFO} \cdot \text{IF} \end{bmatrix}, \tag{3.9}$$

the estimated response is

$$\widehat{\text{BDC}}(\mathbf{x}) = \mathbf{x} \cdot \hat{\mathbf{D}}. \tag{3.10}$$

After evaluating $\widehat{\text{BDC}}(\mathbf{x})$ over the full range of I_{EFO} and IF values tested, these results were used to generate contours of fixed $\widehat{\text{BDC}}$, similar to those in Fig. 3.3. Contours of fixed BH were produced by the same method, then the intersection of the two target contours gave the recommended machine settings of $I_{EFO} = 58.77$ mA and IF $= 971$ mN, obtained using the file AnalyzeGeometry.m in Appendix C.2.

Estimating Confidence Limits

Next, the variations in the measurements and fitted estimates were examined. Using Eq. (1.9), the sum of squared errors is

$$\mathrm{SSE} = \mathbf{BDC}' \cdot \mathbf{BDC} - \hat{\mathbf{D}}' \cdot \mathbf{X}' \cdot \mathbf{BDC} = 4.08\,\mu\mathrm{m}^2, \tag{3.11}$$

where **BDC** is the vector of measured diameters and $\hat{\mathbf{D}}$ is the vector of estimated coefficients, calculated from Eq. (3.8).The estimate for σ, the standard deviation of the BDC measurements with fixed machine settings, is

$$\hat{\sigma} = \sqrt{\frac{\mathrm{SSE}}{n-p}} = 0.583\,\mu\mathrm{m}, \tag{3.12}$$

where $n = 16$ is the number of bonds measured, and $p = 4$ is the number of coefficients in the vector **D**.

The variation in $\widehat{\mathrm{BDC}}(\mathbf{x}_{\mathrm{opt}})$ over many experiments is estimated using the quantity (1.17), evaluated for $\mathbf{x} = \mathbf{x}_{\mathrm{opt}}$:

$$\frac{\mathrm{BDC}(\mathbf{x}_{\mathrm{opt}}) - \widehat{\mathrm{BDC}}(\mathbf{x}_{\mathrm{opt}})}{\hat{\sigma}\sqrt{\mathbf{x}'_{\mathrm{opt}}(\mathbf{X}'\mathbf{X})^{-1}\mathbf{x}_{\mathrm{opt}}}}, \tag{3.13}$$

which has a t distribution with $n-p$ degrees of freedom, as explained in Section 1.6.4. By the choice of $\mathbf{x}_{\mathrm{opt}}$, $\widehat{\mathrm{BDC}}(\mathbf{x}_{\mathrm{opt}}) = 61\,\mu\mathrm{m}$. So 95 % confidence bounds for $\mathrm{BDC}(\mathbf{x}_{\mathrm{opt}})$ are

$$61\,\mu\mathrm{m} \pm t_{0.025,12}\hat{\sigma}\sqrt{\mathbf{x}'_{\mathrm{opt}}(\mathbf{X}'\mathbf{X})^{-1}\mathbf{x}_{\mathrm{opt}}}. \tag{3.14}$$

The results of this calculation are $61.00\,\mu\mathrm{m} \pm 0.44\,\mu\mathrm{m}$ and $14.00\,\mu\mathrm{m} \pm 0.55\,\mu\mathrm{m}$ for $\mathrm{BDC}(\mathbf{x}_{\mathrm{opt}})$ and $\mathrm{BH}(\mathbf{x}_{\mathrm{opt}})$, respectively. Equivalently stated, it can be predicted from the data that, with 95 % confidence,

$$61.00\,\mu\mathrm{m} - 0.44\,\mu\mathrm{m} \le \mathrm{BDC}(\mathbf{x}_{\mathrm{opt}}) \le 61.00\,\mu\mathrm{m} + 0.44\,\mu\mathrm{m}, \tag{3.15}$$

and similarly,

$$14.00\,\mu\mathrm{m} - 0.55\,\mu\mathrm{m} \le \mathrm{BH}(\mathbf{x}_{\mathrm{opt}}) \le 14.00\,\mu\mathrm{m} + 0.55\,\mu\mathrm{m}. \tag{3.16}$$

For the final process, a mean error of at most 0.5 µm is desired for BDC and BH, i.e.

$$|\mathrm{BDC}(\mathbf{x}_{\mathrm{opt}}) - 61\,\mu\mathrm{m}| \le 0.5\,\mu\mathrm{m}, \tag{3.17}$$

and similarly for BH. The confidence bounds for BDC indicate that this is likely to be achieved, but for BH it may not be, because of the larger confidence interval. To increase confidence, 16 more

bonds were produced using the same parameters for additional height measurements. Repeating the calculations with all 32 BH measurements, the new optimized machine settings were $I_{\mathrm{EFO}} = 59.05$ mA and IF $= 967$ mN. New confidence bounds for BDC and BH were $61.00\,\mu\mathrm{m} \pm 0.43\,\mu\mathrm{m}$ and $14.00\,\mu\mathrm{m} \pm 0.45\,\mu\mathrm{m}$, respectively. Fig. 3.7 shows contour plots of the BDC and BH estimates using the 16 BDC measurements and 32 BH measurements. The intersection of the BDC and BH target contours is marked, and its coordinates are the recommended values for IF and I_{EFO}. The plot also shows the 95 % confidence region for the parameters, calculated from Eq. (1.20). This region has an elliptical shape centred on the intersection point.

3.2.2 Stage 2: Optimizing Bonding Step

Next, the bonding step was optimized, seeking minimum splash and at least 120 MPa shear strength. In contrast to the Gomes method, the optimization procedure introduced here is based on a central composite design (CCD) with three factors, US, BF, and UT. The CCD was used because it allows estimation of all two-factor interactions and quadratic terms. It was hypothesized that quadratic terms might be important, for instance, there might be an optimal value for BF, with strength decreasing or splash increasing away from this value.

The factor levels for the three-factor CCD experiment consist of a standard 2^3 full factorial DOE, with a central point and 6 star points added. For each star point, two of the factors are set

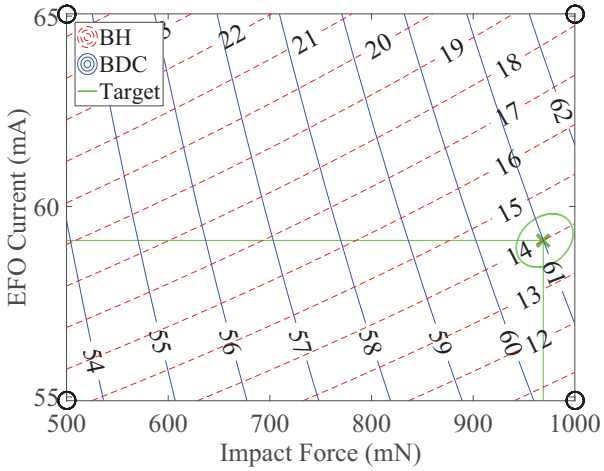

Fig. 3.7: Contour plot of bonded ball diameter and height. Four black circles mark parameter combinations used in the experiment. BDC is constant along solid blue lines, BH along dashed red lines. Green X indicates intersection of target values, and the surrounding ellipse represents a 95 % confidence region.

to their central value, and the third to a value beyond the high or low levels of the 2^3 factorial portion. The star point levels were chosen by following the guidelines in [73]. Twenty-four bonds were produced for the central factor combination, and four for each of the others, except for two unsuccessful bonds discarded as outliers, giving a total of 78. The full sets of five levels for each factor are given in Table 3.5 and illustrated in Fig. 3.8.

The first measured response was the ball shear strength, measured perpendicular to the ultrasonic direction. The second response was the diameter of the displaced Al ("Al splash") along the ultrasonic direction, measured after ball shear, as shown in Fig. 3.9. BDC was also measured to enable shear strength calculation, and to confirm that no UED occurred. Table 3.6 lists the mean responses for each factor combination.

Again, linear models were fitted to the data using least squares regression. The model for shear strength is

$$\begin{aligned} \mathrm{SS} = s_0 &+ s_1 \cdot \mathrm{US} + s_2 \cdot \mathrm{BF} + s_3 \cdot \mathrm{UT} + s_4 \cdot \mathrm{US} \cdot \mathrm{BF} \\ &+ s_5 \cdot \mathrm{US} \cdot \mathrm{UT} + s_6 \cdot \mathrm{BF} \cdot \mathrm{UT} + s_7 \cdot \mathrm{US}^2 + s_8 \cdot \mathrm{BF}^2 + s_9 \cdot \mathrm{UT}^2 + \varepsilon_{\mathrm{SS}} \end{aligned} \tag{3.18}$$

The CCD experiment allows estimation of all interaction and quadratic terms, with the resulting model coefficients and p-values shown in Table 3.7. Here, p-values are used to identify which model terms have statistical significance, commonly defined to be those with $p < 0.05$, providing an indication of which process factors are important. Analysis of p-values was not necessary in Stage 1 (Subsection 3.2.1) because the factors I_{EFO} and IF are both known to be important for the ball geometry.

When examining model coefficients and p-values, especially when including non-linear terms, interpretation is simpler and statistical precision is improved by centring the data. For instance, the machine UT settings in Table 3.5 range from 13 ms to 27 ms. Instead of using these values in the model directly, the median value can be subtracted, defining a centred factor

$$\mathrm{UT}_{\mathrm{cent}} = \mathrm{UT} - 20\mathrm{ms}. \tag{3.19}$$

US and BF were centred similarly, subtracting their medians of 27 % and 292 mN, respectively. These centred values were used when fitting the CCD model, instead of the original off-centre values.

Table 3.5: Factor levels used in CCD experiment.

	Low Star	Low	Mid	High	High Star
US (%)	25.32	26	27	28	28.68
BF (mN)	169	219	292	365	415
UT (ms)	13	15.8	20	24.2	27

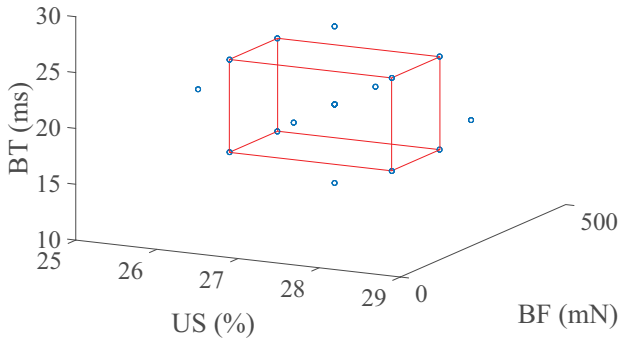

Fig. 3.8: Factor combinations for CCD experiment to investigate quadratic and interaction effects of US power, bond force, and bond time on shear strength and pad splash diameter.

A p-value is a measure of the strength of evidence against a given null hypothesis. After an experiment, an appropriate summary quantity, T, is calculated from the data, and compared to T_0, the value that would be expected, on average, if the null hypothesis were true. If the null hypothesis is true, a large difference $|T - T_0|$ is less likely than a small one. To calculate a p-value, the null hypothesis is assumed to be true, and the p-value is the probability of measuring a difference of size $|T - T_0|$ or larger. Commonly, an effect is said to be statistically significant if the corresponding p-value is less than 0.05.

For the model (3.18), which has ten terms, there are ten null hypotheses to be tested: $s_0 = 0$, $s_1 = 0$, etc. For term j, the appropriate summary quantity is $T_j = \hat{s}_j / \mathrm{se}(\hat{s}_j)$, where $\mathrm{se}(\hat{s}_j)$ is calculated from Eq. (1.8). If $s_j = 0$, then T_j has a student's t distribution with $(n - p)$ degrees of freedom. So the p-value for coefficient j is the probability of obtaining a value with magnitude at least $|\hat{s}_j / \mathrm{se}(\hat{s}_j)|$ from the aforementioned t distribution. Tables of probabilities for t distributions are found in many statistics textbooks, e.g. [73], or the probability can be calculated using statistical software, e.g. with the "tinv" function in either MATLAB or Octave.

The coefficients for the US and splash models, calculated from Eq. (1.5), and the p-values show that shear strength increased with increasing US and UT, consistent with physical intuition. Conversely, increasing BF reduced the shear strength.

Increasing US also increased splash diameter, implying a trade-off between high strength and small splash for the US parameter. BF so it could be chosen to maximize shear strength without consideration of splash. Of the interaction and quadratic terms, only the UT^2 term was statistically significant, with $p > 0.2$ for all other such terms. This term predicts that reducing UT below its central value would increase splash diameter, which is not physically reasonable, so it was discarded when choosing the final parameters. This unphysical result illustrates a known

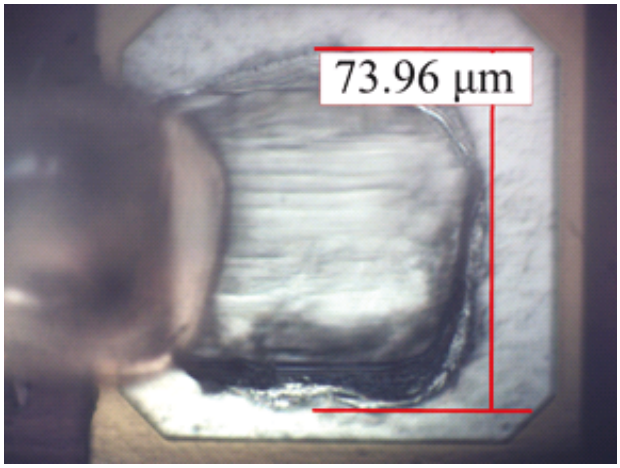

Fig. 3.9: Typical measurement of pad splash diameter along the US direction after shearing ball bond perpendicular to the US direction.

Table 3.6: US, BF, and UT settings, with mean responses, for 15 CCD runs.

Run #	# Meas.	US	BF (mN)	UT (ms)	BDC (µm)	SS (MPa)	Splash D. (µm)
1	4	26	219	20.84	61.201	103.18	77.52
2	4	26	219	29.16	61.781	124.62	78.465
3	4	26	365	20.84	61.338	99.563	76.685
4	4	26	365	29.16	61.710	113.61	78.855
5	4	28	219	20.84	60.979	114.90	78.877
6	4	28	219	29.16	61.093	131.32	79.828
7	3	28	365	20.84	61.943	96.649	78.49
8	4	28	365	29.16	61.815	116.62	80.108
9	3	25.32	292	25	61.755	104.32	76.893
10	4	28.68	292	25	61.150	126.55	78.782
11	4	27	169	25	61.125	118.03	78.7
12	4	27	415	25	61.416	115.64	78.17
13	4	27	292	18	61.432	113.36	80.36
14	4	27	292	32	61.613	119.94	79.36
15	24	27	292	25	61.443	113.88	78.451

Table 3.7: Results of model fitting to central composite design data. Model terms with statistically significant effects ($p < 0.05$) are in bold.

Shear Strength Model Term	Shear Strength Coefficient Estimate	p-Value
Constant	**114.00**	**1.3E-55**
US	**4.24**	**0.0084**
BF	**-0.0488**	**0.022**
UT	**1.41**	**0.00024**
US·BF	-0.0264	0.34
US·UT	-0.0264	0.90
BF·UT	-0.00279	0.67
US^2	-0.119	0.94
BF^2	0.0000525	0.85
UT^2	0.0123	0.88
Splash Model Term	Splash Coefficient Estimate	p-Value
Constant	**78.84**	**4.97E-100**
US	**0.671**	**0.0059**
BF	-0.00135	0.67
UT	0.0688	0.22
US·BF	0.000731	0.86
US·UT	-0.0191	0.79
BF·UT	0.000742	0.46
US^2	-0.250	0.28
BF^2	-0.00000494	0.91
UT^2	**0.0276**	**0.035**

problem when testing many hypotheses at once: if 20 terms that actually have no effects are tested for statistical significance, then, on average, one term would be falsely identified as significant when using a p-value threshold of $0.05 = 1/20$. This problem is not of major concern for this thesis, since the primary goal was to choose a set of parameters that yield good values for the geometry, strength, and splash responses.

To check for UED, a model was also fitted for the BDC response, using the same three factors of US, BF, and UT. In this model, with or without interaction and quadratic terms, the only statistically significant term was the constant term, with $p > 0.1$ for all others. Therefore, as desired, no significant UED occurred in this experiment.

The model results were used to determine an optimum set of parameter values, satisfying the targets of mean shear strength $\geq$ 120 MPa and minimum splash diameter. The final parameters

are given in Table 3.8. The values for I_{EFO} and IF differ slightly from those found in Subsection 3.2.1, because they were actually chosen based on the more comprehensive data in Section 3.3 and in [94]; the responses in Subsection 3.2.3 are based on the parameters in Table 3.8.

Since the selected BF and UT values are both at the extreme limits of the ranges tested, estimates of shear strength and splash for these points are extrapolations outside the fitted range of the model. This extrapolation is a potential source of inaccuracy in predicting process responses for the new parameters. A follow-up experiment can be planned with new ranges for BF and UT to investigate the behaviour in this new area of the parameter space and eliminate the need for extrapolation. Instead, the candidate parameters were tested despite the possible inaccuracy of the responses. The measured responses using these candidate parameters were deemed acceptable, so no further experiments were performed.

3.2.3 Process Responses

Fig. 3.10 shows scanning electron micrographs of typical bonds produced using the optimized parameters. Measured geometry and shear test results from the optimized parameters are presented in Table 3.9. Fig. 3.11 shows the measured responses for 30 bonds, with 15 made on 800 nm thick pads and 15 on 3000 nm pads. Bonds on both pad thicknesses closely met the target diameter of 61 µm and height of 14 µm. The mean shear strength exceeded the target requirement of 120 MPa. The mean splash diameter on 3000 nm pads was 76.4 µm. The Al splash diameter on 800 nm pads was not measured, since splash was a concern primarily for the thicker pads.

Cross-section images of bonded balls were obtained to examine the Al thickness remaining below the bonded ball, and are shown in Fig. 3.12. The mean remaining Al thickness under the ball bonds was estimated to be 500 nm and 1200 nm for the 800 nm and 3000 nm pads, respectively.

Table 3.8: Final optimized bond parameters for first large-scale production process. Small differences from results in Subsection 3.2.1 are explained in the text.

Parameter Name	Value
US Power (%)	27.12
Bond Force (mN)	169
Ultrasound Time (ms)	27
Impact Force (mN)	969
EFO Current (mA)	59.02

Table 3.9: Responses from parameters in Table 6: mean ± standard deviation for 15 bonds on each thickness. Splash was not measured for 800 nm pads because it was primarily of concern for the thicker pads.

Pad Thickness (nm)	800	3000
Ball Diameter (μm)	60.7 ± 0.9	60.9 ± 0.8
Ball Height (μm)	14.1 ± 0.7	14.0 ± 0.8
Shear Force (gf)	37.6 ± 1.8	38.4 ± 3.0
Shear Strength (MPa)	127 ± 8	130 ± 10
Splash Diameter (μm)	Not measured	76.4 ± 1.6

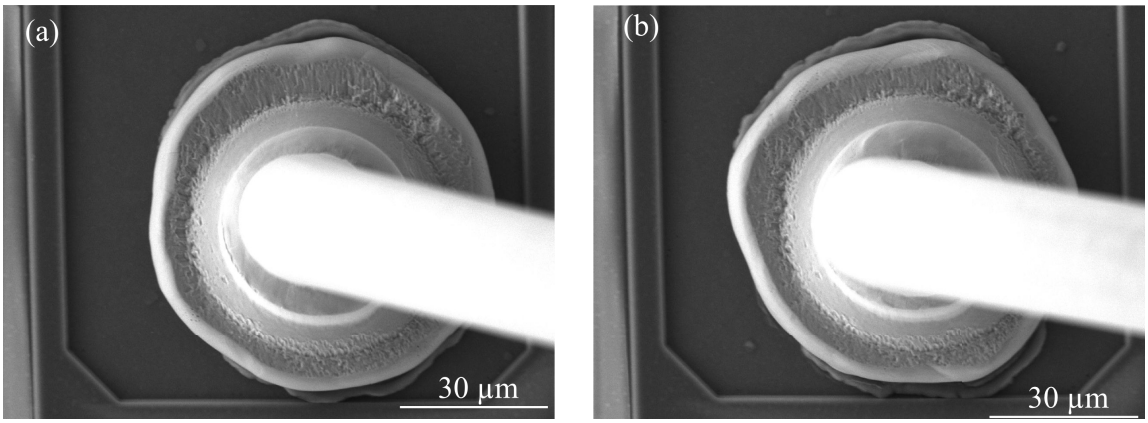

Fig. 3.10: SEM Images of typical ball bonds on (a) 800 nm Al. (b) 3000 nm Al.

Process Capability Estimation

The process capability index, C_{pk}, for a process with mean response μ, standard deviation σ, and upper and lower specification limits USL and LSL, respectively, is defined as

$$C_{pk} = \min \quad \frac{\text{USL} - \mu}{3\sigma}, \frac{\mu - \text{LSL}}{3\sigma} \quad . \tag{3.20}$$

This quantity is easily estimated using Eq. (1.14), together with the estimate $\widehat{BDC}(\mathbf{x}) = \mathbf{x}'\hat{\boldsymbol{D}}$ for the mean response. The file CpkPlot.m in Appendix C.3 implements this calculation. Fig. 3.13 shows estimated C_{pk} values for the bond deformation process, including the dependence on the chosen target geometry. This process has two responses, diameter and height; the overall C_{pk} is taken to be the minimum of the two individual estimates, since the overall yield of a process cannot exceed that of the lowest-yield subprocess. The specification limits are chosen, for the

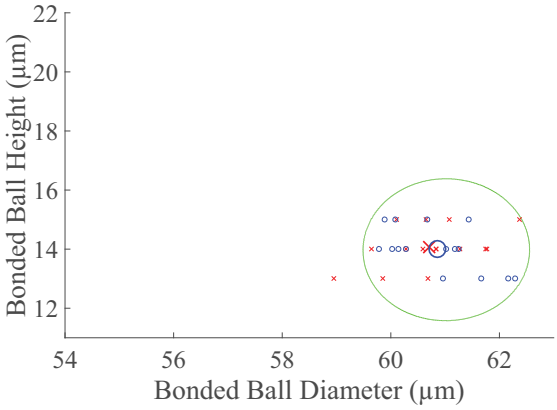

Fig. 3.11: Scatter plot of bond geometry responses from final optimized process. Small red X and blue O markers, 15 of each, represent bonds on 800 nm and 3000 nm thick pads, respectively, with large markers representing mean values for each group. Green curve indicates a 95 % prediction region for individual measurements, generated from Eq. (1.22). On average, 1.5 points would be expected to lie outside the region, so the presence of only one point outside the region indicates good consistency with the model predictions.

purpose of illustration, to be

$$\mathrm{BDC}_{\mathrm{target}} \cdot (1 \pm 0.05) \tag{3.21}$$

for diameter, and

$$\mathrm{BH}_{\mathrm{target}} \cdot (1 \pm 0.25) \tag{3.22}$$

for height. In production, such limits may be determined, for example, by requiring sufficient clearance between adjacent bonds.

Fig. 3.13 shows that C_{pk} worsens as the bonded ball size decreases, illustrating one of the challenges inherent in fine pitch bonding, namely, that tighter control of machine and material variation is required to achieve a robust bonding process.

3.3 First Production Process: Additional Factors Optimized

Meeting Objectives 3. (a), (b), and (c) required a PCC ball bonding process for consistent, good-quality bonds, similar to a mass-production process. This section describes the development of a process meeting these requirements. These results were previously published in [94], and a simplified version of this procedure, based on a reduced data set, was used in Section 3.2 to demonstrate statistical techniques. This section gives the remaining data and explains the

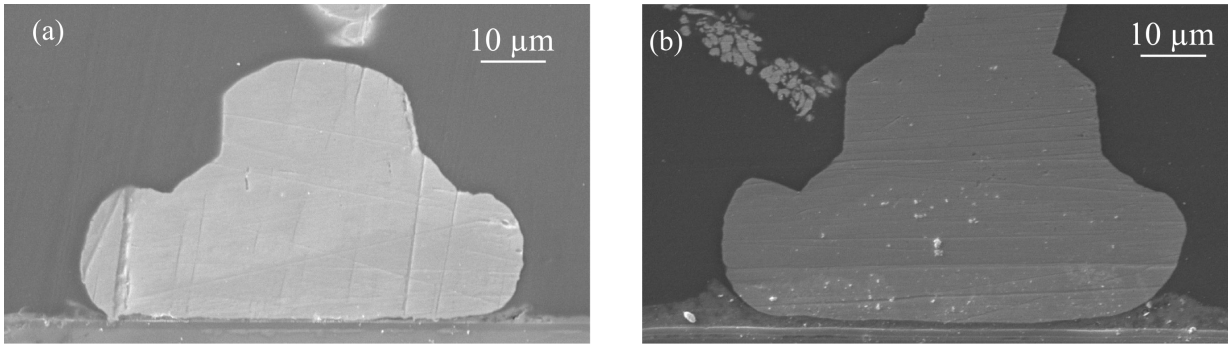

Fig. 3.12: . SEM cross-section images of ball bonds on (a) 800 nm Al pad. (b) 3000 nm Al pad.

optimization of two additional process factors, pre-ultrasonic power and ball height. These which added significant complexity to the procedure: pre-ultrasound because it influences the responses in both stages of the procedure, and ball height (here called a "quasi-factor") because it is a response in Stage 1, but is treated as a factor in Stage 2.

Five factors were identified that may influence bond strength or pad splash:

- Pre-ultrasonic power (PUS)
- Ultrasonic power (US)
- Bond Force (BF)
- Ball Height (BH)
- Ultrasonic Time (UT)

These factors were optimized as follows, using an extension of the Gomes method [92] with additional steps and with statistical analysis as in 3.2.

3.3.1 2^3 DOE for Geometry with Multiple PUS Values

As in Gomes' method [92], process optimization began with finding the correct combination of factor levels to produce the target geometry. Previous sections used two factors, I_{EFO} and IF. Here, PUS, which also influences the bond geometry, was added as a third factor. Three levels for each of BH and PUS were to be used in later process development stages, so the goal for this stage was to find nine combinations of I_{EFO} and IF that all produce the target BDC of 61 µm and, when combined with the three PUS levels, produce each of the three BH levels.

Linear regression models with interaction terms were used to describe the dependence of the BDC and BH responses on the three factors I_{EFO}, IF, and PUS:

$$\begin{aligned}\mathrm{BDC} = {} & d_0 + d_1 \cdot I_{\mathrm{EFO}} + d_2 \cdot \mathrm{IF} + d_3 \cdot \mathrm{PUS} + d_4 \cdot I_{\mathrm{EFO}} \cdot \mathrm{PUS} \\ & + d_5 \cdot \mathrm{IF} \cdot \mathrm{PUS} + d_6 \cdot \mathrm{IF} \cdot \mathrm{PUS} + \varepsilon_{BDC},\end{aligned} \tag{3.23}$$

and

$$\begin{aligned}\mathrm{BH} = {} & h_0 + h_1 \cdot I_{\mathrm{EFO}} + h_2 \cdot \mathrm{IF} + h_3 \cdot \mathrm{PUS} + h_4 \cdot I_{\mathrm{EFO}} \cdot \mathrm{PUS} \\ & + h_5 \cdot \mathrm{IF} \cdot \mathrm{PUS} + h_6 \cdot \mathrm{IF} \cdot \mathrm{PUS} + \varepsilon_{BH},\end{aligned} \tag{3.24}$$

where $\varepsilon_{\mathrm{BDC}}$ and $\varepsilon_{\mathrm{BH}}$ are normally-distributed error terms, assumed to be independent of each other. The mean value of each error term is assumed to be zero, with standard deviations σ_{BDC} and σ_{BH} for the two models. Model covariates are defined as

$$\begin{aligned} x_1 &= I_{\mathrm{EFO}} \\ x_2 &= \mathrm{IF} \\ x_3 &= \mathrm{PUS} \\ x_4 &= I_{\mathrm{EFO}} \cdot \mathrm{IF} \\ x_5 &= I_{\mathrm{EFO}} \cdot \mathrm{PUS} \\ x_6 &= \mathrm{IF} \cdot \mathrm{PUS}, \end{aligned} \tag{3.25}$$

so the model equation for BDC becomes

$$\mathrm{BDC} = d_0 + d_1 x_1 + d_2 x_2 + d_3 x_3 + d_4 x_4 + d_5 x_5 + d_6 x_6 + \varepsilon_{BDC}, \tag{3.26}$$

and similarly for BH. These models match the general form discussed in Section 1.6, and the techniques described there were used to generate the following results.

A 2^3 full-factorial design of experiment (DOE) with added centre point runs was used to generate the necessary data for fitting these models. Table 3.10 lists the factor levels used for I_{EFO}, IF, and PUS. Fig. 3.14 shows the factor combinations graphically. Four BDC measurements and eight BH measurements were taken for each of the DOE vertex points. For the centre point, five BDC measurements and 10 BH measurements were taken.

Eq. (3.26) was fitted to the measured bond geometries as in Section 3.2. For each of the three PUS levels, a contour plot was made showing curves of fixed BDC or fixed BH. These plots are shown in Fig. 3.15. For each plot, three intersection points were identified, corresponding to 61 µm BDC and 14 µm, 16 µm, or 18 µm BH. Confidence intervals for the optimal machine parameters for each of the 9 intersection points were also calculated, as in Section 3.2.

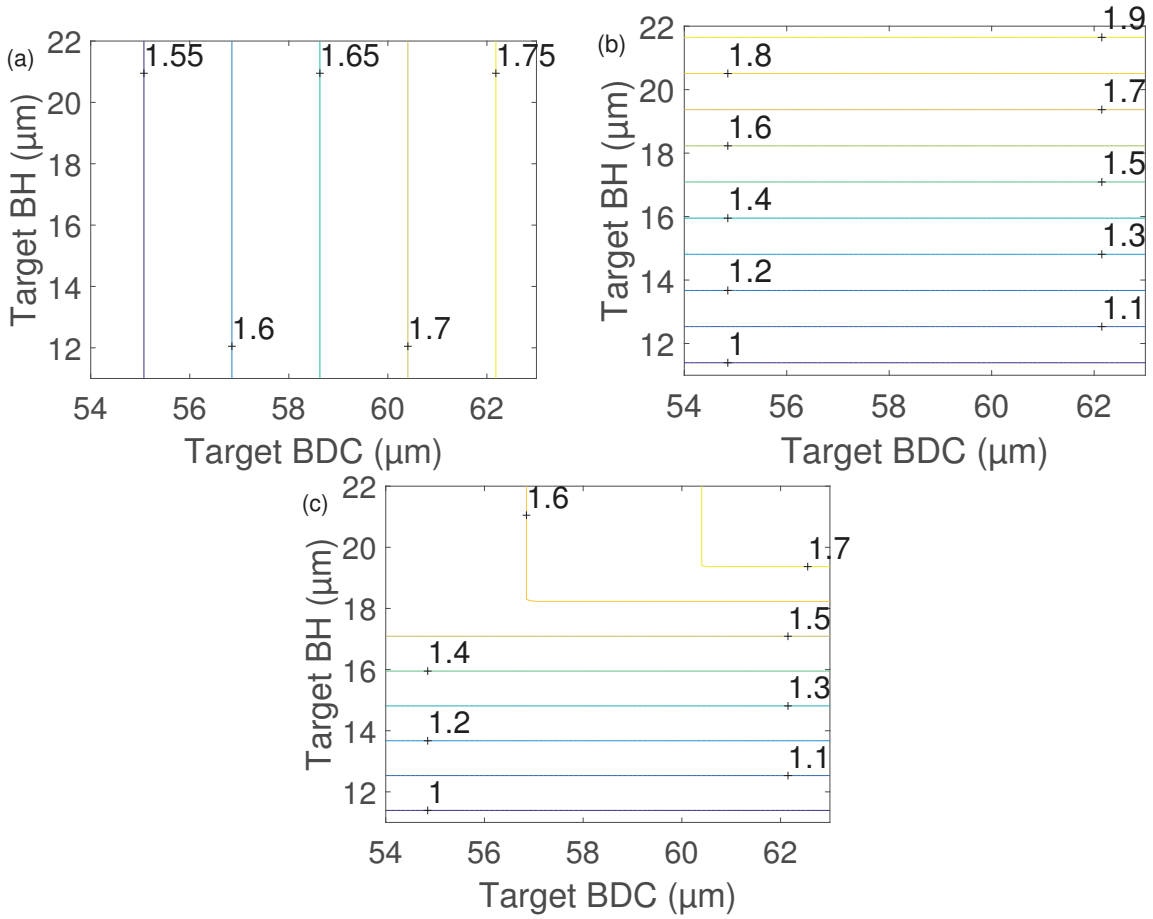

Fig. 3.13: . Contour plots showing estimates for maximum achievable C_{pk}, based on target values for BDC and BH. Specification limits are $\text{BDC}_{\text{target}} \cdot (1 \pm 0.05)$ for diameter and $\text{BH}_{\text{target}} \cdot (1 \pm 0.25)$ for height. (a) C_{pk} for BDC response. (b) C_{pk} for BH response. (c) Minimum of previous two C_{pk} values.

Table 3.10: Process factor levels for 2^3 factorial geometry experiment. The ball US, BF, and UT were held constant for this stage of the optimization.

Parameter	Low	Mid	High
IF (mN)	500	750	1000
I_{EFO}	55	50	65
PUS (%)	0	8	16

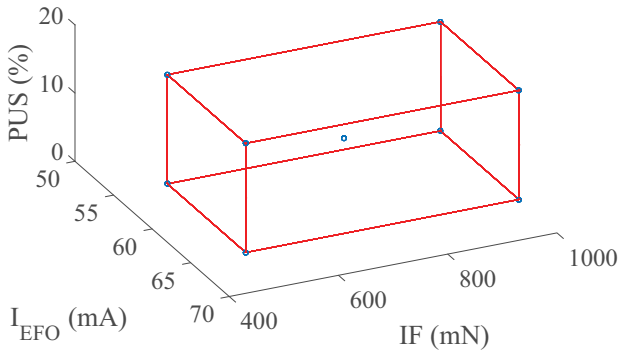

Fig. 3.14: Factor combinations for 2^3 factorial experiment, consisting of the 8 vertices of a rectangular prism and its centre. The BDC model was fitted using 37 measurements: 4 for each vertex and 5 for the centre. The BH model was fitted with twice as many points: 8 for each vertex and 10 for the centre.

3.3.2 $2^{(5-2)}$ Screening Experiment for PUS, US, BF, BH, and UT

Having obtained parameters to produce the required bond geometries, the next goal was to optimize the bonding step. Five factors, PUS, US, BF, BH, and UT, were investigated for their effects on ball shear strength and pad splash diameter. The factors PUS, US, BF, and UT are directly adjustable in the wire bonder's software. BH, however, is not a machine parameter and cannot be adjusted directly. Instead, after choosing desired values for PUS and BH, the machine settings of I_{EFO} and IF were adjusted to the appropriate intersection point identified in Fig. 3.15.

The effects of the five factors were tested using a 2^{5-2} fractional factorial DOE, with a centre point added. Fractional factorial experiments are used when testing three or more factors, to reduce the number of measurements required. These experimental designs are explained in more detail in [73]. Testing all combinations of 5 factors with two levels for each means testing 32 different runs of measurements, generally with multiple measurements per run. The 2^{5-2} and other fractional designs mitigate this problem by omitting many factor combinations. For instance, the 2^{5-2} design tests only one quarter of the possible combinations, for a total of 8 runs.

The disadvantage of fractional designs is that some of the terms in models such as Eq. (3.26) become "confounded", meaning that their coefficients cannot be estimated independently. Typically, the experimental runs are chosen so that no two linear terms or "main effects" are confounded with each other. Instead, the main effects are confounded with interaction terms, which often have much smaller effects on the responses. The 2^{5-2} experimental design used here confounds the main effects with two-factor interactions, so it is commonly used for screening experiments

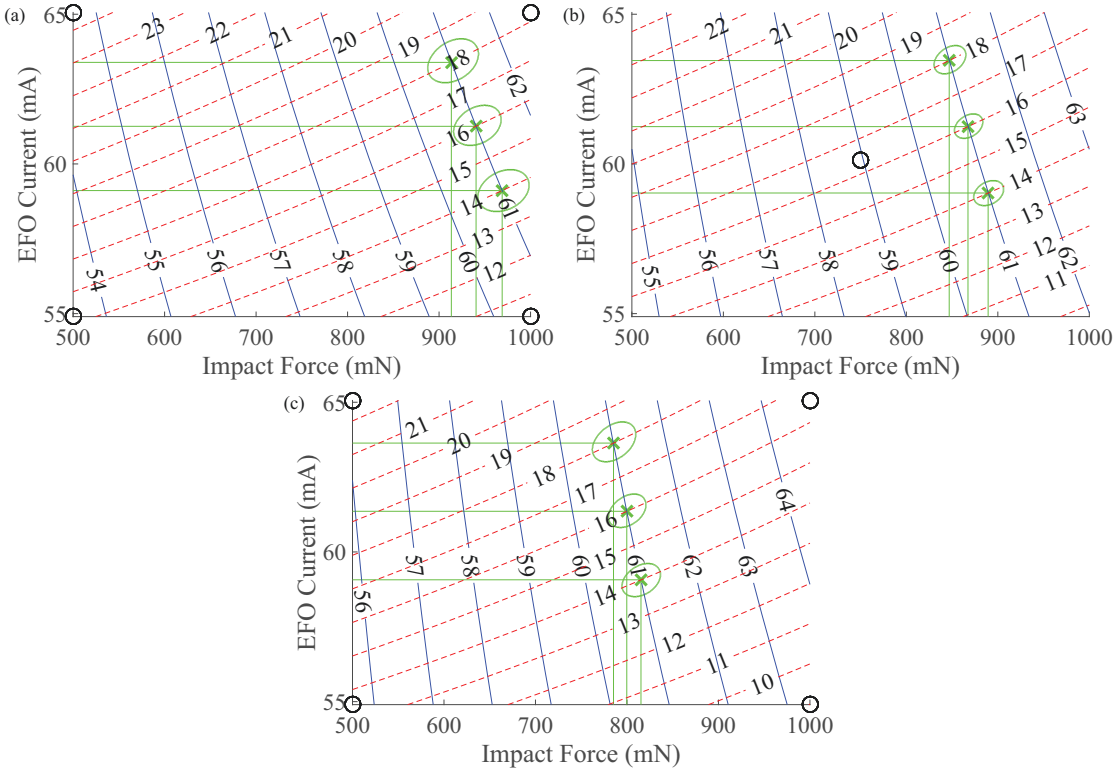

Fig. 3.15: Contour plots of bonded ball diameter and height. Nine black circles mark parameter combinations used in the experiment. BDC is constant along solid blue lines, BH along dashed red lines. Green X markings indicate intersections of target values, and the surrounding ellipses represent 95 % confidence regions. (a) 0 % Pre-US power. (b) 8 % Pre-US power. (c) 16 % Pre-US Power.

to determine which factors warrant further study. The details of which effects are confounded are given in Table 3.11.

3.3.3 Outcomes of Process Development

The final experiment leading to the optimized process parameters was the CCD experiment, already described in Section 3.2.2. The final bonding parameters given in Table 3.8 were chosen after combining the CCD results with those of Section 3.3.2.

Over the range of ball heights tested, the lowest value of 14 µm was found to give the best balance of high shear strength and low splash. Compared to a process with a large ball height,

Table 3.11: Model terms estimated from 2^{5-2} fractional factorial experiment.

Factor	Confounded With
PUS	US·BH, BF·UT
US	PUS·BH
BF	PUS·UT
BH	PUS·US
UT	PUS·BF
US·UT	BF·BH

reducing the height led to increased splash diameter, but also increased strength. Reducing US power could compensate for the increased splash, resulting in a net decrease of splash diameter for the same strength, or a net increase of strength for the same splash diameter. No significant evidence was found that adding pre-ultrasound to the process affected ball shear strength or pad splash.

3.4 Additional Production Processes: 61 µm and 75 µm, PCC and Bare Cu

To meet Objectives 3.(d) and 3.(e), investigating the reliability effects of Pd coating and ball bond diameter, a set of four bonding processes was required, using all combinations of two different ball sizes and two different wire types. Apart from these two factors, the four processes needed to be as similar as possible. This section describes the process optimization work done to develop these processes, and the resulting process responses. The work was also presented in [95].

Compared to Section 3.3, the geometry of 61 µm BDC and 14 µm was maintained as the smaller ball size, but a different capillary model was used, (part # SU-35110-515E-ZU36TS, Small Precision Tools, Inc., Petaluma, CA, USA) specifically designed for use with copper wire. For the larger bonds, a target BDC of 75 µm was chosen, judged to be near the maximum attainable size using the same capillary, with a target BH of 17 µm to maintain approximately the same ratio of BDC to BH. For shear strength, a target value of 130 MPa was chosen to maintain similarity with Section 3.3.

These four processes were developed using a simpler optimization procedure than in 3.3, based primarily on the Gomes method [92], but with some additional statistical analysis according to Section 1.6. The geometry optimization was performed four times, once for each geometry and

wire type combination, starting with the parameters in Table 3.12. The pad thickness for this step was 3000 nm. The geometry results, with confidence regions, are shown in Fig. 3.16.

In the second step, ultrasound was increased to optimize the ball shear strength. The shear strengths for the two PCC wire processes were optimized using simple one-parameter linear models, with the results shown in Fig. 3.17. The optimized US settings were identified from the models as those producing an estimated shear strength of 130 MPa. The shear strength optimization step was performed only twice: once for each geometry using PCC wire only. The dependence of shear strength on ultrasound is plotted in Fig. 3.17, with the target of 130 MPa and corresponding confidence interval indicated. After identifying the desired values for ultrasound, additional test bonds were made to verify the geometry and shear strength. Finally, bonds were made from bare Cu wire using the same ultrasound values determined for PCC wire. No significant difference in shear strength was observed between PCC and bare Cu, so additional optimization steps were deemed unnecessary. For each combination of wire material, bond pad thickness, and target bond diameter, 5 to 10 bonds were tested to determine the final process responses. The final optimized parameters and the process responses are given in Table 3.13.

Table 3.12: Starting ball bond parameters for development of four new bonding processes. The goal is to compare reliabilities between bare Cu and PCC wires and two different ball bond sizes, to meet objectives 3.(d) and 3.(e).

Target BDC (μm)	61	61	75	75
Target BH (μm)	14	14	17	17
Material	PCC	Bare Cu	PCC	Bare Cu
Impact Force (mN)	750, 1250	750, 1250	1500, 2500	1500, 2500
Bond Force (mN)	169	169	255	255
Bond Stress (MPa)	57.8	57.8	57.8	57.8
Pre-Ultrasonic Power (%)	0	0	0	0
Ultrasonic Power (%)	16	16	26	26
Ultrasonic Time (ms)	27.2	27.2	27.2	27.2
EFO Time (ms)	0.7	0.7	0.8	0.8
I_{EFO} (mA)	55, 65	50, 60	60, 70	60, 70
Heater Temperature (°C)	175	175	175	175
Bond Pad Thickness (nm)	3000	3000	3000	3000
Shielding Gas	N_2	N_2, 5 % H_2	N_2	N_2, 5 % H_2
Gas Flow (ℓ/min, fixed nozzle)	0.5	0.5	0.5	0.5
Gas Flow (ℓ/min, electrode nozzle)	0.35	0.35	0.35	0.35

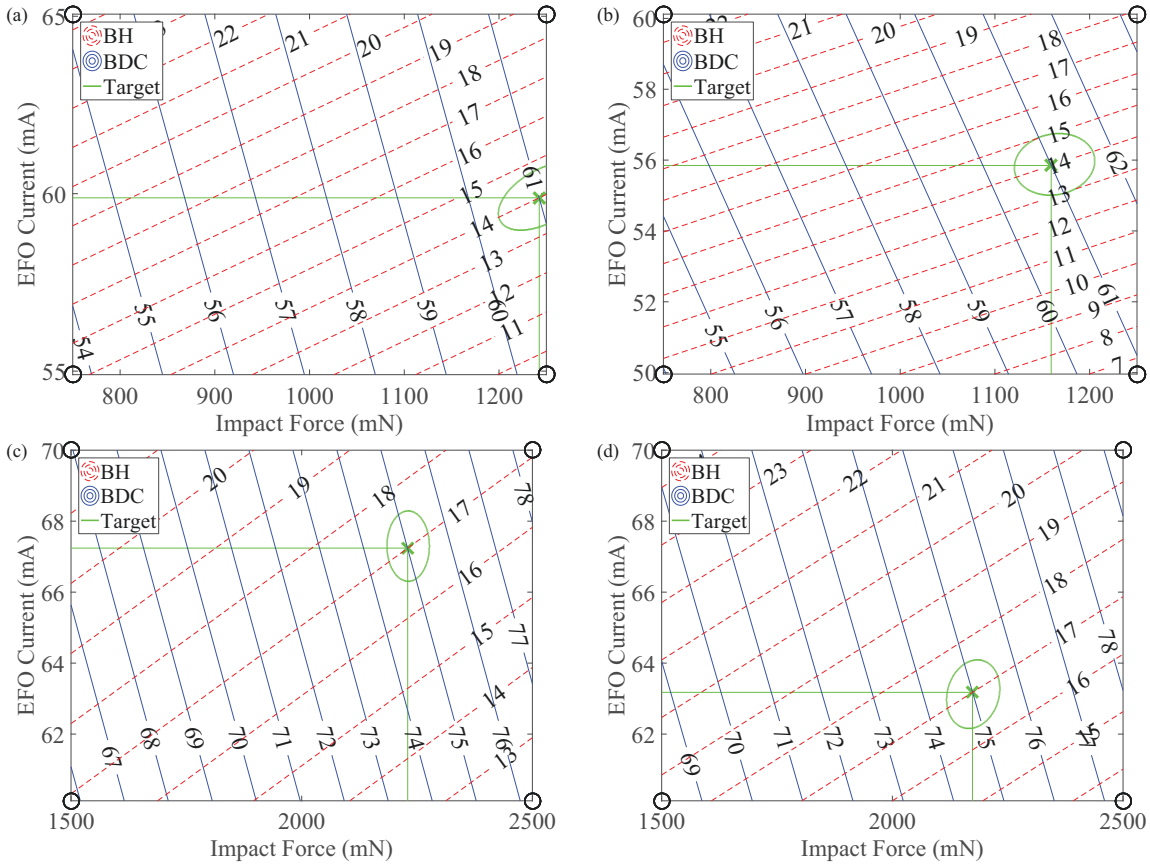

Fig. 3.16: Geometry results for PCC and bare Cu wire using parameters in Table 3.12, showing contours of fixed BDC and BH calculated from linear model. Shaded regions indicate 95 % confidence regions for the process parameters IF and I_{EFO}. (a) PCC wire, 61 µm target ball diameter. (b) Bare Cu wire, 61 µm target ball diameter. (c) PCC wire, 75 µm target ball diameter. (d) Bare Cu wire, 75 µm target ball diameter.

As seen in Fig. 3.16 and Table 3.13, bare Cu wire required a lower EFO current and lower impact force to achieve the same ball geometry. Two-way ANOVA was used to test for differences in shear strength between the four processes or between the two pad thicknesses. No statistically significant differences were found in this analysis: p-values were $p = 0.51$ between processes and $p = 0.44$ between thicknesses.

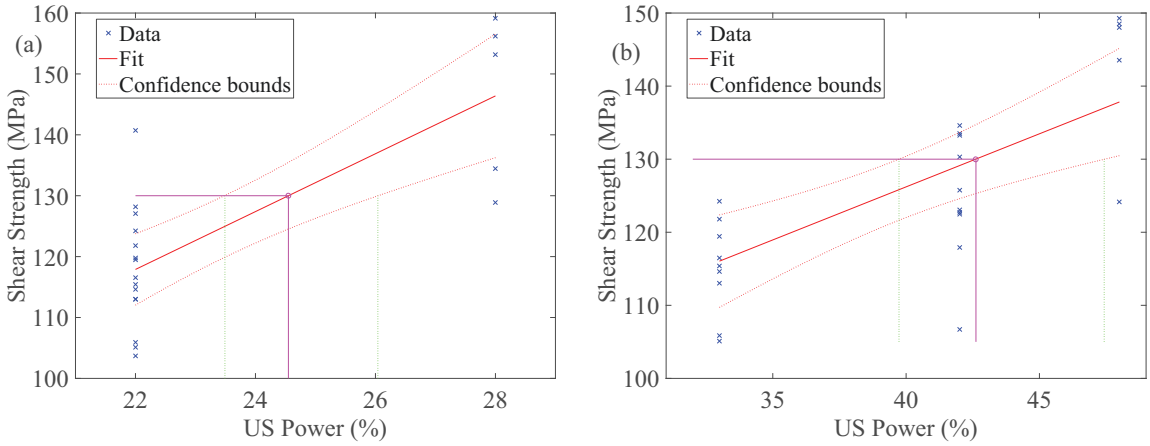

Fig. 3.17: Shear strength results for PCC wire on 3000 nm thick Al pads. (a) 61 µm target diameter. (b) 75 µm target diameter.

3.5 Conclusions from Process Development

Objective 2 has been met by extending the Gomes [92] optimization method in three ways:

1. Error analysis added at each stage of the optimization procedure
2. Optimization of second response variable, splash diameter, in Stage 2
3. Four additional process factors (including the quasi-factor, BH) studied: bond force, ultrasonic time, pre-ultrasonic power, and ball height

The error analysis does not require additional experimental time, and may reduce time costs by quickly identifying unstable processes or unsuitable factor ranges before continuing further in the procedure.

Minimizing the Al pad splash was necessary for this thesis, since the splash reduces the effective Al thickness in the reliability experiments of Chapter 4, where pad thickness is one of the factors investigated.

The influences of the four additional factors were not known, so their inclusion was necessary to improve confidence that the resulting splash was at the minimum level reasonably attainable. However, optimizing PUS and BH adds considerable complexity to the procedure and would not be worthwhile in most other circumstances.

Table 3.13: Final ball bond parameters and responses for four new bonding processes. SF and SS stand for shear force and shear strength, respectively. Responses are given as mean ± standard deviation. These processes are used in Chapter 4 to compare reliabilities between bare Cu and PCC wires and two different ball bond sizes, to meet objectives 3.(d) and 3.(e).

Target BDC (µm)	61	61	75	75
Target BH (µm)	14	14	17	17
Material	PCC	Bare Cu	PCC	Bare Cu
Impact Force (mN)	1242	1160	2229	2174
Ultrasonic Power (%)	24.57	24.57	42.01	42.01
I_{EFO} (mA)	59.84	55.73	67.25	63.14
BDC (µm)	61.9 ± 0.7	61.2 ± 0.7	76.3 ± 0.8	76.5 ± 0.8
BH (µm)	13.5 ± 1.0	13.8 ± 1.0	16.5 ± 0.6	16.5 ± 1.0
SF, 800 nm Pads (gf)	36.7 ± 2.0	35.6 ± 1.7	54.2 ± 3.4	56.3 ± 2.9
SS, 800 nm Pads (MPa)	125.6 ± 7.4	119.8 ± 5.5	124.0 ± 7.6	124.0 ± 7.5
SF, 3000 nm Pads (gf)	38.8 ± 1.9	37.6 ± 1.2	58 ± 4.3	57.5 ± 2.6
SS, 3000 nm Pads (MPa)	136.3 ± 6.6	125.4 ± 6.3	124.5 ± 10.9	122.1 ± 5.8

Six bonding processes for Cu wire have been developed that can be used for ball bonds on Al metallization. These processes are intended for Cu bond reliability studies. The differences between the processes and their uses in Chapter 4 are summarized in Table 3.14.

Table 3.14: Summary of six processes developed in this chapter, including shear strength as measured on 800 nm pads.

Process Name	Pilot	Process 1	Process 2	Process 3	Process 4	Process 5
Wire Material	PCC	PCC	PCC	Bare Cu	PCC	Bare Cu
Target BDC (µm)	58	61	61	61	75	75
Target BH (µm)	22	14	14	14	17	17
Shear Strength (MPa)	114	127	126	120	124	124
Used in Sections	4.2	4.4.1, 4.4.2	4.4.1 to 4.4.4			

Chapter 4

High-Temperature Storage Testing of Cu Wire Bonds

This Chapter describes testing of copper wire bonds at high temperatures, with analysis of the results based on accelerated failure time models as in Section 1.7. It consists of 11 sections. Section 4.1 explains the materials, sample preparation procedures, and testing procedures used. Section 4.2 describes a pilot experiment, with results used to guide planning of the subsequent experiments. Section 4.3 describes the five factors investigated for their effects on reliability. Section 4.4 describes and presents results from the primary high-temperature experiments. Section 4.5 discusses experiments at using the humidity system of Section 2.1. Section 4.6 applies accelerated failure time models to the results of Section 4.4 to calculate activation energies. Section 4.7 presents analysis of the quality of the fits in Section 4.6. Section 4.8 presents a novel technique for measuring the resistance only of the central span of a bonded wire, and uses this method to demonstrate that the wire spans contribute only a minor portions of the total changes in resistance observed. Section 4.9 presents cross-section images of aged samples to illustrate failure mechanisms. Section 4.10 discusses the effects of the five factors studied on bond reliability. Finally, Section 4.11 uses the fitted models of Section 4.6 to estimate wire bond failure probabilities as functions of temperature time, and similarly estimates the maximum allowable temperature for given requirements of lifetime and failure probability.

4.1 Experimental Setup: ON Semiconductor Dies on Ceramic Substrates

To investigate Cu wire bond HTS reliability, and also demonstrate the statistical analysis techniques of Section 1.7, Cu wire bonds were tested under a variety of HTS conditions, as explained in the following sections. The flow chart in Fig. 4.1 summarizes the sample preparation procedure. Fig. 4.2 shows optical images of completed samples at three levels of magnification.

4.1.1 Materials

As in Chapter 3, the wires used were PCC or bare Cu, 25 µm in diameter, from the same supplier. The test dies used were provided by ON Semiconductor, die attached to Au-metallized ceramic substrates using Ablestik 2000B Ag-filled epoxy, produced by Loctite (Düsseldorf, Germany), as shown in Fig. 4.2. The test dies had Al bond pads, 800 nm or 3000 nm thick. The substrate metallization consists of three layers. From bottom to top, these are Ni, Ni-Co alloy, and Au, with thicknesses approximately 1.1 µm, 2.9 µm, and 1.6 µm, respectively, with a cross-section shown in Fig. 4.3.

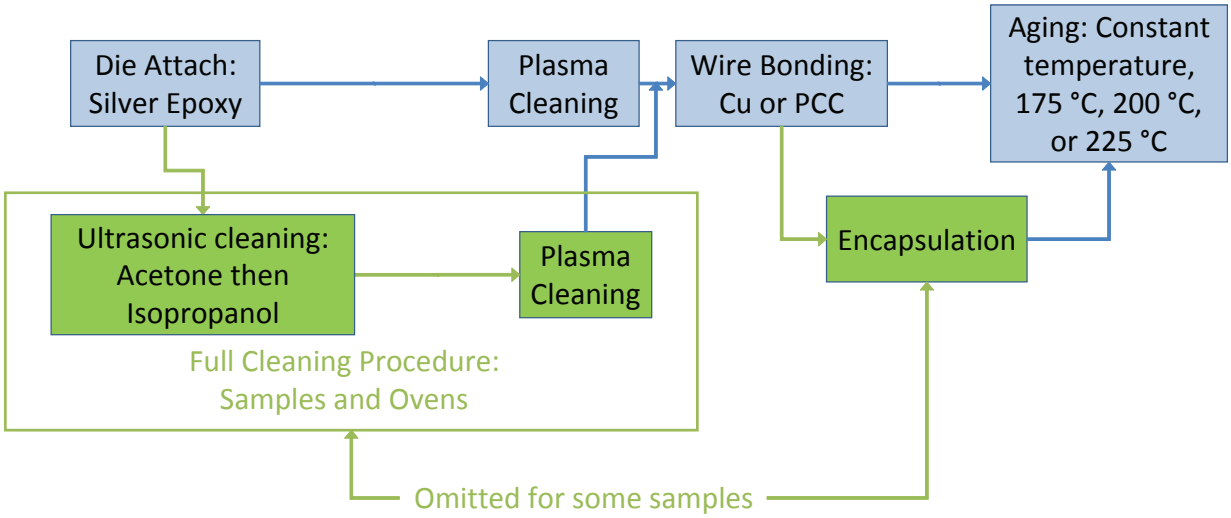

Fig. 4.1: Flow chart of sample preparation procedure.

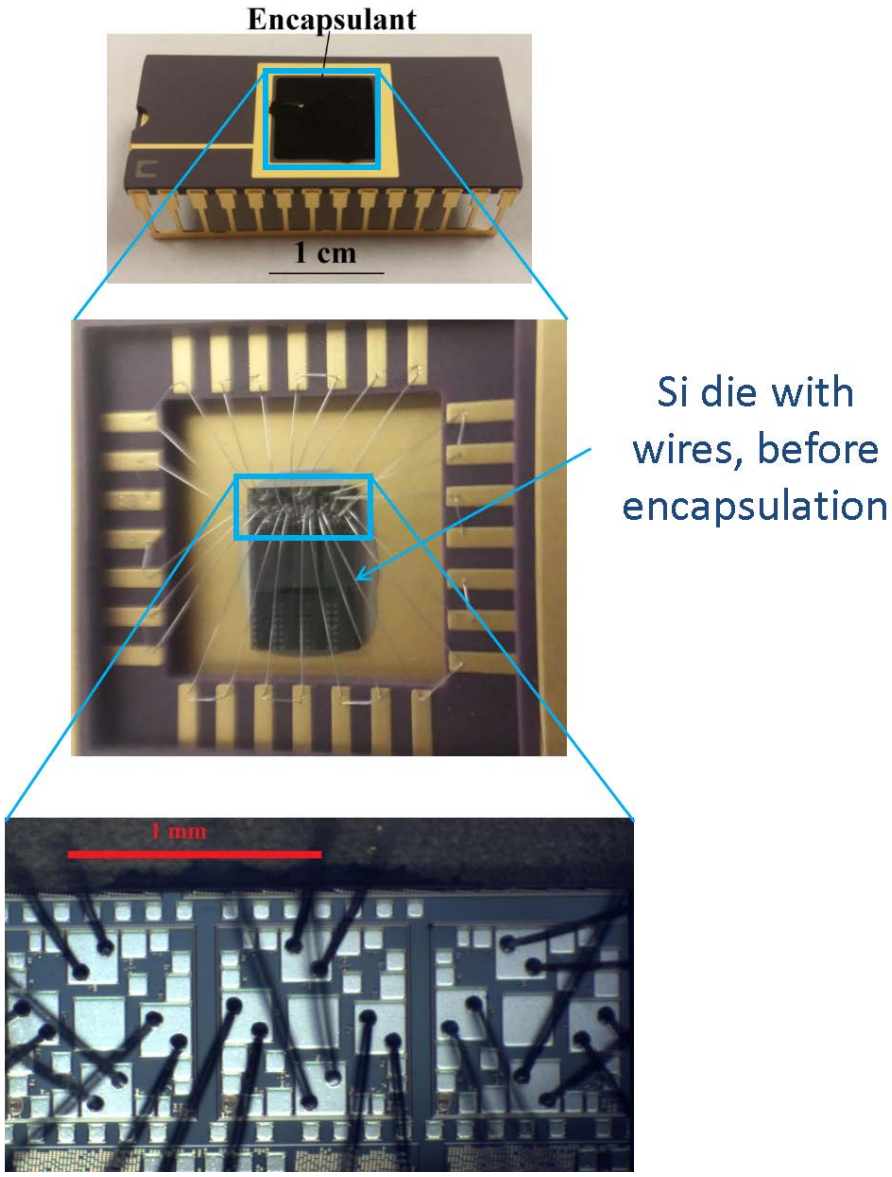

Fig. 4.2: Optical images of completed samples. Top: Ceramic substrate with epoxy encapsulant covering the bonded wires. Middle: Bonding area of substrate without encapsulation, including Si die and PCC wires. Bottom: Bonded area of Si die, showing two ball bonds on each of 12 large pads.

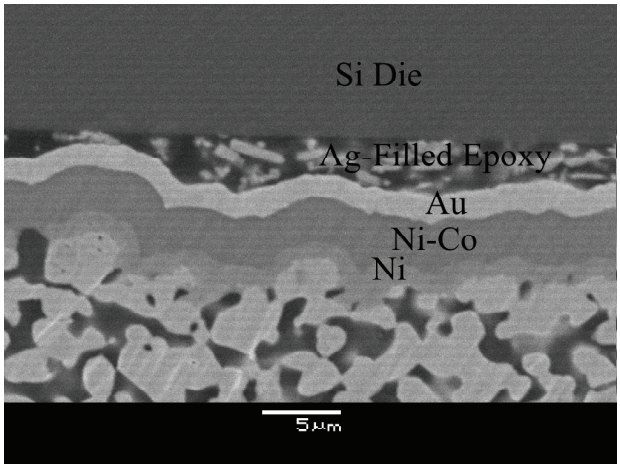

Fig. 4.3: Cross-section through Si die and ceramic substrate, showing substrate metallization layers.

4.1.2 Wire Layout

The wires were typically laid out as in Fig. 4.4, with some exceptions for particular experiments as mentioned in the following sections. This standard layout, with 24 test wires and 14 auxiliary wires, yields 12 four-wire resistance measurements of wire pairs. The measured resistance is the sum of resistance contributions from two Cu ball to Al pad interfaces, two Cu wire spans, two Cu wedge to Au leadfinger interfaces, the Al pad metallization, and the Au leadfinger metallization.

These samples were tested in the mini-ovens, with the graphite interface pads of Section 2.2.3, in a series of many high-temperature aging experiments. In total, 1004 wire pairs on 84 substrates were tested, with temperatures of 175 °C, 200 °C, and 225 °C. The wires were bonded using the processes developed in Chapter 3.

4.1.3 Cleaning Procedure

Cleanliness of the bonding area and the environment are known to be important for good wire bond reliability [3]. To ensure good cleanliness, a thorough cleaning procedure was performed on many of the substrates after die attach and before wire bonding. First, they were ultrasonically cleaned in a bath of acetone, then in a second bath of isopropanol for approximately 1 min each, and finally the isopropanol was dried using a jet of pressurized nitrogen gas. Next, the substrates were plasma cleaned for 10 min using an Ar-H plasma mixture. Finally, immediately before

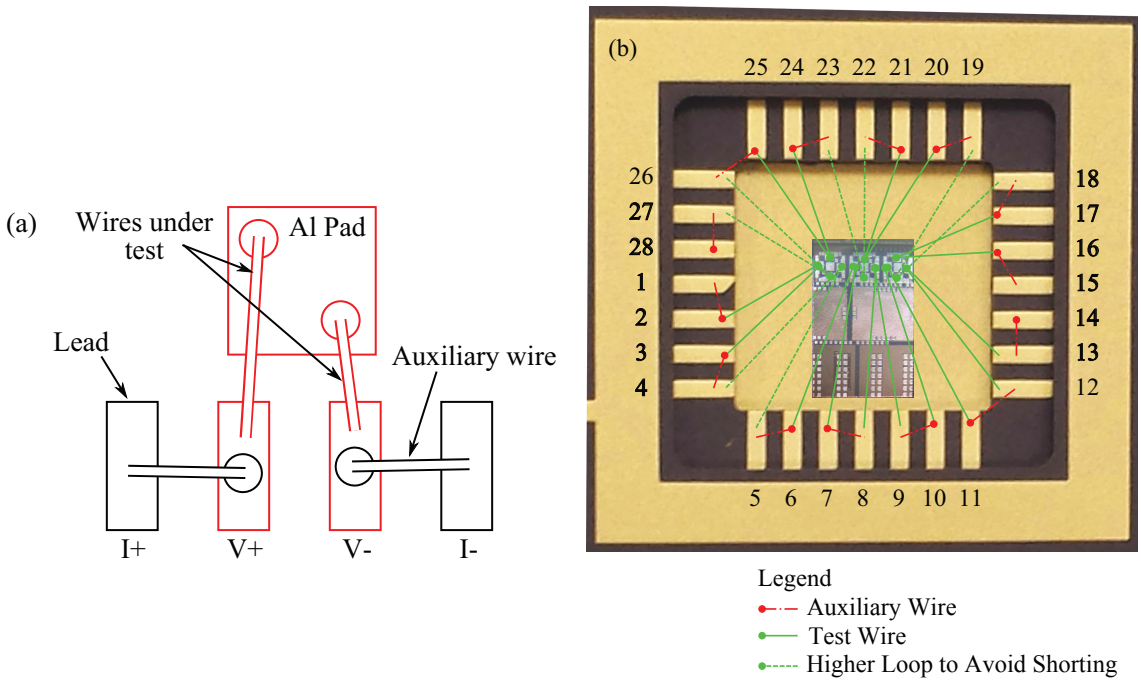

Fig. 4.4: (a) Schematic of a single wire bond pair with auxiliary wires, enabling one four-wire resistance signal. Components shown in red contribute to the total resistance measured. (b) Schematic of standard wire layout, consisting of 24 test wires and 14 auxiliary wires. Allows 12 four-wire resistance measurements of wire pairs. Own work, reproduced from [96].

bonding each substrate, it was rinsed with deionized water, and dried in air by placing it on the heater plate of the wire bonder.

The same process, omitting the deionized water rinse, was applied to the mini-oven heater blocks, graphite thermal interface pads, and Pt100 temperature sensor substrates. This procedure is referred to as the full cleaning process in the remaining sections of the thesis; other substrates received plasma cleaning only, referred to as limited cleaning, with no ultrasonic cleaning or deionized water rinse, and no prior cleaning of the mini-ovens. Compared to plasma cleaning only, the full cleaning procedure resulted in major improvements in bond reliability, based on the observed times before electrical failures. For example, with unencapsulated PCC bonds on 800 nm thick Al pads, the median lifetimes were 458 h and 934 h, for plasma cleaning and full cleaning, respectively, where failure is defined as in Subsection 4.1.4.

4.1.4 Monitor Resistance to Determine Failure Times

During aging, the bond pair resistances were monitored and recorded continually. The typical time interval between consecutive resistance measurements of a single bond pair was 37 min; the interval was shorter if fewer than ten samples were being tested at once in a particular oven rack. These values were then used as indicators of bond degradation. For comparing resistance values of different wires, the values were normalized to minimize the effects of extraneous variables. For example, the wires varied in length, with longer wires having a larger initial resistance. This longer wire span, however, did not contribute much to degradation over time (see Section 4.8), so the initial resistances were subtracted, and only the changes in resistance were compared. Mathematically, the total measured resistance is

$$R(t) = 2R_{\mathrm{Cu-Al}}(t) + 2R_{\mathrm{Cu}} + 2R_{\mathrm{Cu-Au}} + 2R_{\mathrm{Au}} + R_{\mathrm{Al}}, \tag{4.1}$$

with the contribution of interest, $R_{\mathrm{Cu-Al}}(t)$, coming from the Cu-Al interface. The four additional contributions are: R_{Cu}, the wire span resistance, $R_{\mathrm{Cu-Au}}$, the Cu-Al interface at the wedge bond, R_{Au}, the Au metallization on the substrate, and R_{Al}, the Al pad metallization. These extraneous contributions are assumed constant over time. So, to isolate the contribution of interest, the initial resistance,

$$R(0) = 2R_{\mathrm{Cu-Al}}(0) + 2R_{\mathrm{Cu}} + 2R_{\mathrm{Cu-Au}} + 2R_{\mathrm{Au}} + R_{\mathrm{Al}}, \tag{4.2}$$

was subtracted to obtain

$$\Delta R(t) = R(t) - R(0) = 2[R_{\mathrm{Cu-Al}}(t) - R_{\mathrm{Cu-Al}}(0)]. \tag{4.3}$$

As illustrated in Fig. 4.5, the graphs of resistance versus time were examined for each substrate to identify the time just after heating when all readings reached a steady value. This time is defined to be $t = 0$ for that substrate. The mean of the next five readings for each wire pair was taken to be the initial heated resistance, $R(0)$, for that pair. Next, all such values were grouped according to the testing temperature, calculating three mean initial values corresponding to the temperatures of 175 °C, 200 °C, and 225 °C. These values were 0.466 Ω, 0.491 Ω, and 0.525 Ω, respectively, with standard deviations of 0.081 Ω, 0.089 Ω, and 0.096 Ω, respectively.

Next, the resistances were normalized to account for different aging temperatures, since there is a reversible increase in resistance as temperature increases, independent of any degradation also resulting from high temperature. There are two possible options for normalization. The resistance change for wire pair i, $\Delta R_i(t)$ could be divided by: (a) the initial value for the same wire pair, $R_i(0)$, or (b) a reference value, such as the mean initial value for all wire pairs at the same temperature, $R_{\mathrm{mean}}(0)$. In choosing between these options, an important requirement was that if two wire pairs degrade identically at the Cu-Al interface, the normalized resistance changes should also be identical, regardless of constant contributions from, e.g., the Al pad metallization.

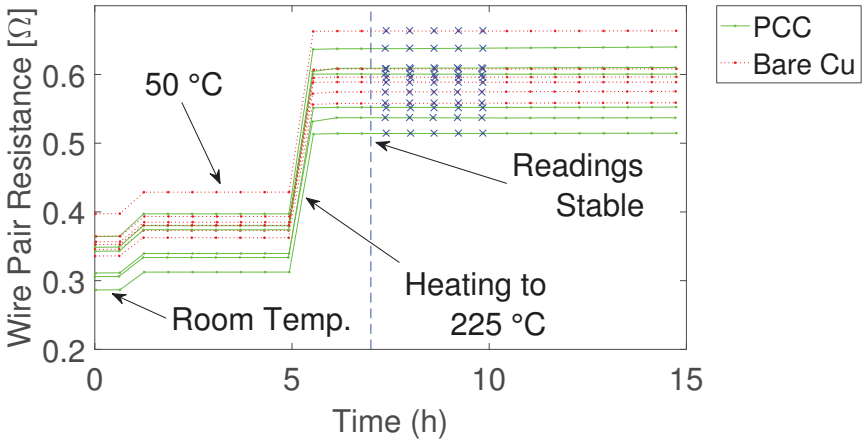

Fig. 4.5: Typical wire pair resistance behaviour at beginning of aging test, for a single substrate. Samples were first monitored at room temperature to verify proper equipment functioning, then heated to 50 °C for 4 h before heating to aging temperature. After heating, five readings for each wire pair, marked with "x", were used to calculate initial resistances for normalization. This substrate had six PCC and six bare Cu wire pairs on 800 nm thick pads, tested at 225 °C.

Only option (b) meets this requirement, so the second option was chosen, with the normalized resistance change for wire i defined as

$$\Delta r_i(t) = \frac{R_i(t) - R_i(0)}{R_{\text{mean}}(0)}, \tag{4.4}$$

where $R_{\text{mean}}(0)$ refers to the mean initial resistance for all wires tested at the same temperature as wire i. From the normalized resistance signals during aging, failure times for each wire bond pair can be identified. Failure was defined as a 10 % increase in resistance compared to the initial mean value. A 10 % resistance increase was chosen as the failure condition because up to this level, the resistance increase is generally smooth and consistent between bonds. Above a 10 % change, many bonds begin to degrade rapidly toward open circuit failures.

4.1.5 Test at 3 Temperatures to Enable Arrhenius Fitting

With the goal of fitting Arrhenius models as described in Section 1.28, samples were tested at three temperatures: 175 °C, 200 °C, and 225 °C. Although two temperatures would be sufficient to obtain an estimate of the activation energy, a third temperature is needed to assess whether the data truly follows the Arrhenius behaviour. These particular temperatures were chosen for consistency with other publications commonly using 175 °C and 200 °C [25, 28, 34, 52, 53, 55, 60–62]. The

highest temperature, 225 °C, is near the upper limit of the mini-oven heating capability. A test temperature of 150 °C was deemed too low, since earlier publications show little degradation of Cu bonds at 150 °C. For example, [97] tested epoxy-encapsulated bonds for up to 25 days, with no cracks observed at 150 °C or 175 °C, but cracks were observed after 9 days at 200 °C. Ref. [40] tested PCC wire at 150 °C for 2000 h with 9 different encapsulant variations. They observed no bond failures in these conditions, with failure defined as a 20 % increase in electrical resistance of 6 wire connected in series.

4.2 Pilot Experiment

Reliability testing began with a pilot experiment for preliminary data, used to guide the planning later experiments. The worst-case factors of maximum temperature, low-purity encapsulant, and limited sample cleaning were used for this experiment, as explained in more detail later in this section. If failure times were very long in this experiment, then the plan of testing some samples at 175 °C with higher-purity encapsulants and more cleaning steps would not be feasible.

These tests used 25 µm PCC wire, with the bonding process developed in Section 3.1. The dies used for this test had only 10 large bonding pads, so instead of the standard layout of 12 wire pairs for testing, ten wire pairs were bonded to Al pads and two wires directly linked Au terminals. The Al pad thickness for these samples was 800 nm. Wires were bonded on three substrates: two were aged at 225 °C, with one encapsulated and one not. The third was reserved for cross-sectioning without aging. The encapsulant used was EPO-TEK 353ND, which has a high chloride ion content of 329 ppm and is not a typical encapsulant for copper wire bonds. The aging results are therefore not representative of bonds used in mass production.

Resistance data obtained during aging is shown in Fig. 4.6. Four of the encapsulated wire pairs failed immediately upon heating; the remainder failed within 84 h of heating, showing the importance of proper encapsulant selection for reliability. For unencapsulated wire pairs, the first failure occurred 424 h after heating, and five of the ten pairs had failed after 682 h. The test was stopped after 741 h, at which point seven of the ten bonds had failed.

After testing, the two aged samples and one without aging were cross-sectioned for analysis of the failure mechanisms, producing the SEM images shown in Fig. 4.7. For the encapsulated sample, a severe crack is visible under the Cu ball, spanning the entire width of the bond. In both aged samples, voids are visible along the upper edges of the ball, similar to those reported in [66]. For the unencapsulated sample, a crack is seen in the Si die, but was not seen in earlier optical images of the same sample, and is due to excessive stress during cross-sectioning. Cross-sectioning techniques were refined after preparing these samples to avoid such damage for later samples.

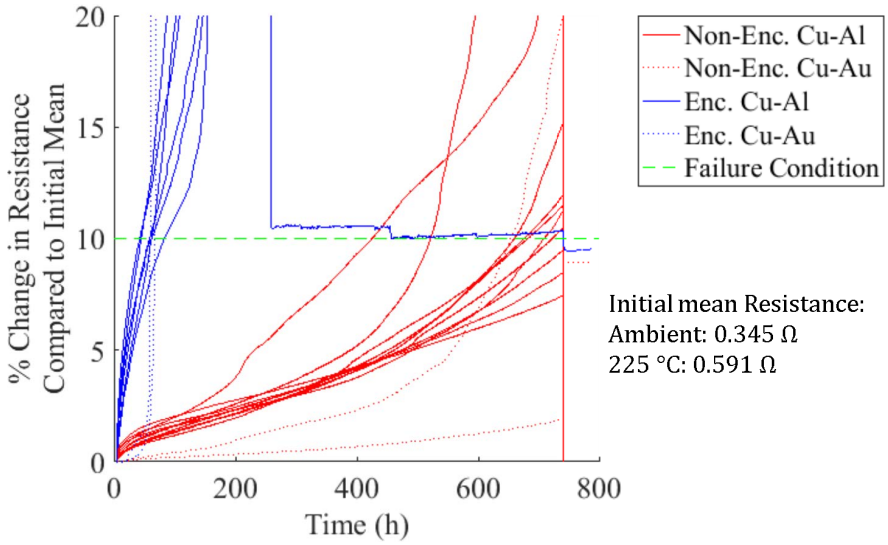

Fig. 4.6: Resistance changes of 16 PCC wire pair samples on 800 nm thick Al pads at 225 °C with low-purity encapsulant, from pilot experiment. Solid lines indicate standard wire pair samples. Dotted lines indicated single wires bonded directly between leadfingers, meaning there is no Cu-Al interface.

This experiment confirmed that, within the temperature limits of the ovens used, Cu-Al bonds can be induced to fail on a practical timescale of less than 1000 h. Also, the resistances have been demonstrated to increase monotonically until failure, with measurement noise much smaller than the signals of interest, so that bond failure times can be unambiguously defined by the time required to reach a particular change in resistance. These two conditions of achievable and well-defined failure times are necessary for analysis using accelerated failure time models as discussed in Sections 1.7, and 4.6, so it was important to verify that the conditions were met before beginning a large-scale experiment.

4.3 Factors Under Test

Five factors were tested for possible effects on ball bond aging behaviour. This section lists each of the five factors, including an explanation as to its possible effect on bond reliability.

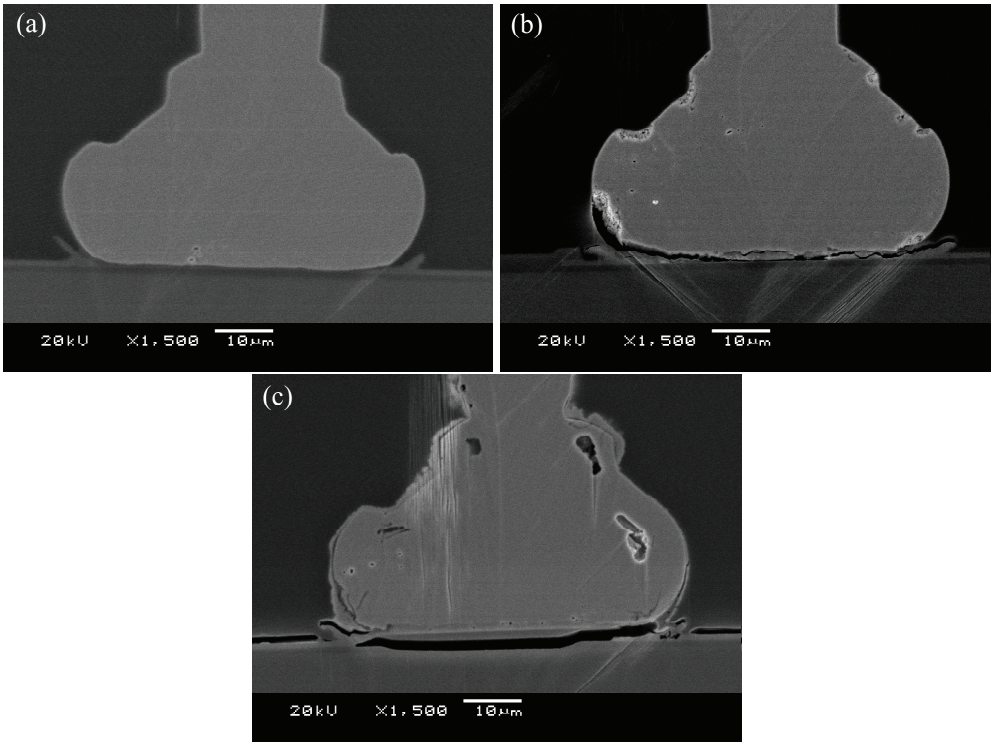

Fig. 4.7: Cross-sections of samples from pilot experiment. (a) Without aging. (b) Aged 253 h at 225 °C with EPO-Tek 353ND encapsulation. (c) Aged 736 h at 225 °C without encapsulation.

1. Cleaning procedure

   Bond pad cleanliness is well-known to affect bond reliability [3]. In these experiments, cleanliness is especially important; the small size of the mini-ovens means that any volatile contaminants present on the sample or on the oven walls are not diluted into the large volume of a conventional oven, and there is little convection available to carry contaminants outside of the oven. Section 4.1.3 describes the cleaning procedure used for the majority of samples, with some left uncleaned for comparison.

2. Choice of encapsulant

   Encapsulants also have strong effects on bond reliability [3]. In particular, a low pH, or high concentrations of Cl or S can severely reduce Cu bond reliability. In this work, three different encapsulants were tested extensively: two epoxies and one silicone. Some samples were also tested without encapsulation for comparison.

3. Bond pad thickness

   As discussed in Section 1.4.3, the IMC layer gradually thickens at high temperature, consuming the Al bonding pad. As the supply of Al is depleted, IMC growth shifts toward Cu-rich IMCs, Cu_9Al_4 and possibly Cu_3Al, which are more vulnerable to corrosion and crack formation [63]. A larger pad thickness means that more Al is available, which may increase the time before the formation of Cu-rich IMCs, thus prolonging bond lifetimes.These experiments used two bond pad thicknesses: 800 nm because it is a common thickness used in mass production, and 3000 nm because it was the largest thickness available on the dies provided by ON Semiconductor, thus maximizing contrast with the thinner 800 nm pads.

4. Ball diameter

   As described in Section 1.4.3, bond failure can be caused by crack formation at the bond interface. Such cracks begin at the outer edge of the bonded interface and progress inward over time. A larger bond interface may increase the time required for the cracks to reach the centre, meaning a longer time to failure. The nominal bonded ball diameters used were 61 µm and 75 µm, using the processes developed in Section 3.4.

5. Pd-coated or bare Cu wire

   During FAB formation, the Pd coating on the wire tail is incorporated into the molten Cu. Some studies indicate that the resulting Pd-doping of the Cu at the bond interface reduces the rate of IMC formation, which may improve reliability. Conversely, an electrochemical reaction can occur at the wire surface between the Pd coating and bulk Cu, producing voids in the Cu that may degrade bond reliability [66]. Both PCC and bare Cu were used in these experiments.

Figs. 4.8 and 4.9 indicate the combinations of these five factors that were tested. Not all possible combinations were included due to limited resources, including the number of test dies and ovens available, so the tests focused on those combinations that would efficiently achieve the objectives stated in Section 1.3. For instance, it soon became clear that samples with limited cleaning or with Epoxy A performed poorly, so any further results for such samples would be of limited value.

	800 nm Al thickness		3000 nm Al thickness	
	Epoxy A	Unenc.	Epoxy A	Unenc.
175 °C	36		36	
200 °C	36		36	
225 °C	36	36	36	36

Fig. 4.8: Table of samples tested with limited cleaning procedure. Shaded cells indicate combinations of temperature, encapsulation, and bond pad thickness that were tested. Numbers indicate how many wire bond pairs were tested for that combination.

		800 nm Al thickness							
		PCC				Cu			
		Epoxy A	Epoxy B	Unenc.	Silicone	Epoxy A	Epoxy B	Unenc.	Silicone
61 µm bond diameter	175 °C		9	36	9		9		9
	200 °C		9	36	9		9		9
	225 °C		9	45	9		9	9	9

		PCC				Cu			
		Epoxy A	Epoxy B	Unenc.	Silicone	Epoxy A	Epoxy B	Unenc.	Silicone
75 µm bond diameter	175 °C		9		9		9		9
	200 °C		9		9		9		9
	225 °C		9	9	9		9	9	9

		3000 nm Al thickness							
		PCC				Cu			
		Epoxy A	Epoxy B	Unenc.	Silicone	Epoxy A	Epoxy B	Unenc.	Silicone
61 µm bond diameter	175 °C	9	9	36		9	9		
	200 °C	9	9	36		9	9		
	225 °C	9	8	45		9	9	9	

		PCC				Cu			
		Epoxy A	Epoxy B	Unenc.	Silicone	Epoxy A	Epoxy B	Unenc.	Silicone
75 µm bond diameter	175 °C	9	9			9	9		
	200 °C	9	9			9	9		
	225 °C	9	8	9		9	7	9	

Fig. 4.9: Table of samples tested with full cleaning procedure. Shaded cells indicate combinations of temperature, encapsulation, wire type, bond pad thickness, and ball bond diameter that were tested. Numbers indicate how many wire bond pairs were tested for that combination. Four wire pairs on one substrate were not bonded properly and were therefore excluded from all of the analysis; these account for the three entries that are not multiples of nine.

4.4 Experiment Descriptions and Preliminary Results

4.4.1 Unencapsulated Trials

Limited Cleaning

After completing the pilot experiment, two trials were performed in parallel: one using unencapsulated samples, described in this section, and one using Epoxy A, described in Section 4.4.2. Samples were first tested with the limited cleaning procedure: plasma cleaning only, as discussed in Section 4.1.3. These trials used PCC wire only, and all samples were tested at 225 °C. Bond process 1, described in Section 3.3, was used to produce these bonds.

Fig. 4.10 shows resistance data for all samples in this experiment. Lifetimes were very inconsistent, with the first failure after 20 h and many failures in the first 50 h for samples on 800 nm pads, but others survived 780 h without failure. Lifetimes on 3000 nm pads were longer but still inconsistent, with the first failure at 571 h, but other samples surviving 1000 h.

Comparisons between groups, such as the two groups of wires in Fig. 4.10, require statistical analysis of the variation within each group. Fig. 4.11 is a plot based on such an analysis for the resistance changes of unencapsulated PCC samples with limited cleaning. Such plots also summarize the resistance data conveniently, so that more sample groups can be visually compared in a single plot. Additional plots similar to Fig. 4.10, showing resistance changes for every bond

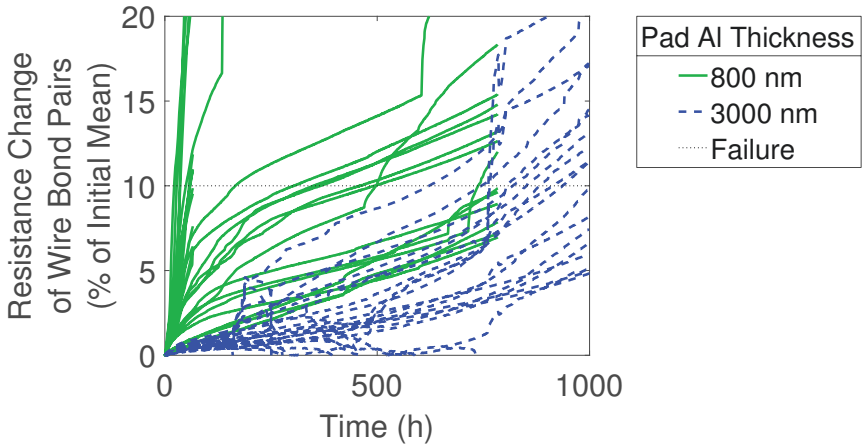

Fig. 4.10: Normalized resistance changes over time for unencapsulated PCC bond pairs at 225 °C with limited cleaning. Two bond pad thicknesses, with three different ovens used for each thickness. Without cleaning, bonds age at drastically different rates, with some bonds failing very rapidly.

pair, are shown in Appendix A.1. It shows the median resistance changes over time with 95 % confidence bands, based a Kaplan-Meier estimate, explained in the following paragraphs and calculated using the file KMPlot.m in Appendix C.4. From this plot, it is clear that there is a statistically significant difference in lifetimes between the group bonded on 800 nm pads and the group bonded on 3000 nm pads. However, this difference may be due to confounding factors and not a true effect of pad thickness; in particular, the lack of cleaning greatly affects the repeatability of the results, as discussed in the next section.

The set of resistances for all wire pairs in a single group at a single temperature can be summarized using the Kaplan-Meier estimate for the survival probability, as defined in Section 1.7.5 and in [75]. Similar to Eq. (1.37), but using the times t_i instead of residuals z_i, the Kaplan-Meier estimate gives the probability of failure at or before time t as

$$\hat{F}(t) = 1 - \prod_{i:t_i<t} \frac{n_i - f_i}{n_i}. \tag{4.5}$$

As in Section 1.7.5, n_i is the number of samples that were being observed at time t_i, meaning the number that had not yet failed or been censored, and f_i is the number of samples that failed at time t_i.

To summarize resistance changes using the Kaplan-Meier estimate, the first step is to choose a fixed level of resistance increase, e.g. 1 %, and identify the time at which each wire pair exceeded this level. These times are the "failure" times t_i used in Eq. (4.5). If a wire pair did not reach the resistance change threshold, it is considered censored, with the censoring time taken to be the time that testing stopped for that pair. Then the estimated median time to 1 % resistance increase is the

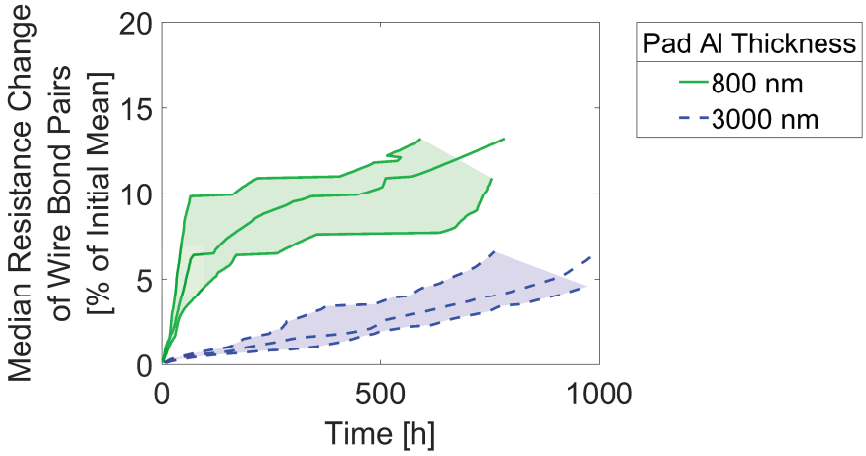

Fig. 4.11: Summary plot of unencapsulated aging behaviour at 225 °C with limited cleaning.

earliest time for which $\hat{F}(t) \geq 0.5$, i.e. the probability of failure is at least 50 %. This procedure is repeated for resistance change levels of 0.1 % up to 20 %, with these change levels plotted against the resulting median times to indicate the median degradation behaviour for a particular group of wires. Confidence intervals for the medians are calculated using Greenwood's formula [75], which gives the variance of $\hat{F}(t)$ as

$$\mathrm{var}(\hat{F}(t)) = \hat{F}(t)^2 \sum_{i:t_i<t} \frac{f_i}{n_i(n_i - f_i)}. \tag{4.6}$$

So, assuming an approximately normal distribution for $\hat{F}$, 95 % confidence bounds for $\hat{F}(t)$ are

$$\hat{F}(t) \pm 1.96 \quad \overline{\mathrm{var}(\hat{F}(t))}. \tag{4.7}$$

Upper and lower confidence bounds for the median failure time are taken to be the earliest times for which the upper and lower confidence bounds for $\hat{F}(t)$ reach 0.5 or lower, similar to the procedure for estimating the median.

Full Cleaning

The wide variation in lifetimes seen in Section 4.4.1 is highly undesirable, both in real production and for fitting statistical models, since it greatly reduces the precision of any statistical estimates made from the lifetime data. As illustrated in Fig. 4.12, the lifetimes of bonds on the same substrate appear highly correlated. Since the preparation procedures were the same for all of these samples, pre-existing or accidental contamination of the samples was suspected to be responsible for the inconsistencies, and the cleaning process described in Section 4.1.3 was developed to remedy the problem. The set of trial factors was also expanded for the 225 °C tests, with two ball bond diameters and bare Cu wire tested as well as PCC in the 225 °C tests. Bond Process 1 was used for 36 PCC wire pairs for each of the three temperatures, and Processes 2 to 5 to produce 9 wire pairs for each combination of bond diameter and wire type tested at 225 °C.

Figs. A.1 and A.4 show the resulting resistance change data. In particular, the solid green curves of Fig. A.4 (a) and the solid blue curves of Fig. A.4 (b) show results for PCC wire, approximately equivalent to Fig. 4.10 except for the added cleaning steps.

The median lifetimes for PCC wire, seen in Fig. 4.13, are greatly improved compared to the results without cleaning, and the narrower confidence bands indicate that consistency between samples is also improved. Bare Cu, however, failed significantly faster than PCC in these conditions, likely due to oxidation of the unprotected Cu.

The bond pad thickness had a minor effect on the bond degradation behaviour, with similar times to 10 % resistance change, but slower initial resistance change for the samples on 3000 nm pads than for those on 800 nm pads.

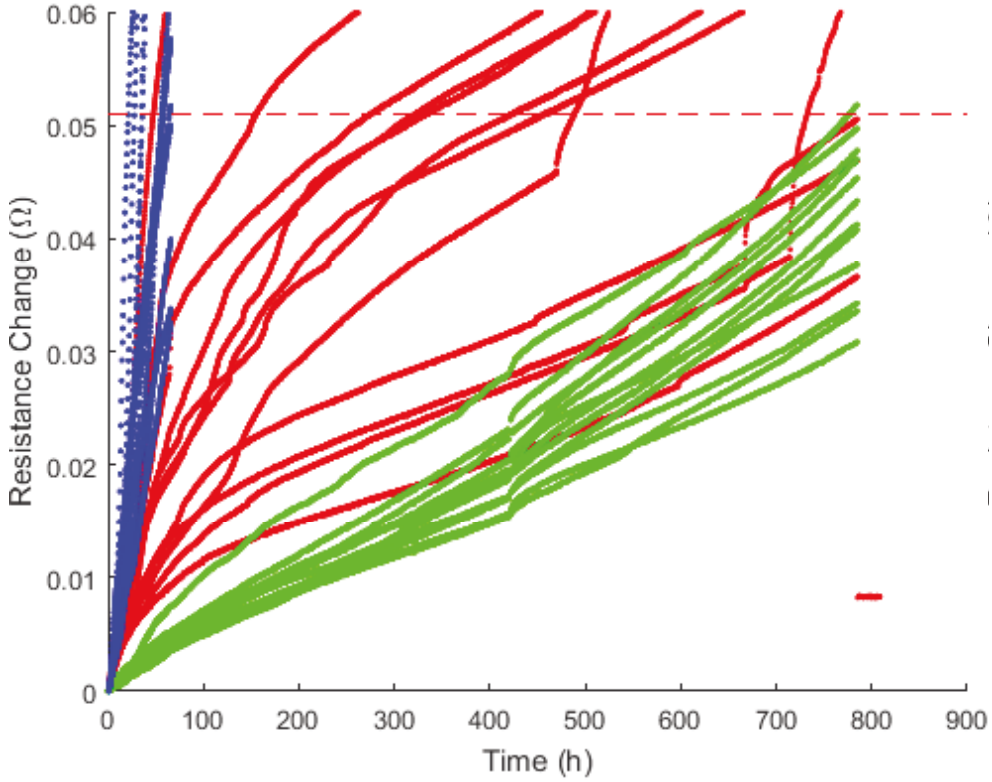

Fig. 4.12: Comparison of resistance changes for three different substrates with limited cleaning. Lines of the same colour correspond to wire bond pairs on the same substrate. All three substrates and all of the bonds were prepared using the same processes. Wires are PCC on 800 nm pads, aged at 225 °C without encapsulation.

4.4.2 Epoxy Encapsulant Type A Trials

Limited Cleaning

The first encapsulant tested in detail was Eccobond FP4450, produced by Loctite (Düsseldorf, Germany), and referred to as Epoxy A in this thesis. This is an epoxy encapsulant recommended by the manufacturer for use with Cu wire bonds. At 5 ppm, it has a much lower chloride ion content than the epoxy used in the pilot experiment, but its maximum operating temperature rating is 150 °C, which is exceeded in these tests. The material was used in spite of this limitation because no more suitable material had been found. With the limited cleaning process, PCC bonds using this encapsulant were tested at all three temperatures: 175 °C, 200 °C, and 225 °C, and on both pad thicknesses, 800 nm and 3000 nm. Results are shown in Figs. A.2 and 4.14. Bare Cu

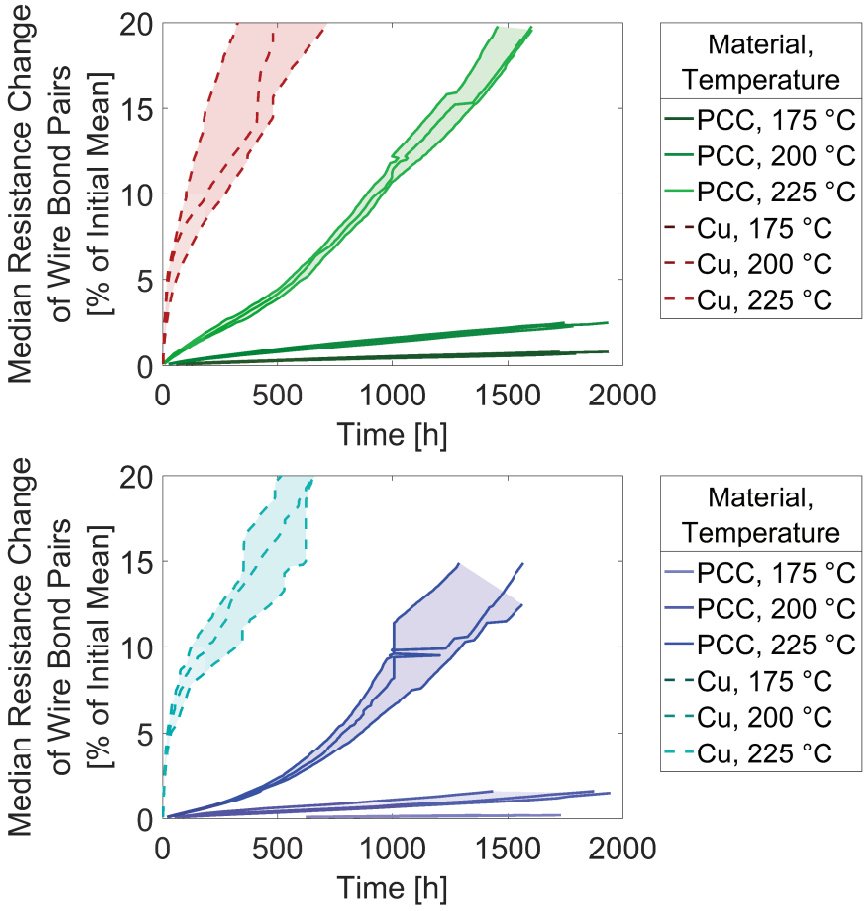

Fig. 4.13: Summary plots of unencapsulated aging behaviour with full cleaning. (a) 800 nm pad thickness. (b) 3000 nm pad thickness.

testing with this encapsulant was limited to the full cleaning process and 3000 nm pads, with results given in Section 4.4.2.

As expected, samples generally degraded faster at higher temperatures. Samples on 3000 nm pads initially degraded more slowly than those on 800 nm pads, but the degradation rate accelerated over time, whereas the samples on 800 nm degraded approximately linearly until failure, so that the median time to failure was not significantly different between the two groups when tested at the same temperature.

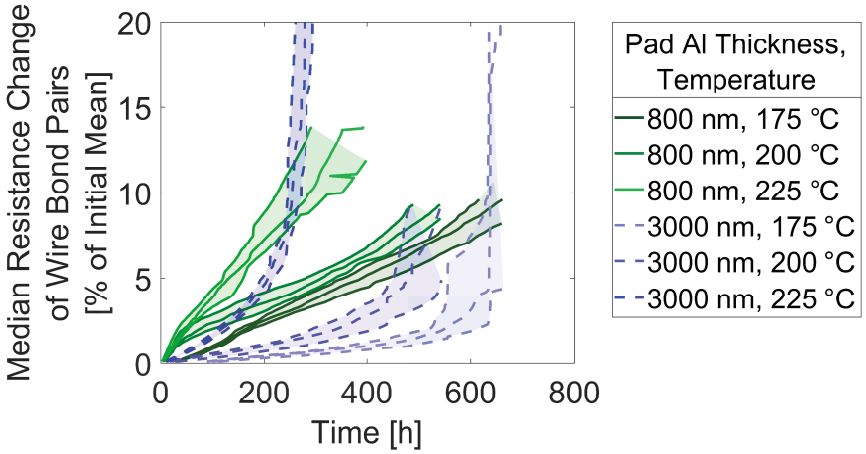

Fig. 4.14: Summary plots of PCC behaviour with Epoxy A and limited cleaning.

Full Cleaning

After developing the cleaning procedure, Epoxy A was tested again, in this case with both PCC and bare Cu wires and two bond diameters, using Bond Processes 2 to 5. Pad thickness for these tests was 3000 nm only. Results are shown in Figs. A.3 and 4.15.

At 200 °C and 225 °C, many sudden failures occurred, with samples on the same substrate failing at the same time. These concurrent failures were likely due to failure of the encapsulant, due to exceeding the recommended operating limit of 150 °C, rather than wire bond failures, since

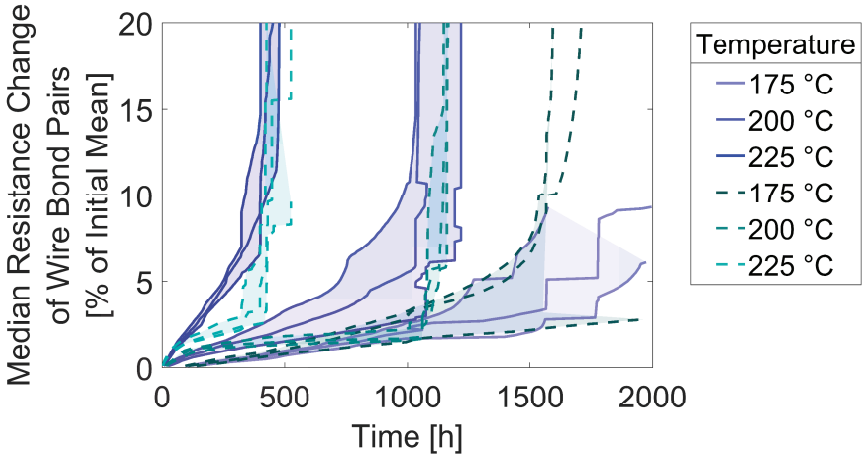

Fig. 4.15: Summary plots of PCC and bare Cu behaviour with Epoxy A and full cleaning.

there is no logical reason for multiple wires, with different materials and ball sizes, to fail at the same time. In contrast, encapsulant failure can result in the concurrent failures of all wires on a substrate. For instance, if the encapsulant delaminates from the substrate, the wires embedded in the encapsulant will be pulled with it, causing severe stress at the bond interface. Similar failures were also observed in the wire span experiments, described in Section 4.8. Such encapsulant failures make drawing conclusions about wire behaviour difficult, and no further samples were tested with this encapsulant.

4.4.3 Epoxy Encapsulant Type B Trials

The second encapsulant tested was 832HT, produced by MG Chemicals (Surrey, BC, Canada), referred to as Epoxy B in this thesis. It is sold as an encapsulating material for printed circuit boards and electronic assemblies, and is designed for high-temperature applications, with a constant service temperature rating of up to 225 °C. Using this material, 18 substrates were produced, and all 24 combinations of temperature, pad thickness, ball diameter, and wire coating were tested. Bond Processes 2 to 5 were used to produce the bonds. All 18 substrates received the full cleaning procedure. Figs. A.5, A.6, and A.7 show the resistance changes over time for 175 °C, 200 °C, and 225 °C, respectively. Figs. 4.16 and 4.17 summarize the data for all three temperatures, with estimates of the median resistance change and corresponding confidence intervals.

Similar to the unencapsulated and Epoxy A results, samples on 3000 nm pads degraded more slowly than those on 800 nm pads initially. However, at 225 °C, the only temperature for which failures occurred, the failure times did not significantly differ by pad thickness, again similar to

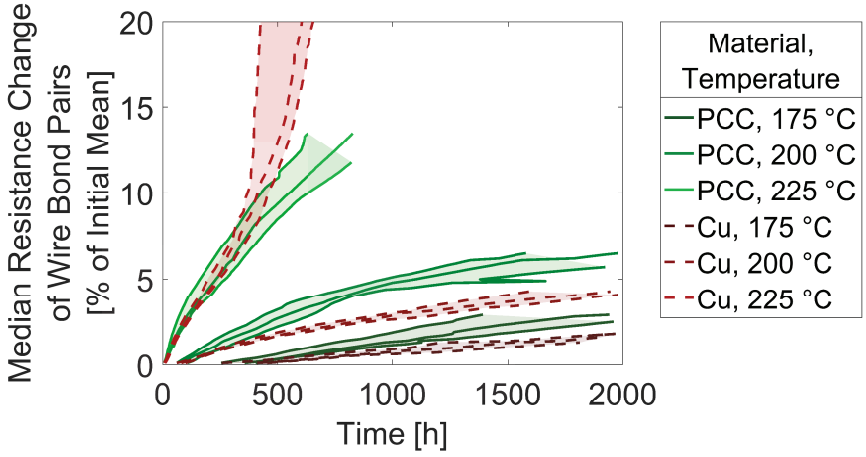

Fig. 4.16: Summary plot of aging behaviour with Epoxy B and full cleaning on 800 nm pads.

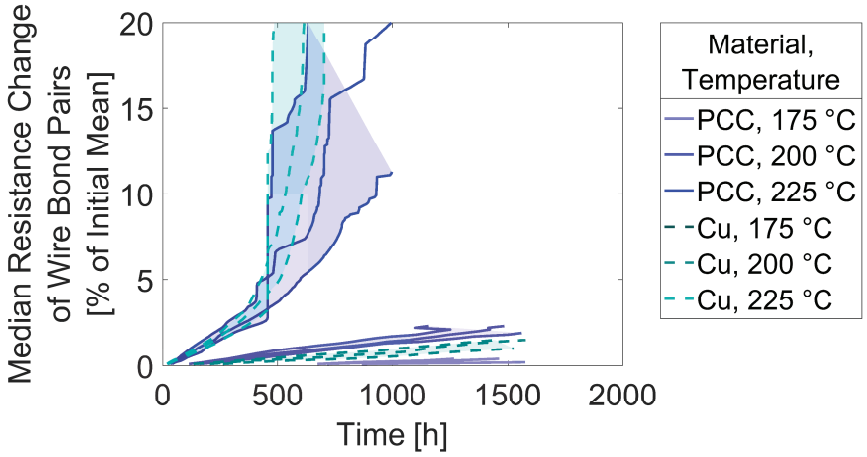

Fig. 4.17: Summary plot of aging behaviour with Epoxy B and full cleaning on 3000 nm pads.

previous results. Bare Cu degraded more slowly than PCC at 175 °C and 200 °C, with similar degradation rates for the two types at 225 °C.

4.4.4 Silicone Trials

The final encapsulant tested was Semicosil 915HT, produced by Wacker Chemie AG (Munich, Germany), a silicone-based encapsulant produced by Wacker Chemie AG and recommended for use as a semiconductor encapsulant. It is rated for use up to 210 °C. This product was tested on cleaned samples with 800 nm pad thickness, and all combinations of temperature, ball diameter, and wire coating, with bonds produced using Processes 2 to 5. Fig. A.8 shows the resistance changes over time, and Fig. 4.18 summarizes the results for all three temperatures.

Figs. A.8 and 4.18 show much better reliability for PCC wire than for bare Cu using this encapsulant. PCC reliability at 225 °C was excellent, except for one outlier. However, the PCC degradation behaviour did not show a large difference between 175 °C and 200 °C, which has negative implications when extrapolating to lower temperatures, as explored further in Sections 4.6 and 4.11.

4.5 Humidity Testing

PCC bonds encapsulated using Epoxy A were tested for 1000 h in the miniature environmental chambers of Section 2.1 without electrical bias, at nominal conditions of 85 °C and 85 % relative

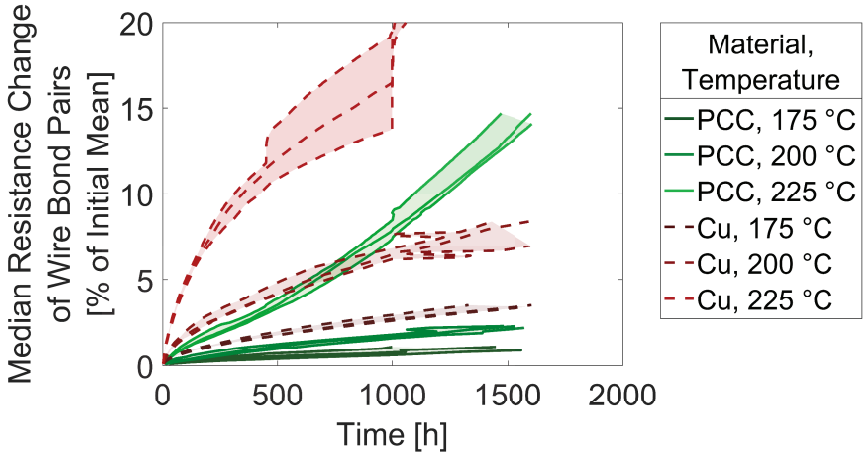

Fig. 4.18: Summary plots of aging behaviour with silicone encapsulant and full cleaning.

humidity, after preconditioning according to JEDEC MSL 3. No detectable resistance changes were observed under these conditions. This result indicates adequate reliability for many purposes. Given this result, this thesis focuses on HTS reliability, rather than attempting to study reliability in humid environments more broadly. For such a study, HAST capability would be highly advantageous, as typical temperatures of 110 °C to 130 °C would greatly accelerate aging behaviour. Other publications, referred to in 1.4.3, have investigated Cu bond reliability in humid environments in more detail.

4.6 Estimation of Activation Energies

Activation energies were estimated for each combination of wire material, pad thickness, and encapsulant as described in Section 1.7.4, and implemented in the file FailureRegression.m in Appendix C.5. Since many samples at low temperatures did not reach the failure condition of 10 % resistance increase, in some cases it was not possible to obtain a good activation energy estimate from the measured failure times. Instead, the times until lower degradation conditions were used. These times are referred to as the degradation times for a given degradation condition.

Figs. 4.19 and 4.20 show activation energies for various encapsulant, wire type, and pad thickness combinations. These are calculated over a range of degradation conditions, from 0.1 % to 10 % of initial mean resistance. Some plots show a reduced range of degradation conditions, with the range chosen based on the level of censoring for each group of samples: a significant number of degradation times must be observed for at least two temperatures in order to obtain

a good estimate of the activation energy. Table 4.1 lists activation energies for cleaned samples, estimated using a 1 % degradation condition.

For Epoxy A samples, the activation energy is low: 0.57 eV $\pm$ 0.09 eV at 95 % confidence for a 10 % degradation condition on 3000 nm pad with cleaning. Furthermore, the estimated activation energy is higher when calculated with low degradation conditions, then decreases when using higher conditions. Using a 1 % degradation condition, the activation energy for the same samples is 0.91 eV $\pm$ 0.14 eV. This change in activation energy suggests that at least two failure mechanisms contribute to the increase in resistance.

4.7 Assessment of Fit Quality

For each of the regression models in Section 4.6, fit assessment plots were produced as described in Section 1.7.5 and implemented in the file AssessFit.m in Appendix C.6. Some representative examples are shown in Fig. 4.21. Additional plots are presented in Appendix A.2. The log-normal model provides a moderately good fit for most sample groups, generally with better fits for samples on 800 nm pads than on 3000 nm pads, which may be due to the more linear behaviour of the resistance for 800 nm pads. Table 4.1 gives a subjective summary of the fit quality of each of the regression models fitted.

Table 4.1: Estimated activation energies with 95 % confidence intervals for various sample groups, all with full cleaning process. Calculated using a 1 % degradation condition. Fit quality is discussed in Section 4.7.

Encapsulant	Wire Material	Pad Thickness (nm)	Activation Energy (eV)	Fit Quality
None	PCC	800	1.41 ± 0.09	Poor
None	PCC	3000	1.09 ± 0.12	Moderate
Epoxy A	PCC	3000	0.96 ± 0.13	Poor
Epoxy B	PCC	800	1.21 ± 0.10	Good
Epoxy B	Cu	800	1.32 ± 0.08	Good
Epoxy B	PCC	3000	1.11 ± 0.19	Moderate
Epoxy B	Cu	3000	1.60 ± 0.32	Poor
Silicone	PCC	800	0.81 ± 0.13	Moderate
Silicone	Cu	800	0.98 ± 0.06	Moderate

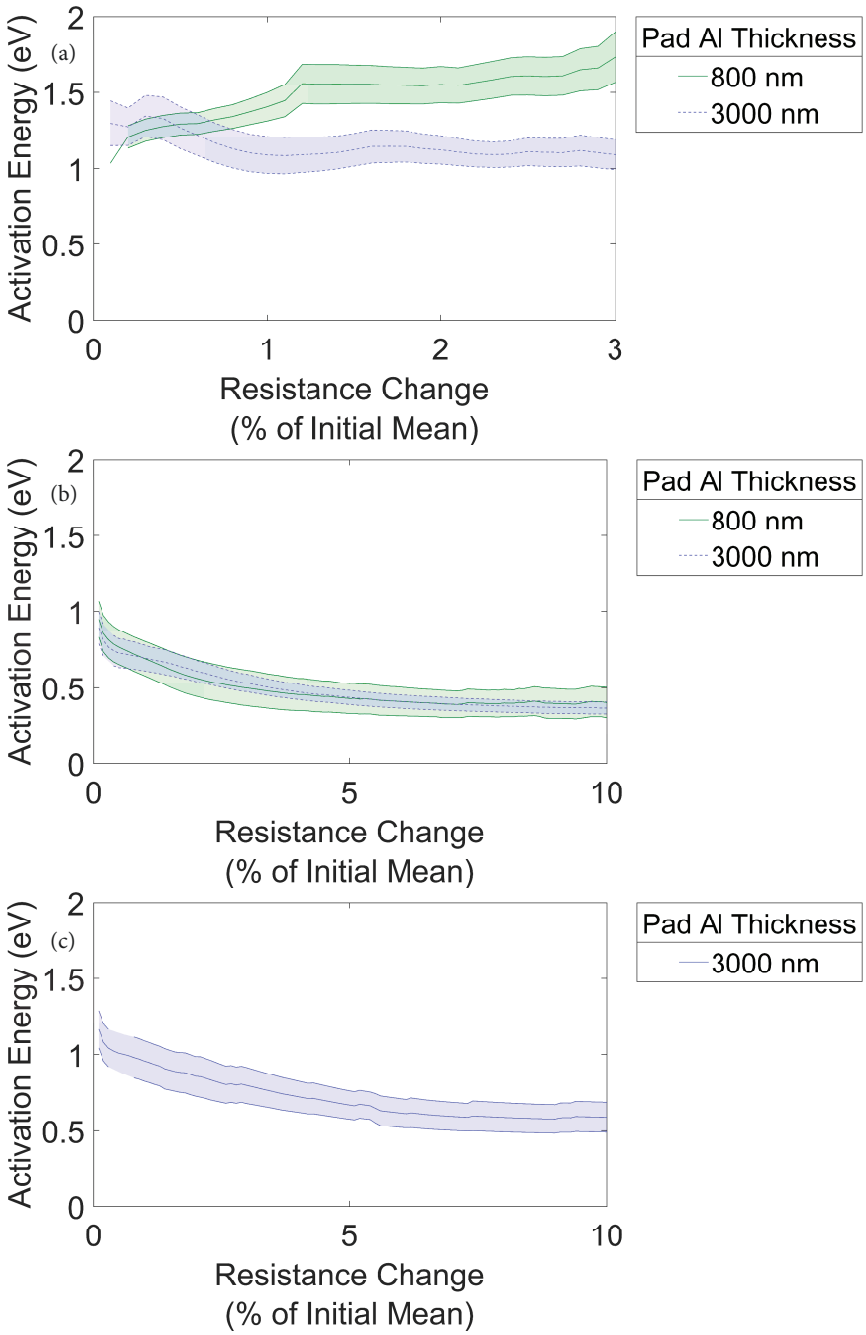

Fig. 4.19: Dependence of activation energy estimate on degradation condition for PCC wires. (a) Unencapsulated, full cleaning. (b) Epoxy A, limited cleaning. (c) Epoxy A, full cleaning.

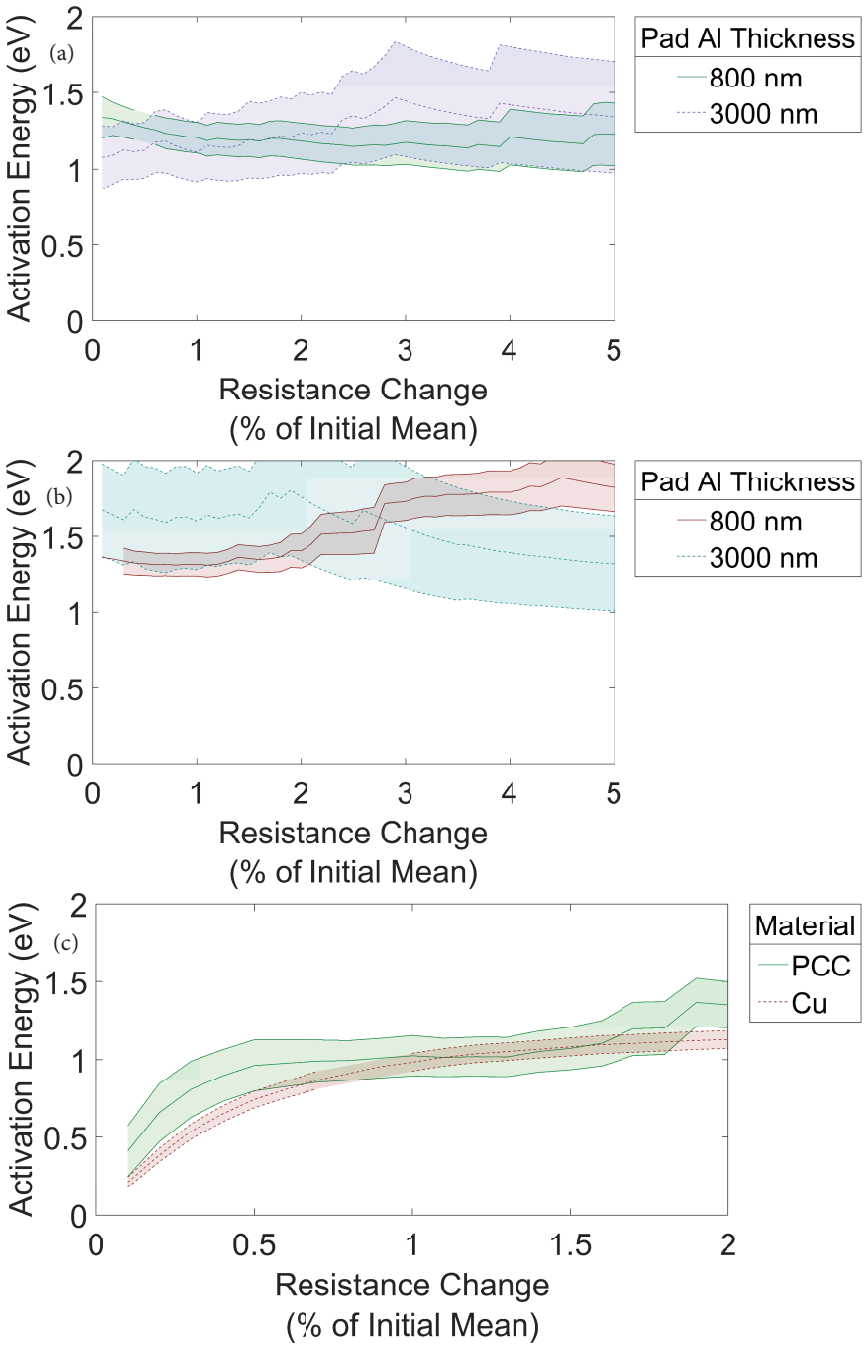

Fig. 4.20: Dependence of activation energy estimate on degradation condition with full cleaning. (a) Epoxy B, PCC wires. (b) Epoxy B, bare Cu wires. (c) Silicone, 800 nm pads.

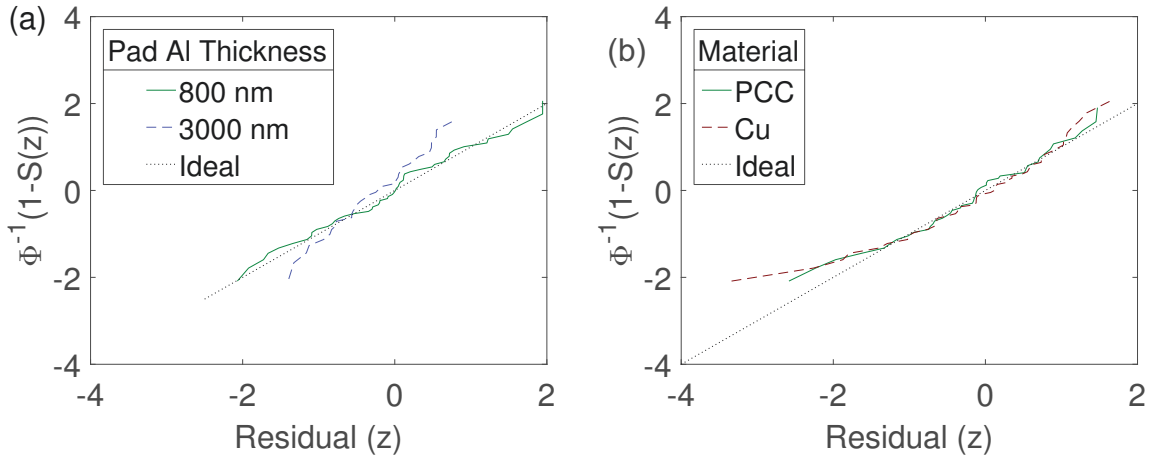

Fig. 4.21: Fit assessment plots based on log-normal model. (a) PCC bonds with Epoxy B, full cleaning. (b) Silicone encapsulant, 800 nm bond pads.

4.8 Wire Span Testing

To help determine the source of resistance increases, a procedure was developed for measuring the resistance of the central span of a wire, excluding any contribution from the bond interfaces or substrate metallization. This goal was achieved by first bonding a test wire between two leadfingers, then bonding auxiliary wires on top of the test wire, with their ball bonds placed near the ends of the test wire, and their wedge bonds placed on two additional leadfingers. A schematic of the wire placements is shown in Fig. 4.22 (a), and a photo of wires bonded in this configuration in Fig. 4.22 (b). This configuration enables a four-wire resistance measurement of the central span of the test wire, with current input through the two terminals directly connected to the test wire, and voltage measurements across the two outer terminals, connected to the test wire through the auxiliary wires.

Fig. 4.23 shows a diagram of the arrangement of all the wires on a wire span test substrate: eight test wires and 16 auxiliary wires give eight resistance signals per substrate.

Fig. 4.24 shows resistance change data for wire span samples using PCC and bare Cu wire at temperatures of 175 °C, 200 °C, and 225 °C. The PCC data shows consistent increasing behaviour at 200 °C and 225 °C, with no clear trends at 175 °C. The bare Cu data, in contrast, does not show consistent trends. For both wire types, sudden sharp increases in resistance occurred for all samples on a particular substrate at the same time, starting after about 400 h. As in Section 4.4.2, these events are attributed to encapsulant failure, not to degradation in the individual wire samples.

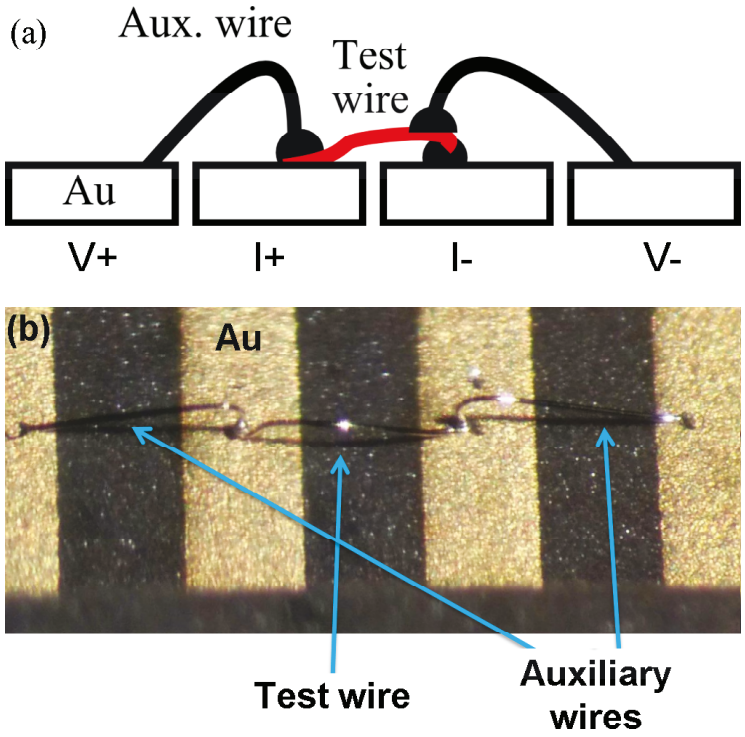

Fig. 4.22: (a) Schematic of wire sample for wire span resistance measurement. Only the portion of the test wire shown in red is included in the resistance measurement. (b) Photo of wire sample for wire span resistance measurement. Test wire is bonded first, then ball bonds of auxiliary wires are placed on top, near its two ends. Own work, reproduced from [98].

The resistance data for PCC wire spans can be used to estimate an activation energy, using the same approach as in Section 4.6. A degradation condition of 1 % resistance change was used, producing an estimate of 0.81 eV, with 95 % confidence interval 0.65 eV to 0.97 eV.

The resistance changes for these samples are small compared those for the standard wire bond pairs. For instance, with PCC wire at 200 °C, the median resistance change in the wire span samples after 1000 h was 1.0 % of the initial mean. For wire pair samples in the same conditions, the median resistance change was 5.8 % of the initial mean,. Similarly, after 400 h at 225 °C, the median resistance change in PCC wire spans was 1.1 %, whereas the median change for wire pairs in the same conditions was 10.2 %. Since there was no consistent resistance change behaviour for the other four groups of wire span samples, it was concluded that the wire span contributes negligibly to the resistance changes measured for the wire pair samples.

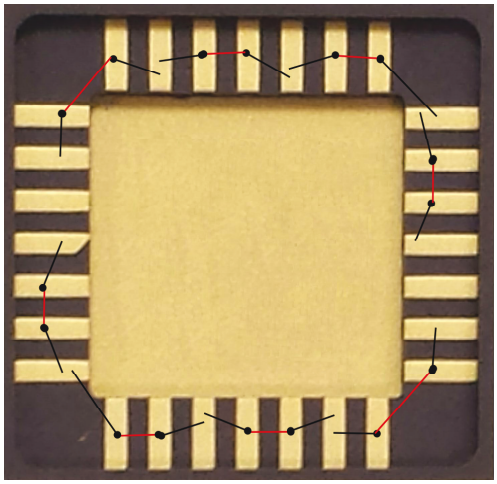

Fig. 4.23: Diagram of wire layout for wire span resistance samples. Eight test wires (red) and 16 auxiliary wires (black) are bonded on each substrate, allowing eight resistance signals. Own work, modified from [98].

4.9 Cross-Sections for Investigation of Failure Mechanisms

After aging, several samples were cross-sectioned for failure analysis. To cross-section these samples, the die and wire bonds needed to be separated from the extremely hard ceramic substrate. For unencapsulated samples, this was achieved by heating the substrates on a 400 °C hot plate for about 30 s, which weakened the die attach epoxy enough to remove the die mechanically. The loose die was then encapsulated in epoxy for grinding and polishing.

For samples aged with encapsulation, the substrate was cut four times using a diamond abrasive saw, as shown in Fig. 4.25, leaving only one surface of the encapsulant in contact with the ceramic substrate. At this stage, the encapsulant separated easily from the substrate, with the die still embedded in the encapsulant. Ball bond cross-sections for both types of samples could then be prepared by standard techniques of grinding with SiC abrasive paper, then polishing with diamond particle suspensions, to a minimum particle size of 100 nm. Samples could then be observed by optical microscopy or by electron microscopy after sputter coating with gold to produce a conductive surface.

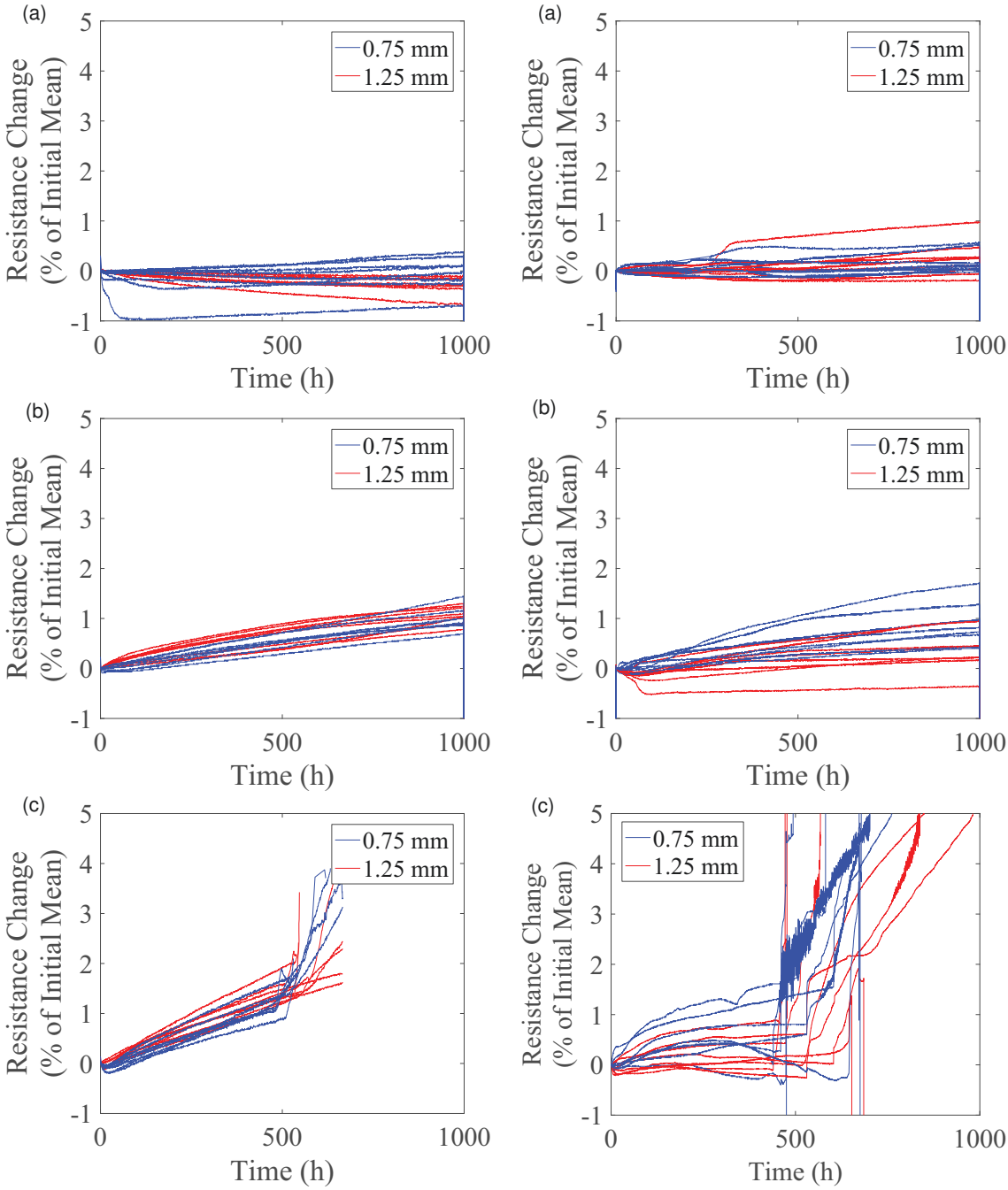

Fig. 4.24: Resistance changes of wire span samples over time with Epoxy A. Left side: PCC wire. Right side: bare Cu wire. (a) 175 °C. (b) 200 °C. (c) 225 °C.

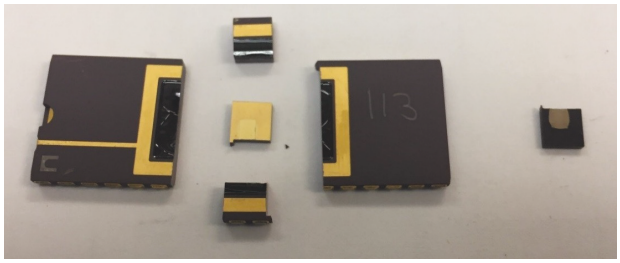

Fig. 4.25: Encapsulated sample after cutting four times with diamond abrasive saw. After four cuts, the Si die, embedded in the encapsulant (black square at right), separates easily from the substrate.

Fig. 4.26 shows cross-sections of samples before aging for comparison purposes. Figs. 4.27 to 4.32 show cross-sections for a variety of samples after aging. As expected, after aging, intermetallic layers are observed below the Cu ball, with the full Al pad thickness consumed in many cases. Cracks are also observed between the bulk Cu and IMC layers, in severe cases spanning the entire width of the bonded ball. Other samples, such as in Fig. 4.31, had begun crack formation, but the crack had not yet grown across the entire interface.

The cracks are likely the primary mechanism leading to ultimate bond failure. In samples aged without encapsulation, no crack was observed after aging at 175 °C, and a short crack, not spanning the whole interface, after aging at 225 °C. Referring to the activation energies in Section 4.6, these results suggest that the higher activation energies observed for the more reliable encapsulants reflect intermetallic growth, with an activation energy between 1.0 eV and 1.6 eV. The lower activation energy of 0.5 eV to 0.7 eV then likely corresponds to crack formation and growth at the bond interface.

Energy dispersive x-ray (EDX) analysis of cross-sections did not detect any unexpected or corrosive chemical elements: those observed were Cu, Al, and Si in their expected locations, C in the epoxy encapsulant, and Au applied prior to SEM imaging. This result rules out high concentrations of contaminants the bonding interface, but trace quantities may still be present and contribute to bond degradation, since EDX is not sensitive to concentrations below about 1 %.

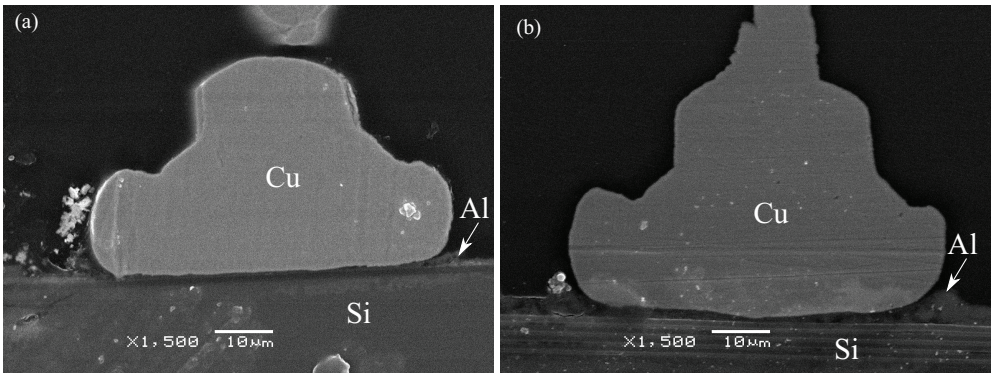

Fig. 4.26: PCC cross-sections before aging. (a) 800 nm pad thickness. (b) 3000 nm pad thickness.

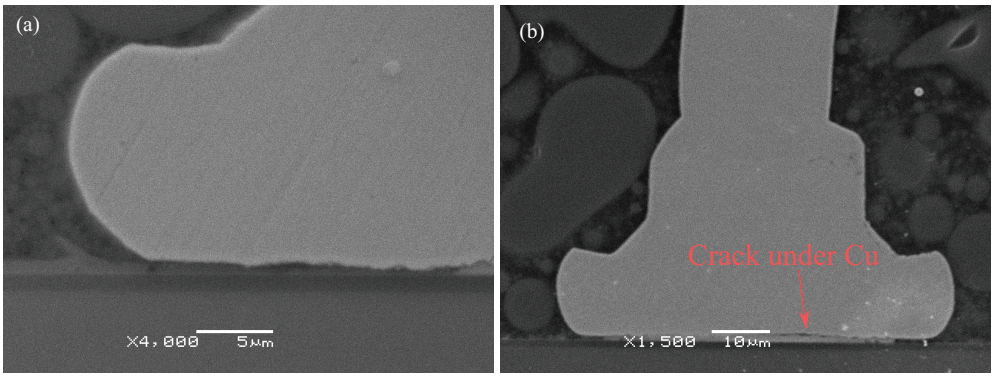

Fig. 4.27: PCC cross-section after aging with Epoxy A, limited cleaning, 800 nm pad thickness. (a) 666 h at 175 °C. (b) 371 h at 225 °C

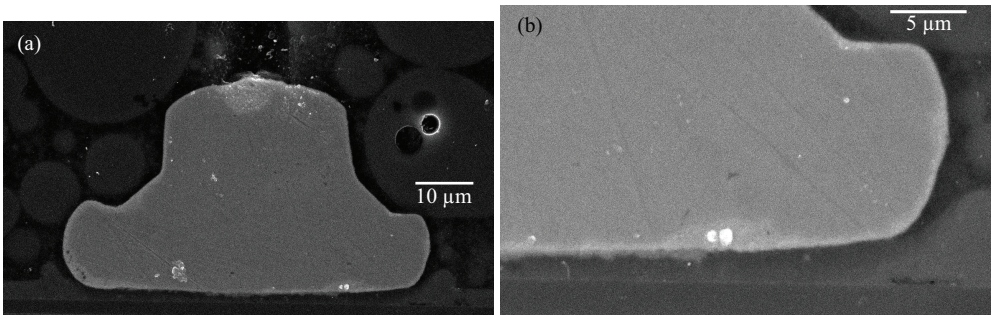

Fig. 4.28: PCC cross-sections after aging 664 h at 175 °C with Epoxy A, limited cleaning, 3000 nm pad thickness.

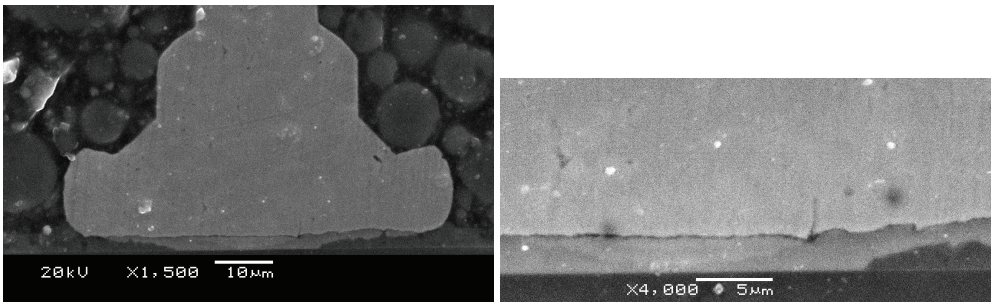

Fig. 4.29: PCC cross-sections after aging 401 h at 225 °C with Epoxy A, limited cleaning, 3000 nm pad thickness

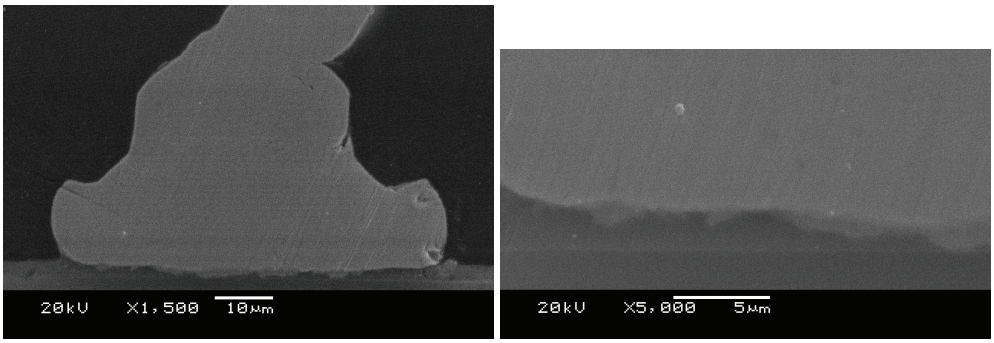

Fig. 4.30: PCC cross-sections after aging 1955 h at 175 °C in air, full cleaning.

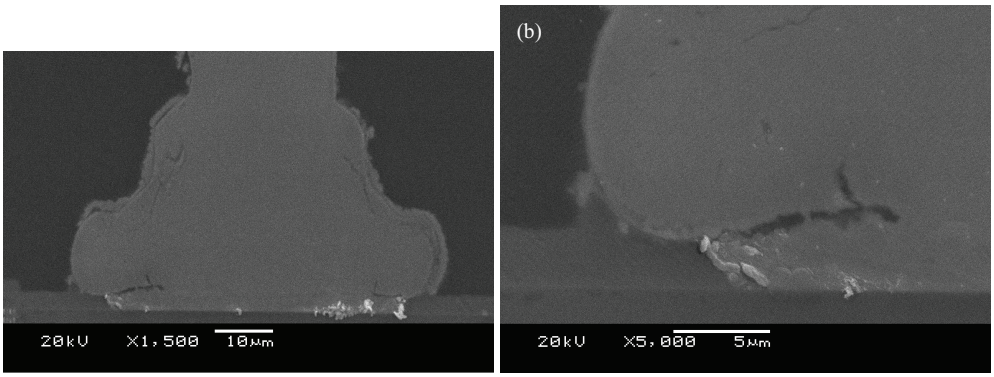

Fig. 4.31: PCC cross-section after aging 982 h at 225 °C in air, full cleaning.

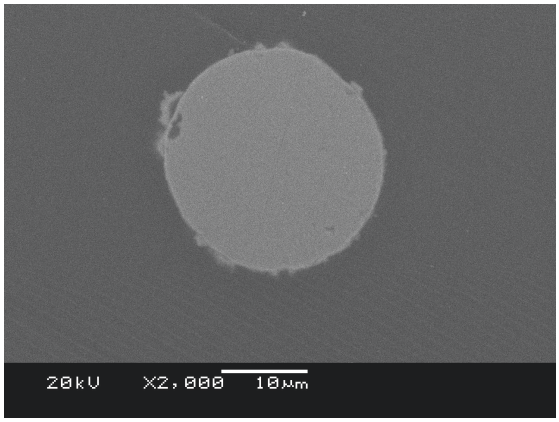

Fig. 4.32: PCC wire cross-section after aging 982 h at 225 °C in air, full cleaning. Voids are visible near the wire surface, similar to those described in [66] and attributed to galvanic corrosion.

4.10 Factor Comparisons

4.10.1 Cleaning Procedure

The full cleaning procedure greatly improved bond lifetime and also reduced the variability between samples with the same preparation. No attempt was made to estimate activation energies without the full cleaning procedure, since repeatability was poor.

4.10.2 Al Bond Pad Thickness

Examining the median resistance plots in Section 4.4, it is seen that thicker 3000 nm bond pads resulted in slower initial resistance changes compared to 800 nm pads. However, the resistance change for the 3000 nm pads was more strongly non-linear with respect to time, with the rate of resistance change increasing over time. Ultimately, for conditions that resulted in bond failure, the failure times were similar between samples on 800 nm and on 3000 nm pads. Likewise, the activation energy plots in Figs. 4.19 to 4.20 show overlapping confidence bands in most cases, suggesting that the same physical mechanisms lead to failure in both cases.

4.10.3 Encapsulant

Figs. 4.33 to 4.36 compare median resistance behaviour for wire pairs with all three encapsulants and in air.

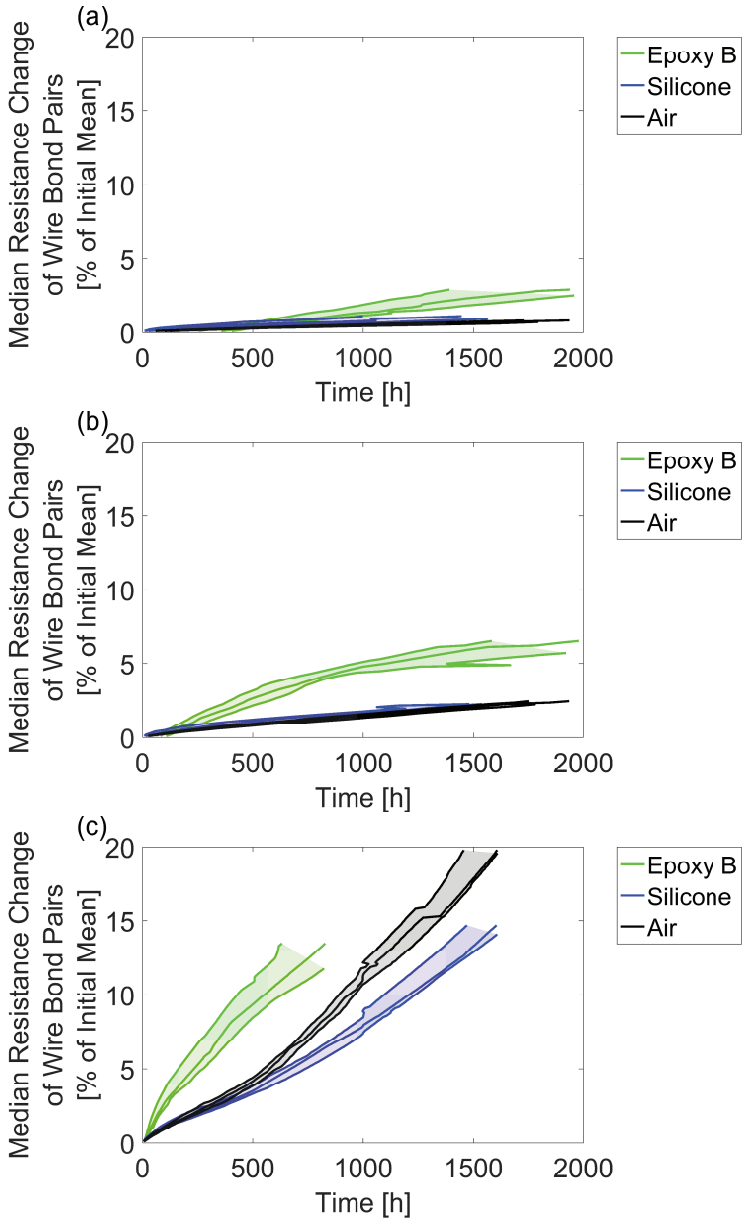

Fig. 4.33: Median resistance change plot for comparing PCC lifetimes with different encapsulants on 800 nm pads. (a) 175 °C. (b) 200 °C. (c) 225 °C.

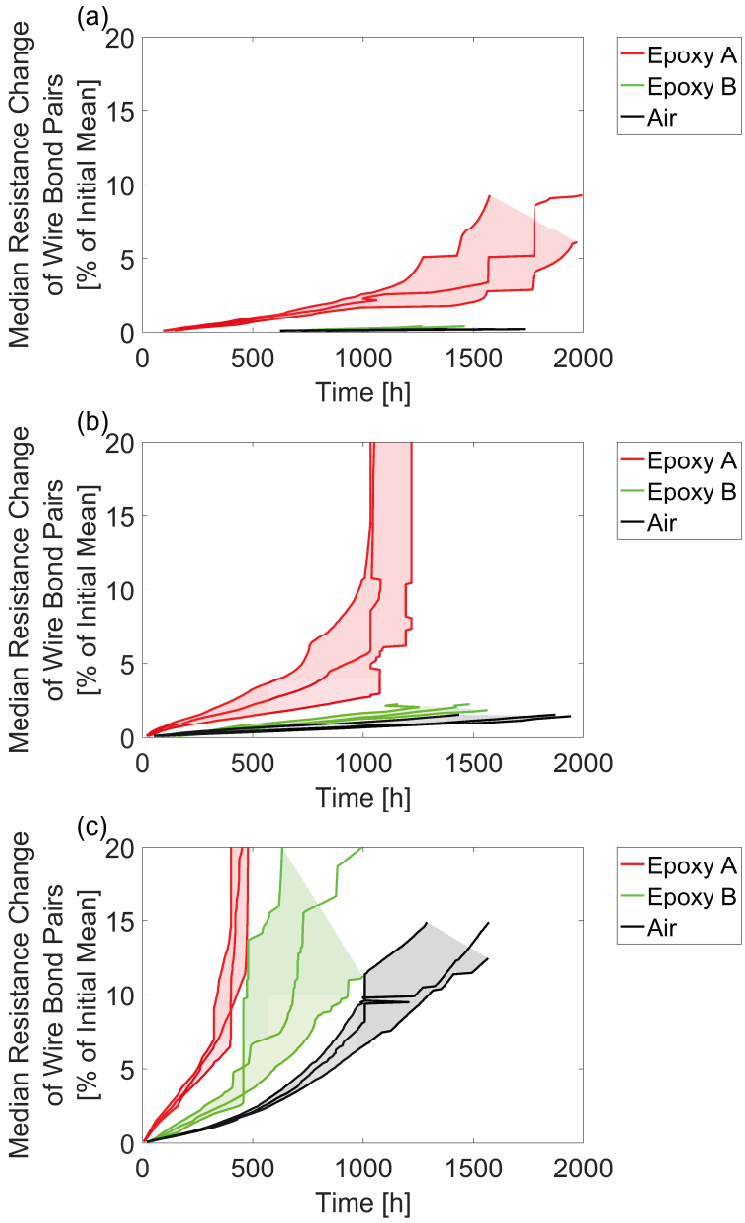

Fig. 4.34: Median resistance change plot for comparing PCC lifetimes with different encapsulants on 3000 nm pads. (a) 175 °C. (b) 200 °C. (c) 225 °C.

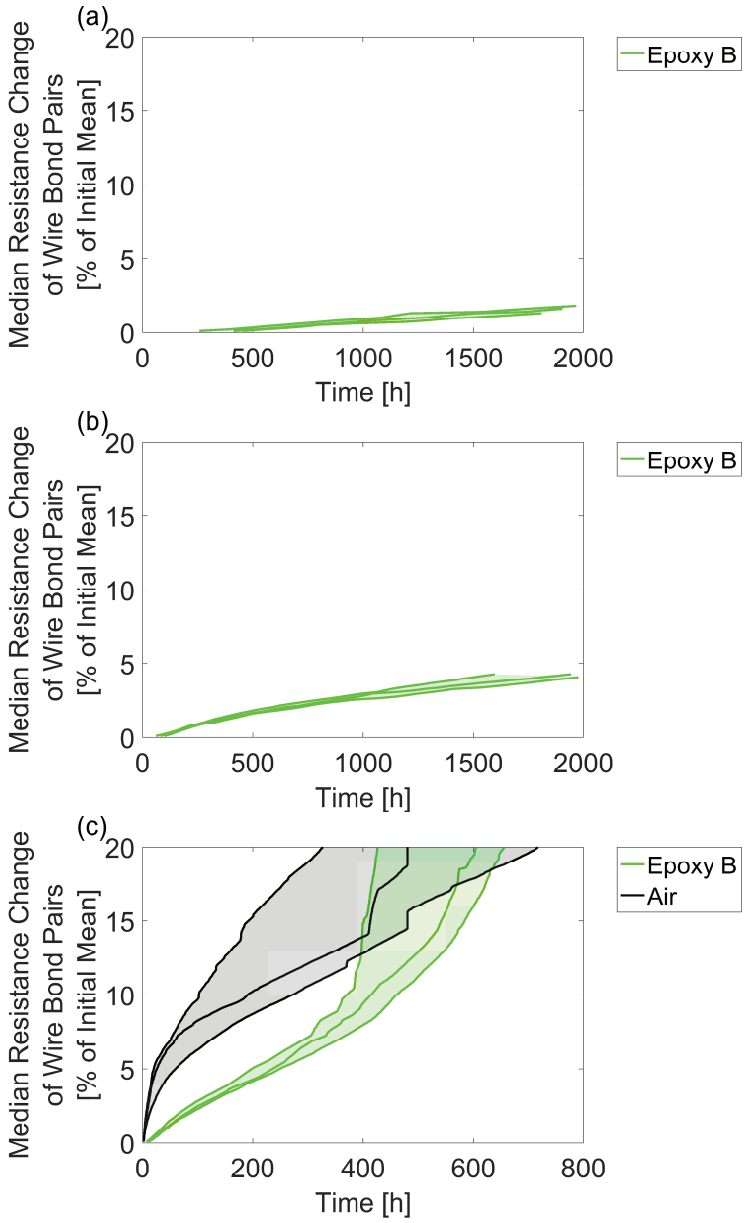

Fig. 4.35: Median resistance change plot for comparing bare Cu lifetimes with different encapsulants on 3000 nm pads. (a) 175 °C. (b) 200 °C. (c) 225 °C.

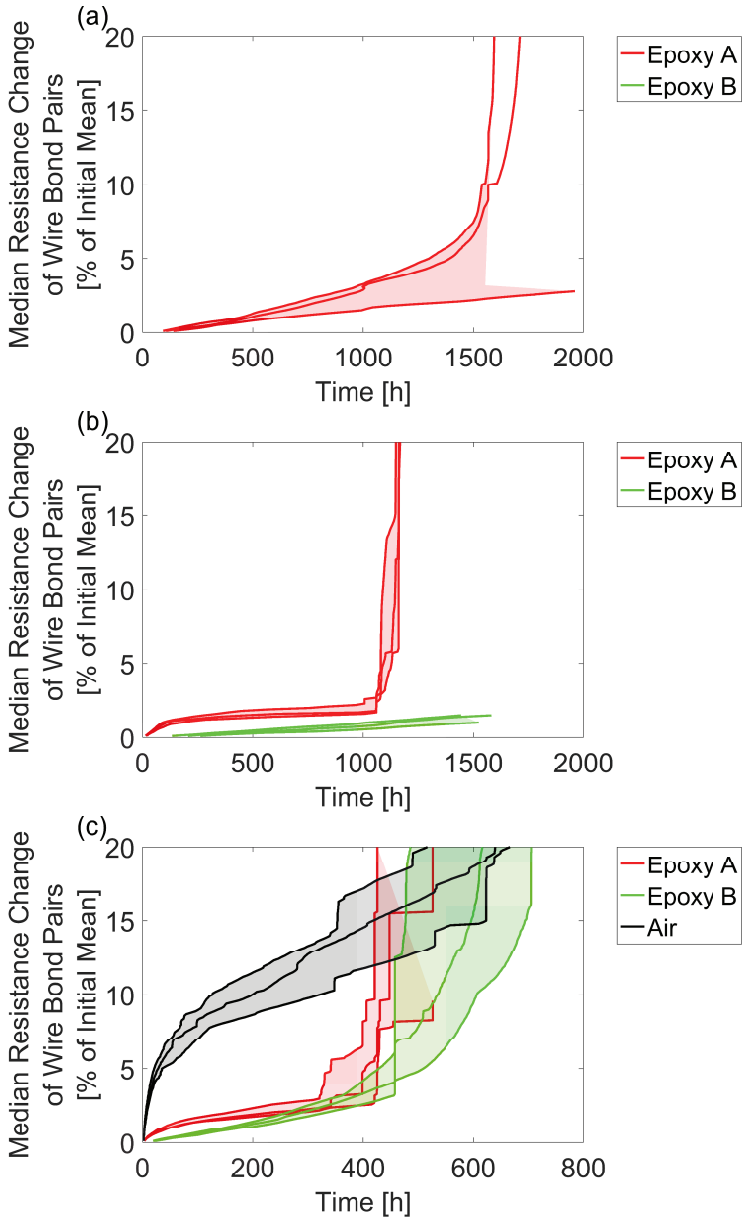

Fig. 4.36: Median resistance change plot for comparing bare Cu lifetimes with different encapsulants on 3000 nm pads. (a) 175 °C. Epoxy B samples do not appear because median resistance change is less than 0.1 %. (b) 200 °C. (c) 225 °C.

For PCC wire, Epoxy A gave the poorest performance, with wires failing earlier than for equivalent conditions in any other encapsulant or in air. PCC wires in silicone gave excellent reliability performance at 200 °C and 225 °C, matching or exceeding the performance of unencapsulated bonds, but at 175 °C, the performance was worse than for unencapsulated samples and more similar to Epoxy B. These results demonstrate a weaker temperature dependence of the degradation behaviour in silicone, which is also reflected in the lower activation energy of Fig. 4.20 (c) compared to results for Epoxy B or in air, as in Figs. 4.20 and 4.19 (a), respectively.

4.10.4 Pd Coating

The effect of the Pd coating depends strongly on the choice of encapsulant. With epoxy encapsulants, bare Cu degraded more slowly than PCC. However, PCC wire showed more consistent performance over the full range of encapsulations than did bare Cu wire: bare Cu performed poorly in air or in silicone encapsulation, with much shorter lifetimes than for PCC wire. This poor performance of bare Cu may be due to oxidation by ambient O_2, with silicone being highly permeable to gases and therefore insufficient to protect the bare Cu wires. For PCC wire samples, the Pd coating is able to protect the interior Cu from oxidation, resulting in less severe resistance degradation.

4.10.5 Ball Bond Diameter

The ball bond diameter had at most a small effect on bond lifetimes. To illustrate, Figs. 4.37 and 4.38 show median resistance changes over time with Epoxy B for PCC and bare Cu wires, respectively. Only Fig. 4.37 (a) shows non-overlapping confidence bands for the 61 µm and 75 µm diameters. This result suggests that the fraction of the bond area covered by IMCs is approximately the same for both bond sizes, as the processes were optimized to have the same shear strength. The bond resistances then increase as the IMC layers grow in thickness.

Bond diameter can also be added to the AFT model of Eq. (1.30) as an additional covariate:

$$\log(T) = g_0 + g_1 x_1 + g_2 x_2 + bZ. \tag{4.8}$$

Repeating the fittings from Section 4.6 with x_2 as the nominal bond diameter, typical results for the coefficient g_2 range from 0 to -0.03, with statistically significant differences from zero in some cases. To understand what this result means for bond lifetimes, Eq. (4.8) can be rewritten as

$$T = \exp(x_0)\exp(x_1 g_1)\exp(g_2 x_2)\exp(bZ). \tag{4.9}$$

Then the ratio of lifetime estimates for large and small bonds, assuming other factors are the same, including the error term Z, is

$$\frac{T_{\text{large}}}{T_{\text{small}}} = \frac{\exp(g_2 x_{2,\text{large}})}{\exp(g_2 x_{2,\text{small}})} = \exp[g_2(x_{2,\text{large}} - x_{2,\text{small}})] \tag{4.10}$$

For these experiments, $x_{2,\text{large}} = 75$ and $x_{2,\text{large}} = 61$, so the lifetime ratio for $g_2 = -0.03$ is

$$\frac{T_{\text{large}}}{T_{\text{small}}} = \exp[-0.03 * (75 - 61)] = 0.66, \tag{4.11}$$

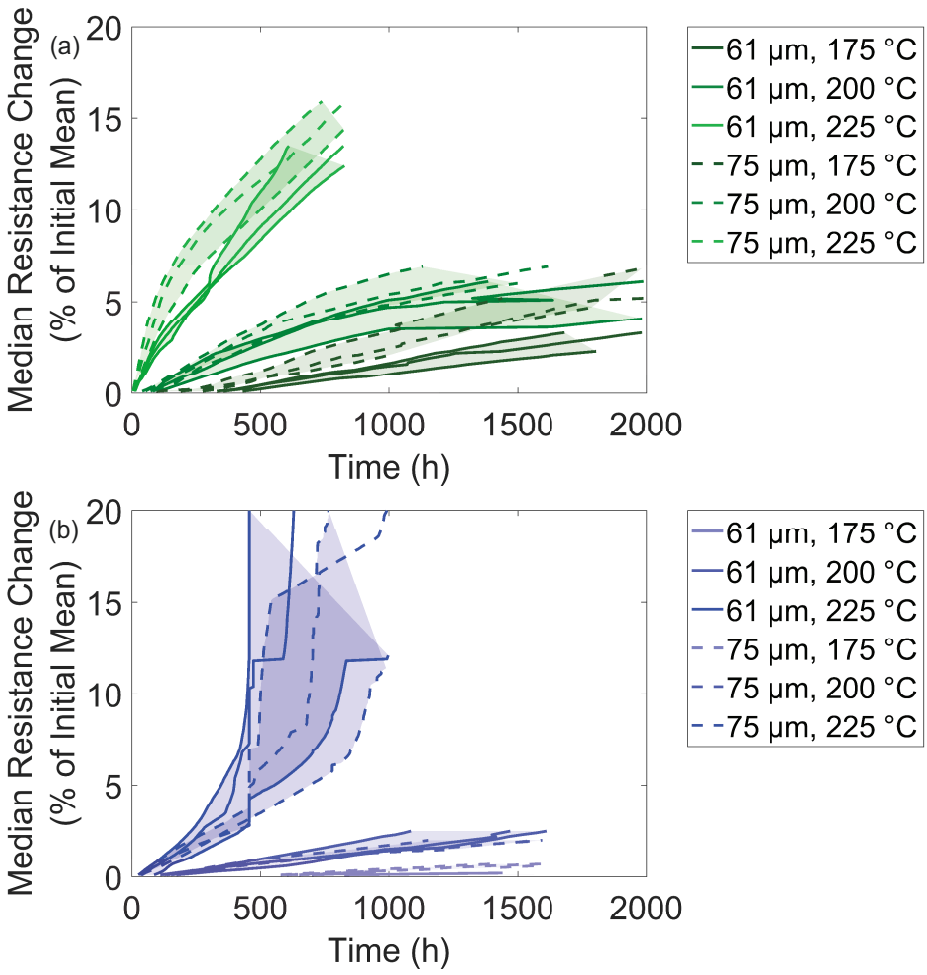

Fig. 4.37: Median resistance change plot for comparing PCC lifetimes with Epoxy B for 61 µm and 75 µm diameter bonds. (a) 800 nm pad thickness. (b) 3000 nm pad thickness.

meaning that in the worst case, the mean lifetime for 75 µm bonds would be 66 % of the mean lifetime for 61 µm bonds.

4.11 Predictions for Lower Temperatures

Fig. 4.39 outlines the steps involved in predicting bond lifetimes, beginning from data collection, and ending with extrapolation of a fitted AFT model, as described in this section and implemented in the file LifetimeExtrapolation.m in Appendix C.7. The extrapolation was based on AFT models

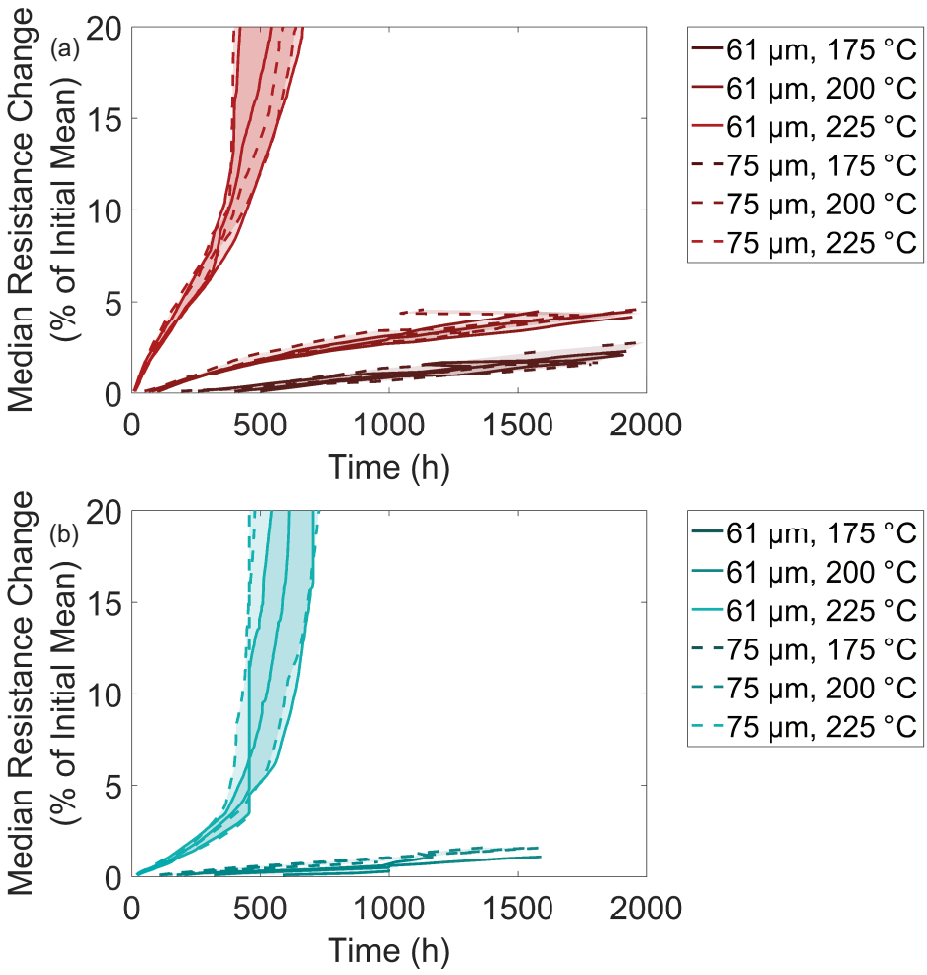

Fig. 4.38: Median resistance change plot for comparing bare Cu lifetimes with Epoxy B for 61 µm and 75 µm diameter bonds. (a) 800 nm pad thickness. (b) 3000 nm pad thickness.

with log-normal failure distributions, used to estimate the time until a particular failure probability at a given temperature. Then these results were inverted to obtain the maximum temperature for which the failure probability remains below a specified limit for a given duration.

Degradation times for 1 % resistance increase were used for the following calculations, since many samples at 175 °C or 200 °C did not degrade significantly beyond 1 %. Then, to estimate times until the original failure condition of 10 %, the estimated times were multiplied by 10, since the resistances grew approximately linearly with time before failure. This extrapolation is based on the observed pattern of near-linear intial resistance growth, followed by more rapid growth as a bond approaches failure, with the assumption that this trend is maintained at lower temperatures. Physically, these two stages of degradation are attributed to IMC growth and crack growth, respectively. The two stages are related, since interface cracking is expected to occur when the Cu-rich IMCs reach sufficient thickness for severe corrosion or stress cracking as in [63].

The failure times were calculated using Eq. (1.40), with the model coefficients $\hat{g}_0$, $\hat{g}_1$, and $\hat{b}$ from Section 4.6, to calculate the time t_p until a failure probability p over a range of temperatures. The failure probabilities used were $p = 0.5$ and $p = 10^{-6}$ (1 ppm). Similarly, Eq. (1.47) was used to calculate upper and lower confidence bounds for each time value.

Figs. 4.40 to 4.43 show the resulting t_p values for various combinations of encapsulant, wire type, and pad thickness. From these plots, the intersection of the t_p curve with the horizontal line for a particular duration t gives the maximum temperature for which the wires have a probability p of surviving until time t. Confidence bounds for the maximum temperature can likewise be identified as the intersections of the t_p confidence bounds with the same horizontal line.

Table 4.2 summarizes the maximum temperature estimates for a lifetime requirement of 12000 h. For industries with high reliability requirements, such as automotive, the results for 1 ppm failure probabilities are more relevant than those for 50 % failure probabilities. Comparing these results, the unencapsulated samples are seen to be reliable at the highest temperature of 167 °C. Bare Cu bonds in epoxy B performed second best, with an estimated temperature limit of 159 °C. Silicone performed poorly, especially with bare Cu wire, with temperature limits of 141 °C for PCC wire and 125 °C for bare Cu.

Table 4.2: Estimated temperature limits with 95 % confidence intervals for 12000 h extrapolated lifetime of Cu wire bonds, depending on encapsulant, wire type, pad thickness, and allowed failure probability. Sample groups with fit quality judged "poor" in Table 4.1 are omitted.

Encapsulant	Wire	Pad Thick. (nm)	1 ppm Fail Temp. (°C)	50 % Fail Temp. (°C)
None	PCC	3000	167 ± 6	198 ± 2
Epoxy B	PCC	800	145 ± 6	171 ± 3
Epoxy B	Cu	800	159 ± 4	177 ± 2
Epoxy B	PCC	3000	154 ± 11	191 ± 5
Silicone	PCC	800	141 ± 10	177 ± 4
Silicone	Cu	800	125 ± 5	141 ± 3

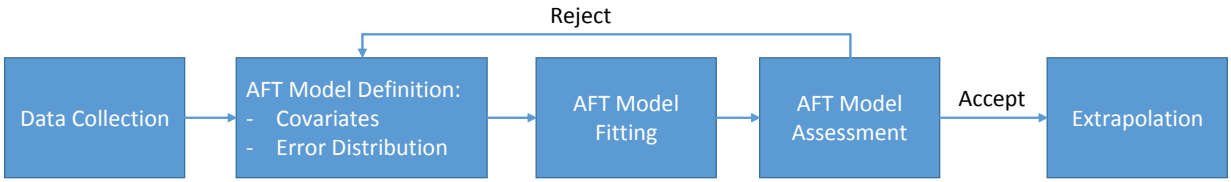

Fig. 4.39: Flow chart of procedure for obtaining lifetime extrapolations, beginning from data collection.

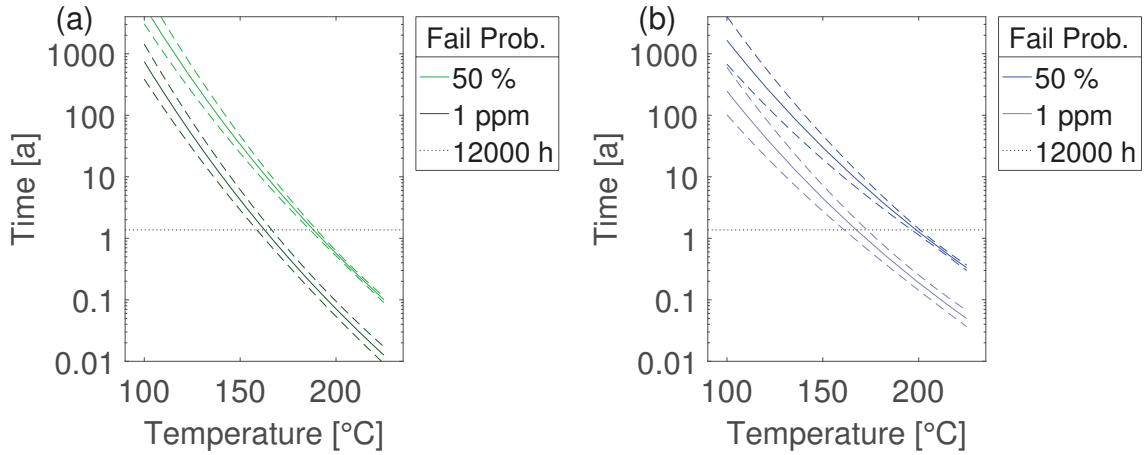

Fig. 4.40: Extrapolation for PCC wire without encapsulation. (a) 800 nm pads. (b) 3000 nm pads.

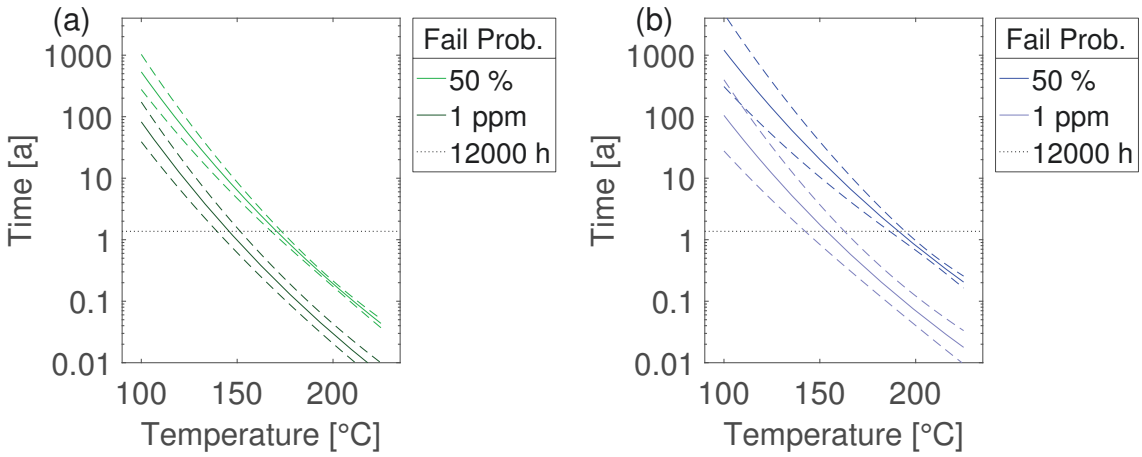

Fig. 4.41: Extrapolation for PCC wire with Epoxy B. (a) 800 nm pads. (b) 3000 nm pads.

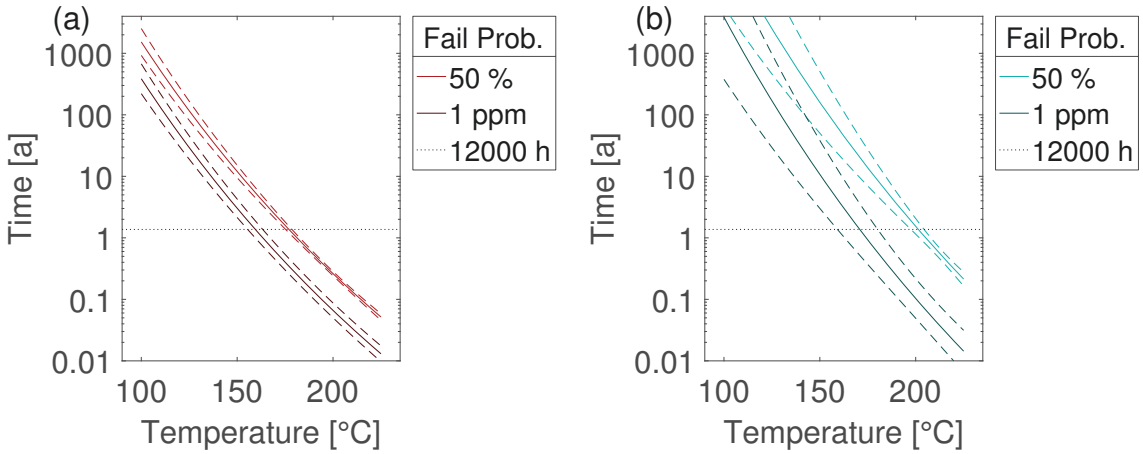

Fig. 4.42: Extrapolation for bare Cu wire with Epoxy B. (a) 800 nm pads. (b) 3000 nm pads.

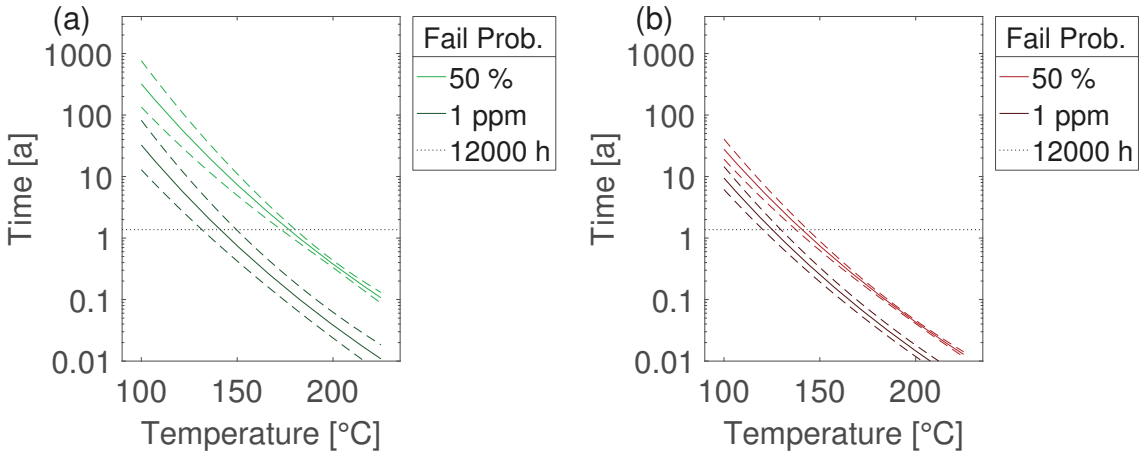

Fig. 4.43: Extrapolation for bonds on 800 nm pads with silicone encapsulant. (a) PCC wire. (b) Cu wire.

Chapter 5

Conclusions

Objectives 1, 2, and 3 listed in Section 1.3 were met. Capabilities for environmental testing of microelectronics at UW have been improved, including better temperature control accuracy and a new type of humidity testing system now available, capable of testing microelectronic devices in up to ten different conditions in parallel. New techniques have been demonstrated for ball bond process optimization that, compared to previous similar work, can reduce errors without needing any additional experimental steps. Additional process factors and responses can also be included in a convenient way, resulting in a higher-quality final process.

Effects on reliability were clearly demonstrated for the cleaning procedure, choice of encapsulant, and Pd wire coating. The choice of PCC or bare Cu wire should be made carefully, taking the choice of encapsulant into account. Although the Pd coating yields improvement in bond process windows and wire shelf life, it can lead to reduced wire lifetime at high temperatures for some choices of encapsulant. Conversely, if wire-bonded devices are used in air without encapsulation or with a highly permeable encapsulant, the Pd coating offers considerable protection from atmospheric oxygen, giving a large advantage in reliability compared to bare Cu wire. In constrast, pad thickness and ball diameter were shown to have minor effects on bond reliability in some cases, and no significant effect in others, so that these can be chosen primarily to meet requirements of the fabrication and bonding steps.

Statistical techniques based on accelearted failure time models have been demonstrated for analysis of experimental reliability data, in which observations are frequently censored due to time limitations. These models can be used to properly account for censored data and make strong conclusions about sample reliability, including assessment of uncertainty, without waiting for all test samples to fail.

Using these statistical techniques, predictions of Cu wire bond lifetimes have been made, answering an important question of what is the maximum temperature for which Cu bonds are reliable and meeting Objective 4. The results of Chapter 4 suggest that, using typical low-cost processes, reliable Cu bond operation is possible up to about 160 °C. This is a useful temperature for many automotive applications; the Automotive Electronics Council only defines qualification tests for operating temperatures up to 150 °C. However, operation at even higher temperatures remains desirable. Achieving this goal would require novel processing techniques or alternative materials such as different pad metallizations, more advanced encapsulants, or hermetic package sealing in an oxygen-free environment. Post-bonding treatments could also be investigated, to determine whether a more stable initial structure can be produced at the bond interface, for instance by annealing in an oxygen-free environment at high temperature.

The accelerated failure time model based on the Arrhenius equation was found to fit the reliability data well. However, confidence in the resulting reliability estimates is weakened by multiple levels of unverified extrapolation that were necessary to obtain meaningful results. In the future, to improve the quality of Cu wire bond reliability predictions, longer-duration aging tests

could be performed to reduce the degree of extrapolation required for estimating lifetimes and maximum temperatures. Samples could be tested at one or more additional high temperatures, for instance 210 °C, to avoid the problem of heavy censoring at low temperatures, especially for processes already achieving very good high-temperature reliability. Bond resistance data could be combined with cross-sections at specific resistance levels along with finite element modelling of the bond interface to relate resistance degradation behaviour to IMC and crack growth.

An essential consideration that was not addressed in this thesis is the bond reliability in other forms of aging test, such as thermal cycling. This concern must be addressed by comprehensive environmental and mechanical testing of the bonds prior to use in mass-production. Models similar to the accelerated failure time models used in this thesis may be useful for other types of environmental testing as well, and could be evaluated for suitability in thermal cycling or humidity testing, for example. This type of model has great value and could be used more broadly, with applications extending beyond the area of wire bond reliability.

References

[1] M. D. Hook, S. Hunter, and M. Mayer. Deriving lifetime predictions for wire bonds at high temperatures. *Microelectronics Reliability*, forthcoming.

[2] Michael David Hook and Michael Mayer. Miniature environmental chambers for temperature humidity bias testing of microelectronics. *Review of Scientific Instruments*, 88(3):034707, 2017.

[3] George G Harman. *Wire Bonding in Microelectronics*. McGraw-Hill, 3 edition, 2010.

[4] Daniel Lu and CP Wong. *Materials for advanced packaging*, volume 181. Springer, 2009.

[5] Inductiveload. DIP cross-section, 2009. Public Domain. `file:///C:/Users/mdhook/Desktop/Dropbox/Thesis/Images/DIP_Cross-section.svg`; [accessed 24-July-2018].

[6] Nelson Wong. Presentation at 2nd Annual SEMI Vietnam Semiconductor Strategy Summit, September 2013.

[7] J. S. Cho, H. S. Jeong, J. T. Moon, S. J. Yoo, J. S. Seo, S. M. Lee, S. W. Ha, E. K. Her, S. H. Kang, and K. H. Oh. Thermal reliability & IMC behavior of low cost alternative Au-Ag-Pd wire bonds to Al metallization. In *2009 59th Electronic Components and Technology Conference*, pages 1569–1573, May 2009.

[8] H. Liu, Q. Chen, Z. Zhao, Q. Wang, J. Zeng, J. Chae, and J. Lee. Reliability of Au-Ag alloy wire bonding. In *2010 Proceedings 60th Electronic Components and Technology Conference (ECTC)*, pages 234–239, June 2010.

[9] Hao-Wen Hsueh, Fei-Yi Hung, Truan-Sheng Lui, and Li-Hui Chen. Microstructure, electric flame-off characteristics and tensile properties of silver bonding wires. *Microelectronics Reliability*, 51(12):2243, 2011.

[10] J. Wu, T. Rockey, O. Yauw, L. Shen, and B. Chylak. Study of Ag-alloy wire in thermosonic wire bonding. In *2012 IEEE 14th Electronics Packaging Technology Conference (EPTC)*, pages 499–503, Dec 2012.

[11] C. Lu. Review on silver wire bonding. In *Microsystems, Packaging, Assembly and Circuits Technology Conference (IMPACT), 2013 8th International*, page 226, Oct 2013.

[12] R. Guo, C. Yin, D. Mao, M. Li, Z. Lv, and H. Chiu. Thermal reliability of Ag-8Au-3Pd alloy wire bonds. In *CPMT Symposium Japan (ICSJ), 2013 IEEE 3rd*, page 1, Nov 2013.

[13] C.H. Cheng, H.L. Hsiao, S.I. Chu, Y.Y. Shieh, C.Y. Sun, and C. Peng. Low cost silver alloy wire bonding with excellent reliability performance. In *Electronic Components and Technology Conference (ECTC), 2013 IEEE 63rd*, page 1569, May 2013.

[14] H. H. Tsai, T. H. Chuang, J. D. Lee, C. H. Tsai, H. C. Wang, H. J. Lin, and C. C. Chang. High performance Ag-Pd alloy wires for high frequency IC packages. In *Microsystems, Packaging, Assembly and Circuits Technology Conference (IMPACT), 2013 8th International*, page 162, Oct 2013.

[15] A. Lan, J. Tsai, J. Huang, and O. Hung. Interconnection challenge of wire bonding - Ag alloy wire. In *2013 IEEE 15th Electronics Packaging Technology Conference (EPTC 2013)*, pages 504–509, Dec 2013.

[16] J. Tsai, A. Lan, D. S. Jiang, L. W. Wu, J. Huang, and J. B. Hong. Ag alloy wire characteristic and benefits. In *Electronic Components and Technology Conference (ECTC), 2014 IEEE 64th*, page 1533, May 2014.

[17] Y. C. Jang, S. Y. Park, H. D. Kim, Y. C. Ko, K. W. Koo, M. R. Choi, H. G. Kim, N. K. Cho, I. T. Kang, J. H. Yee, and S. H. Lim. Study of intermetallic compound growth and failure mechanisms in long term reliability of silver bonding wire. In *2014 IEEE 16th Electronics Packaging Technology Conference (EPTC)*, pages 704–708, Dec 2014.

[18] J. Xi, N. Mendoza, K. Chen, T. Yang, E. Reyes, S. Bezuk, J. Lin, S. Ke, and E. Chen. Evaluation of ag wire reliability on fine pitch wire bonding. In *2015 IEEE 65th Electronic Components and Technology Conference (ECTC)*, pages 1392–1395, May 2015.

[19] Yi-Wei Tseng, Fei-Yi Hung, Truan-Sheng Lui, Mei-Yu Chen, and Hao-Wen Hsueh. Effect of annealing on the microstructure and bonding interface properties of Ag-2Pd alloy wire. *Microelectronics Reliability*, 55(8):1256 – 1261, 2015.

[20] C. H. Tsai, C. H. Chuang, H. H. Tsai, J. D. Lee, D. Chang, H. J. Lin, and T. H. Chuang. Materials characteristics of ag-alloy wires and their applications in advanced packages. *IEEE Transactions on Components, Packaging and Manufacturing Technology*, 6(2):298–305, Feb 2016.

[21] S. Tanna, J.L. Pisigan, W. H. Song, C. Halmo, J. Persic, and M. Mayer. Low cost Pd coated Ag bonding wire for high quality FAB in air. In *Electron. Components and Technology Conference (ECTC), 2012 IEEE 62nd*, page 1103, 2012.

[22] Jimy Gomes. A Study on the Effect of Bond Stress and Process Temperature on Palladium Coated Silver Wire Bonds on Aluminum Metallization. Master's thesis, University of Waterloo, 2015.

[23] Di Erick Xu, Jimy Gomes, Michael Mayer, Rob Lyn, and John Persic. Thermal Aging Behavior of Fine Pitch Palladium Coated Silver (PCS) Ball Bonds on Al Metallization. *International Symposium on Microelectronics*, 2015(1):000298, 2015.

[24] Martin Schneider-Ramelow and Christian Ehrhardt. The reliability of wire bonding using Ag and Al. *Microelectronics Reliability*, 63:336 – 341, 2016.

[25] Salim L Khoury, David J Burkhard, David P Galloway, and Thomas A Scharr. A comparison of copper and gold wire bonding on integrated circuit devices. *IEEE transactions on components, hybrids, and manufacturing technology*, 13(4):673–681, 1990.

[26] Tan Chee Wei and Abdul Razak Daud. Mechanical and electrical properties of Au-Al and Cu-Al intermetallics layer at wire bonding interface. *Journal of Electronic Packaging*, 125(4):617, 2003.

[27] CL Gan and U Hashim. Reliability assessment and activation energy study of Au and Pd-coated Cu wires post high temperature aging in nanoscale semiconductor packaging. *Journal of electronic packaging*, 135(2):021010, 2013.

[28] Pradeep Lall, Shantanu Deshpande, and Luu Nguyen. Reliability of Copper, Gold, Silver, and PCC Wirebonds Subjected to Harsh Environment. In *Electronic Components and Technology Conference, 2018. ECTC 2018. 68th*, pages 724–734, 2018.

[29] Chong Leong Gan, Classe Francis, Bak Lee Chan, and Uda Hashim. Extended reliability of gold and copper ball bonds in microelectronic packaging. *Gold Bulletin*, 46(2):103–115, Jun 2013.

[30] CL Gan, TT Toong, CP Lim, and CY Ng. Environmental friendly package development by using copper wirebonding. In *Electronic Manufacturing Technology Symposium (IEMT), 2010 34th IEEE/CPMT International*, pages 1–5. IEEE, 2010.

[31] Hai Liu, Zhenqing Zhao, Qiang Chen, Jianwei Zhou, Maohua Du, Senyun Kim, Jonghyun Chae, and Myungkee Chung. Reliability of copper wire bonding in humidity environment. In *Electronics Packaging Technology Conference (EPTC), 2011 IEEE 13th*, pages 53–58. IEEE, 2011.

[32] C Glenn Shirley and Melissa Shell De Guzman. Moisture-induced gold ball bond degradation of polyimide-passivated devices in plastic packages. In *Reliability Physics Symposium, 1993. 31st Annual Proceedings., International*, pages 217–226. IEEE, 1993.

[33] Hidenori Abe, Dong Chul Kang, Takashi Yamamoto, Takashi Yagihashi, Yoshinori Endo, Hiroyuki Saito, Takahiro Horie, Hironori Tamate, Yoshinori Ejiri, Naoki Watanabe, et al. Cu wire and Pd-Cu wire package reliability and molding compounds. In *Electronic Components and Technology Conference (ECTC), 2012 IEEE 62nd*, pages 1117–1123. IEEE, 2012.

[34] F. C. Classe and S. Gaddamraja. Long term isothermal reliability of copper wire bonded to thin 6.5 µm aluminum. In *2011 International Reliability Physics Symposium*, pages CP.1.1–CP.1.5, April 2011.

[35] JEDEC Solid State Technology Association. High Temperature Storage Life, JESD22-A103C, 2004. JEDEC Solid State Technology Association, Arlington, VA.

[36] J. D. Beleran, N. Milanes, G. Mehta, N. Suthiwongsunthorn, R. Rajoo, and C. K. Chong. Enabling fine pitch Cu and Ag alloy wire bond assessment for 28nm ultra low-k structure. In *Electronic Components and Technology Conference (ECTC), 2014 IEEE 64th*, page 490, May 2014.

[37] Automotive Electronics Council Component Technical Committee. Failure mechanism based stress test qualification for integrated circuits, September 2014.

[38] Elaheh Arjmand, Pearl A. Agyakwa, Martin R. Corfield, Jianfeng Li, Bassem Mouawad, and C. Mark Johnson. A thermal cycling reliability study of ultrasonically bonded copper wires. *Microelectronics Reliability*, pages 126 – 133, 2016.

[39] JEDEC Solid State Technology Association. Temperature Cycling, JESD22-A104D, 2009. JEDEC Solid State Technology Association, Arlington, VA.

[40] P. Su, H. Seki, C. Ping, S. i. Zenbutsu, S. Itoh, L. Huang, N. Liao, B. Liu, C. Chen, W. Tai, and A. Tseng. An evaluation of effects of molding compound properties on reliability of Cu wire components. In *Electronic Components and Technology Conference (ECTC), 2011 IEEE 61st*, page 363, May 2011.

[41] Richard K Ulrich and William D Brown. *Advanced electronic packaging*. Wiley Hoboken, NJ, 2006.

[42] Ying-Ta Chiu, Tzu-Hsing Chiang, Yin-Fa Chen, Ping-Feng Yang, Louie Huang, and Kwang-Lung Lin. The corrosion performance of Cu alloy wire bond on Al pad in molding compounds of various chlorine contents under biased-HAST. In *Electronic Components and Technology Conference (ECTC), 2014 IEEE 64th*, pages 419–424. IEEE, 2014.

[43] Tomohiro Uno. Bond reliability under humid environment for coated copper wire and bare copper wire. *Microelectronics Reliability*, 51(1):148, 2011. Copper Wire Bonding.

[44] L. J. Kai, L. Y. Hung, L. W. Wu, M. Y. Chiang, D. S. Jiang, C. M. Huang, and Y. P. Wang. Silver alloy wire bonding. In *Electronic Components and Technology Conference (ECTC), 2012 IEEE 62nd*, page 1163, May 2012.

[45] C. L. Gan and U. Hashim. Influence of shear strength on long term biased humidity reliability of cu ball bonds. *Journal of Materials Science: Materials in Electronics*, 25(11):4786–4792, Nov 2014.

[46] JEDEC Solid State Technology Association. Steady State Temperature Humidity Bias Life Test, JESD22-A101C, 2009. JEDEC Solid State Technology Association, Arlington, VA.

[47] JEDEC Solid State Technology Association. Highly-Accelerated Temperature and Humidity Stress Test (HAST), JESD22-A110-B, 1999. Electronic Industries Alliance, Arlington, VA.

[48] M. Mayer. Non-destructive monitoring of Au ball bond stress during high-temperature aging. In *Electronic Components and Technology Conference, 2008. ECTC 2008. 58th*, page 1762, 2008.

[49] M. Mayer, J.T. Moon, and J. Persic. Measuring stress next to Au ball bond during high temperature aging. *Microelectronics Reliability*, 49(7):771, 2009.

[50] *Low Level Measurements Handbook*. Keithley Instruments, Inc., 7th edition, 2014.

[51] A. Laor, P. J. Herrell, and M. Mayer. A Study on Measuring Contact Resistance of Ball Bonds on Thin Metallization. *IEEE Transactions on Components, Packaging and Manufacturing Technology*, 5(5):704, May 2015.

[52] D. Olsen and K. James. Effects of ambient atmosphere on aluminum - copper wirebond reliability. *IEEE Transactions on Components, Hybrids, and Manufacturing Technology*, 7(4):357–362, Dec 1984.

[53] L. England and T. Jiang. Reliability of Cu wire bonding to Al metallization. In *2007 Proceedings 57th Electronic Components and Technology Conference*, pages 1604–1613, May 2007.

[54] Chong Leong Gan, Francis Classe, and Uda Hashim. Superior performance and reliability of copper wire ball bonding in laminate substrate based ball grid array. *Microelectronics International*, 30(3):169–175, 2013.

[55] R. Pelzer, M. Nelhiebel, R. Zink, S. Whlert, A. Lassnig, and G. Khatibi. High temperature storage reliability investigation of the alcu wire bond interface. *Microelectronics Reliability*, 52(9):1966 – 1970, 2012. SPECIAL ISSUE 23rd EUROPEAN SYMPOSIUM ON THE RELIABILITY OF ELECTRON DEVICES, FAILURE PHYSICS AND ANALYSIS.

[56] T. Boettcher, M. Rother, S. Liedtke, M. Ullrich, M. Bollmann, A. Pinkernelle, D. Gruber, H.-J. Funke, M. Kaiser, Kan Lee, M. Li, K. Leung, T. Li, M.L. Farrugia, O. O'Halloran, M. Petzold, B. März, and R. Klengel. On the intermetallic corrosion of Cu-Al wire bonds. In *Electronics Packaging Technology Conference (EPTC), 2010 12th*, page 585, Dec 2010.

[57] M. v. Soestbergen, A. Mavinkurve, J. J. M. Zaal, G. M. OHalloran, R. T. H. Rongen, and M. L. Farrugia. Crevice corrosion of ball bond intermetallics of Cu and Ag wire. In *2016 IEEE 66th Electronic Components and Technology Conference (ECTC)*, pages 774–781, May 2016.

[58] C. L. Gan, C. Francis, B. L. Chan, E. K. Ng, and U. Hashim. Effects of wire type and mold compound on wearout reliability of semiconductor flash fineline bga package. In *2013 8th International Microsystems, Packaging, Assembly and Circuits Technology Conference (IMPACT)*, pages 144–148, Oct 2013.

[59] Wentao Qin, Tom Anderson, Denise Barrientos, Harold Anderson, and George Chang. Corrosion Mechanisms of Cu Wire Bonding on Al Pads. In *Electronic Components and Technology Conference, 2018. ECTC 2018. 68th*, pages 1446–1454, 2018.

[60] C. Gan, E. Ng, B. Chan, T. Kwuanjai, S. Jakarin, and U. Hashim. Wearout reliability study of Cu and Au wires used in flash memory fine line BGA package. In *2012 7th International Microsystems, Packaging, Assembly and Circuits Technology Conference (IMPACT)*, pages 232–235, Oct 2012.

[61] Gan Chong Leong and Hashim Uda. Comparative reliability studies and analysis of au, pd-coated cu and pd-doped cu wire in microelectronics packaging. *PLOS ONE*, 8(11):1–8, 11 2013.

[62] R. Rongen, G. M. O'Halloran, A. Mavinkurve, L. Goumans, and M. L. Farrugia. Lifetime prediction of Cu-Al wire bonded contacts for different mould compounds. In *2014 IEEE 64th Electronic Components and Technology Conference (ECTC)*, pages 411–418, May 2014.

[63] M. Mishler, V. Ouvarov-Bancalero, Seung H. Chae, Luu Nguyen, and Choong-Un Kim. Intermetallic compound growth and stress development in Al-Cu diffusion couple. *Journal of Electronic Materials*, 47, January 2018.

[64] M. Han, M. Wang, L. Zhang, B. Yan, J. Li, M. Song, and V. Mathew. Copper wire bond pad/IMC interfacial layer crack study during HTSL (high temperature storage life) test. In *2016 IEEE 18th Electronics Packaging Technology Conference (EPTC)*, pages 797–800, Nov 2016.

[65] C.J. Hang, C.Q. Wang, M. Mayer, Y.H. Tian, Y. Zhou, and H.H. Wang. Growth behavior of Cu/Al intermetallic compounds and cracks in copper ball bonds during isothermal aging. *Microelectronics Reliability*, 48(3):416 – 424, 2008.

[66] C. C. Lee, V. Mathew, T. Tran, R. Ibrahim, and P. L. Eu. Copper ball voids for Pd-Cu wires: Affecting factors and methods of controlling. In *2016 IEEE 66th Electronic Components and Technology Conference (ECTC)*, pages 606–613, May 2016.

[67] P. Lall, S. Deshpande, and L. Nguyen. Effect of emcs on the high current reliability of cu wirebonds operating in harsh environments. In *2017 16th IEEE Intersociety Conference on Thermal and Thermomechanical Phenomena in Electronic Systems (ITherm)*, pages 1315–1324, May 2017.

[68] S. Na, T. Hwang, J. Park, J. Kim, H. Yoo, and C. Lee. Characterization of intermetallic compound (IMC) growth in Cu wire ball bonding on Al pad metallization. In *2011 IEEE 61st Electronic Components and Technology Conference (ECTC)*, pages 1740–1745, May 2011.

[69] Jin Onuki, M. Koizumi, and I. Araki. Investigation of the reliability of copper ball bonds to aluminum electrodes. *IEEE Transactions on Components, Hybrids, and Manufacturing Technology*, 10(4):550–555, Dec 1987.

[70] Y. Y. Tan and F. K. Yong. Cu-Al IMC micro structure study in Cu wire bonding with TEM. In *2010 17th IEEE International Symposium on the Physical and Failure Analysis of Integrated Circuits*, pages 1–4, July 2010.

[71] Michael McCracken, M. Mayer, Isaac Jourard, Jeong-Tak Moon, and J. Persic. Symmetric miniaturized heating system for active microelectronic devices. *Review of Scientific Instruments*, 81(7):075112, 2010.

[72] M. Mayer and J. Gomes. Accelerating reliability assessment with multi-oven racks and sensor chips for wire bonds. Presented at IMAPS New England Symposium, May 2015.

[73] Douglas C Montgomery. *Design and analysis of experiments*. John wiley & sons, 2017.

[74] Ezequiel Uriel Jimnez. *Introduction to Econometrics*. University of Valencia, 2013.

[75] Jerald F. Lawless. *Statistical Models and Methods for Lifetime Data*. John Wiley & Sons, Inc., 2 edition, 2011.

[76] Leonidas Bantis. Accelerated failure time (AFT) models, 2012.

[77] Wayne B Nelson. *Accelerated testing: statistical models, test plans, and data analysis*, volume 344. John Wiley & Sons, 1990.

[78] W.Q. Meeker and L.A. Escobar. *Statistical Methods for Reliability Data*. Wiley Series in Probability and Statistics. Wiley, 1998.

[79] J. Gomes and M. Mayer. Effect of Au ball bond geometry on bond strength and process parameters, and assessing reliability on Al bond pad using integrated stress sensors. In *2015 IEEE 65th Electronic Components and Technology Conference (ECTC)*, page 2127, May 2015.

[80] ASTM Standard D5032 - 11. Standard Practice for Maintaining Constant Relative Humidity by Means of Aqueous Glycerin Solutions, 2011. ASTM International, West Conshohocken, PA.

[81] Wikimedia Commons. Ball-and-stick model of glycerol, 2007. `https://en.wikipedia.org/wiki/Glycerol#/media/File:Glycerol-3D-balls.png`; [accessed 18-March-2016].

[82] G. R. Ross and W. J. Heideger. Vapor Pressure of Glycerol. *Journal of Chemical & Engineering Data*, 7(4):505, 1962.

[83] NS Osborne and CH Meyers. A formula and tables for the pressure of saturated water vapor in the range 0 to 374 C. *United States Bureau of Standards, Journal of Research*, 13:1, 1934.

[84] Jeffrey Kovac. Molecular size and Raoult's Law. *Journal of Chemical Education*, 62(12):1090, 1985.

[85] B. Lutz, Z. Guan, L. Wang, F. Zhang, and Z. L. Water absorption and water vapor permeation characteristics of HTV silicone rubber material. In *Electrical Insulation (ISEI), Conference Record of the 2012 IEEE International Symposium on*, page 478, June 2012.

[86] W. L. Robb. Thin silicone membranes-their permeation properties and some applications. *Annals of the New York Academy of Sciences*, 146(1):119, 1968.

[87] Stephen J. Blundell and Katherine M. Blundell. *Concepts in thermal physics*. Oxford University Press, 1 edition, 2006.

[88] P.W. Atkins. *Physical Chemistry*. Oxford University Press, 1990.

[89] M. Mayer, D. E. Xu, and K. Ratcliffe. The electrical reliability of silver wire bonds under high temperature storage. In *2016 IEEE 66th Electronic Components and Technology Conference (ECTC)*, page 654, May 2016.

[90] Di Erick Xu, Michael David Hook, and Michael Mayer. Real time joint resistance monitoring during solder reflow. *Journal of Alloys and Compounds*, 695:3002 – 3010, 2017.

[91] *ASM Handbook*, volume 3. ASM International, 2016.

[92] J. Gomes, M. Mayer, and B. Lin. Development of a fast method for optimization of Au ball bond process. *Microelectronics Reliability*, 55(3-4):602, 2015.

[93] H. Gaul, M. Schneider-Ramelow, and H. Reichl. Analytic model verification of the interfacial friction power in Al US w/w bonding on Au pads. *IEEE Transactions on Components and Packaging Technologies*, 33(3):607–613, Sept 2010.

[94] Michael David Hook, Michael Mayer, and Stevan Hunter. High temperature storage reliability of bond resistance of palladium-coated copper ball bonds. *International Symposium on Microelectronics*, 2017(1):000432–000437, 2017.

[95] Michael Hook, Michael Mayer, and Stevan Hunter. Thermosonic ball bonding recipe optimization: Comparing Cu and PCC wire on two pad thicknesses. Presented at IMAPS 14th International Conference and Exhibition on Device Packaging, Fountain Hills, AZ, USA, March 2018.

[96] Michael Hook, Michael Mayer, and Stevan Hunter. Effects of epoxy molding compound on electrical resistance degradation of Pd-coated Cu wire bonds in the 175 to 225 °C range. In *Electronic Components and Technology Conference (ECTC), 2018 IEEE 68th*, 2018.

[97] Y.H. Tian, C.J. Hang, C.Q. Wang, G.Q. Ouyang, D.S. Yang, and J.P. Zhao. Reliability and failure analysis of fine copper wire bonds encapsulated with commercial epoxy molding compound. *Microelectronics Reliability*, 51(1):157 – 165, 2011. Copper Wire Bonding.

[98] M. Hook, S. Hunter, and M. Mayer. Resistance changes of pd-coated Cu and Ag bonding wires in high temperature storage. Presented at TMS 147th Annual Meeting and Exhibition, March 2018.

Appendix A

Additional Plots of Aging Data

A.1 Detailed Resistance Change Plots

This appendix presents comprehensive resistance change data, showing the resistance changes over time for individual wire bond pairs, which were not practical to display in Chapter 4.

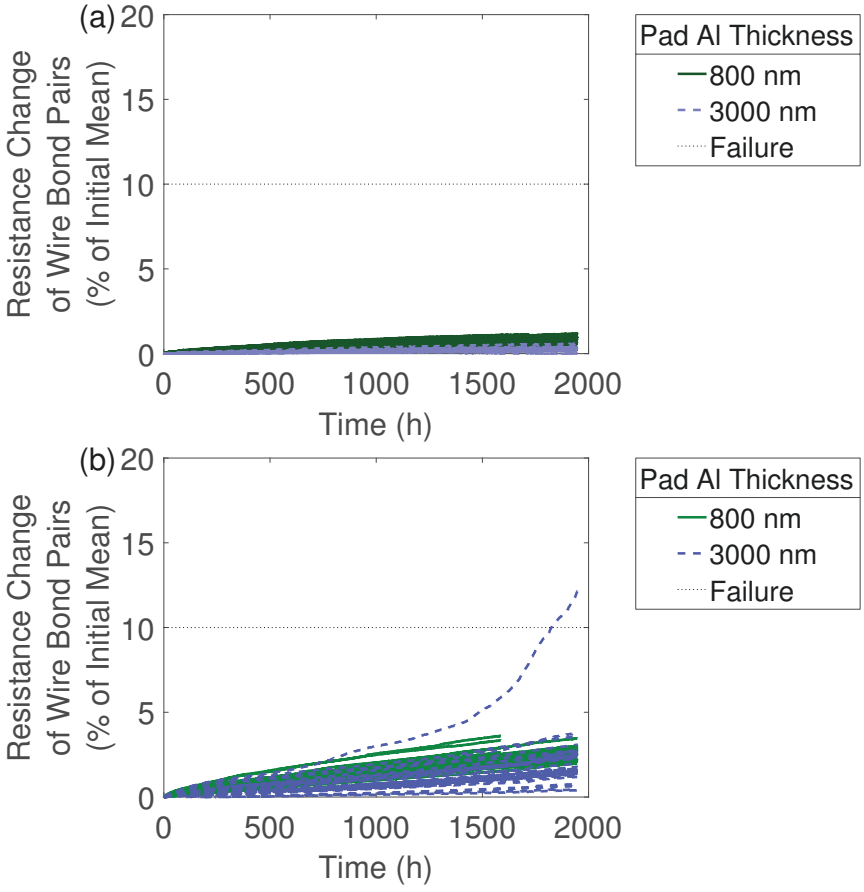

Fig. A.1: Normalized resistance changes over time for unencapsulated PCC bonds with full cleaning. (a) 175 °C. (b) 200 °C.

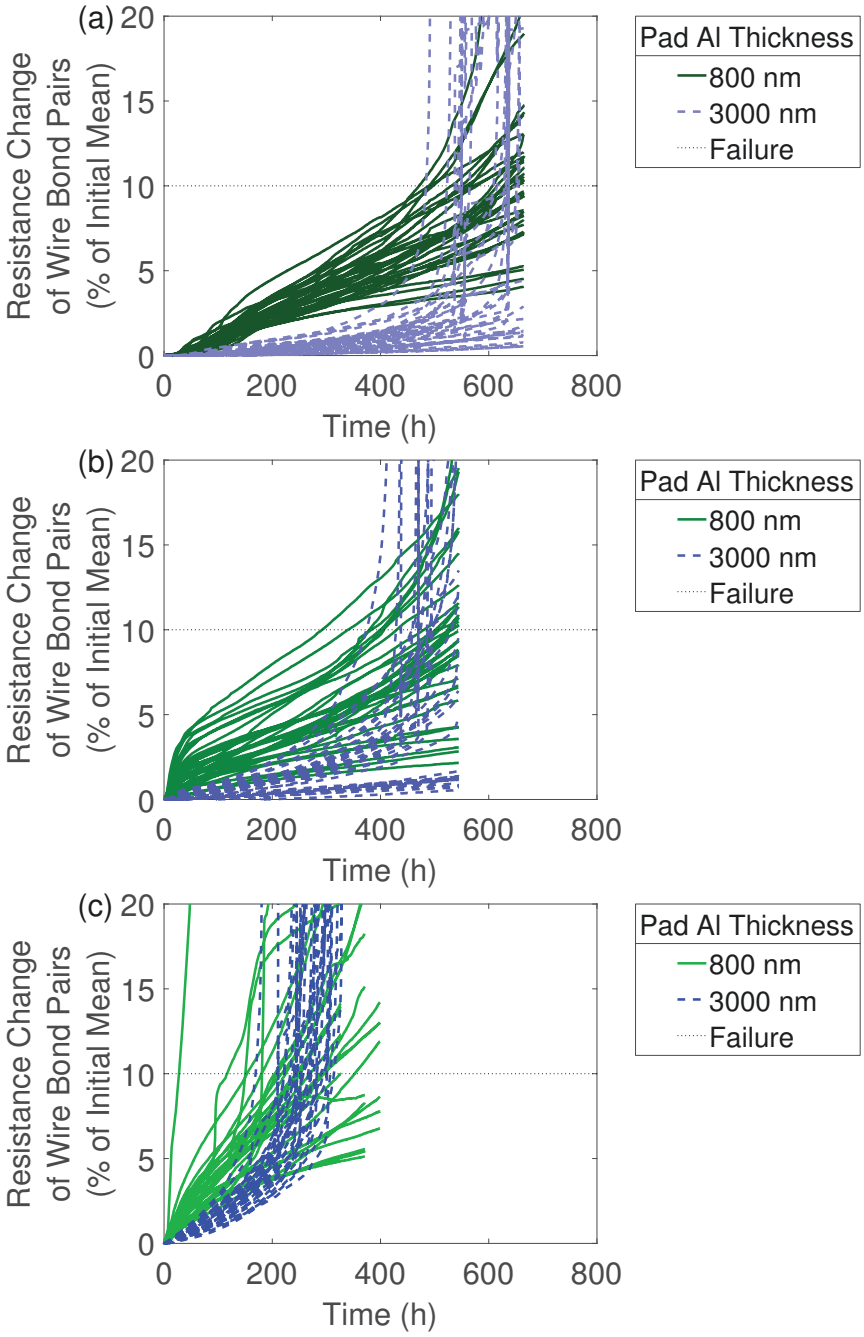

Fig. A.2: Normalized resistance changes over time for PCC bonds with Epoxy A and limited cleaning. Two bond pad thicknesses for each plot. (a) 175 °C. (b) 200 °C. (c) 225 °C.

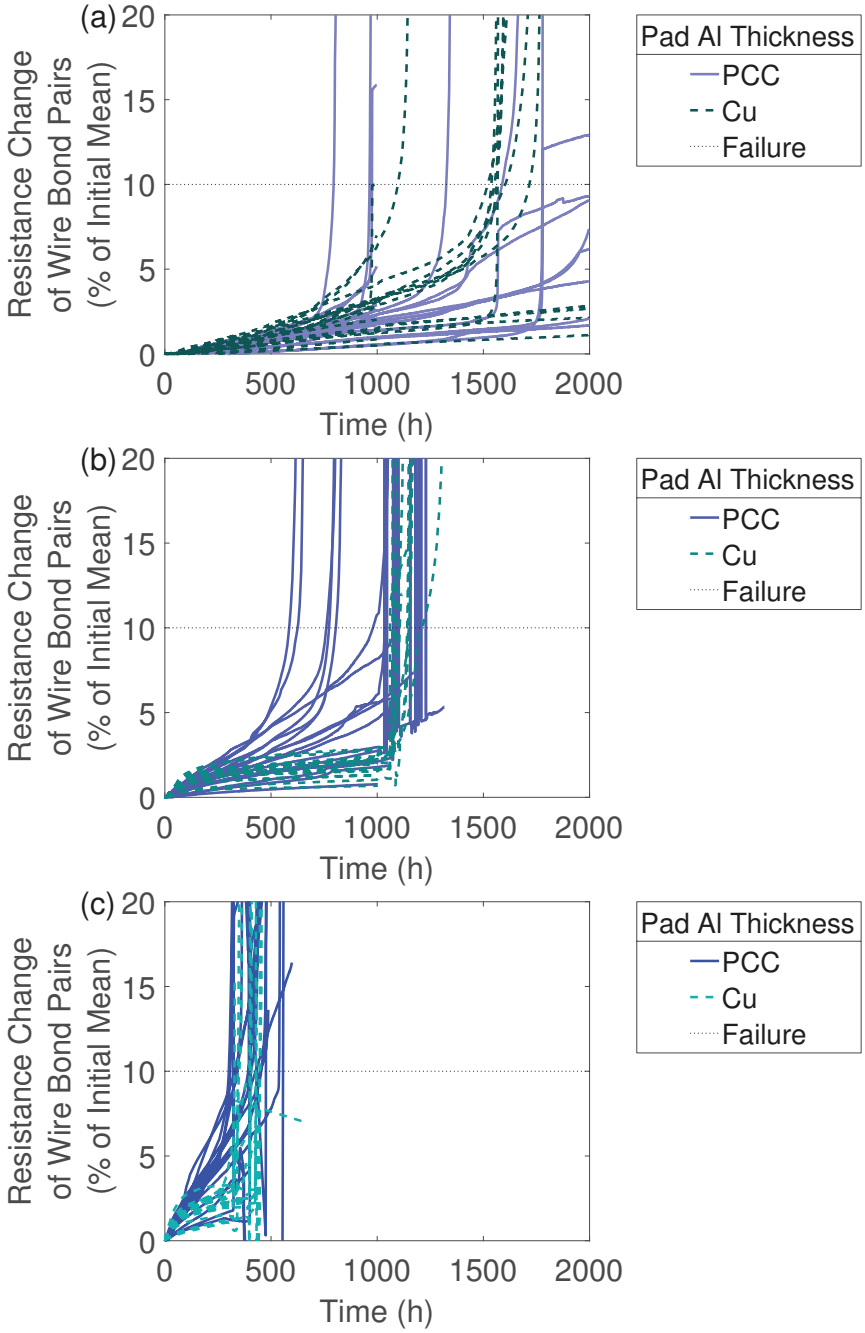

Fig. A.3: Normalized resistance changes over time for both wire types with Epoxy A and full cleaning. (a) 175 °C. (b) 200 °C. (c) 225 °C.

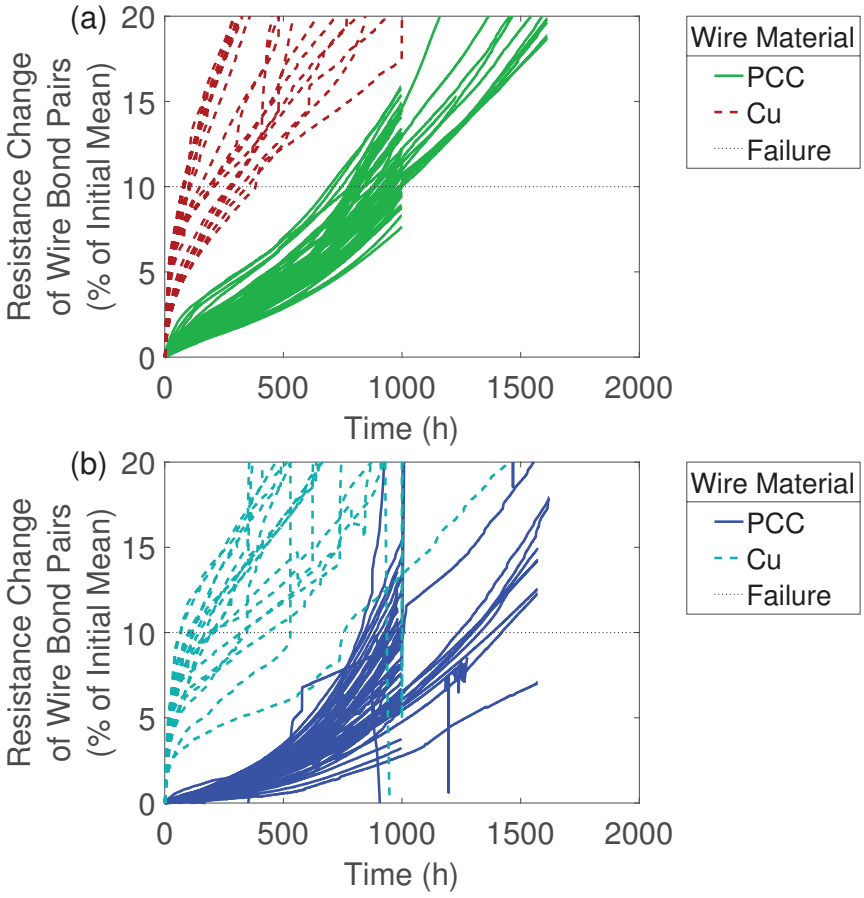

Fig. A.4: Normalized resistance changes over time for unencapsulated bonds at 225 °C with full cleaning. (a) 800 nm pad thickness. (b) 3000 nm pad thickness.

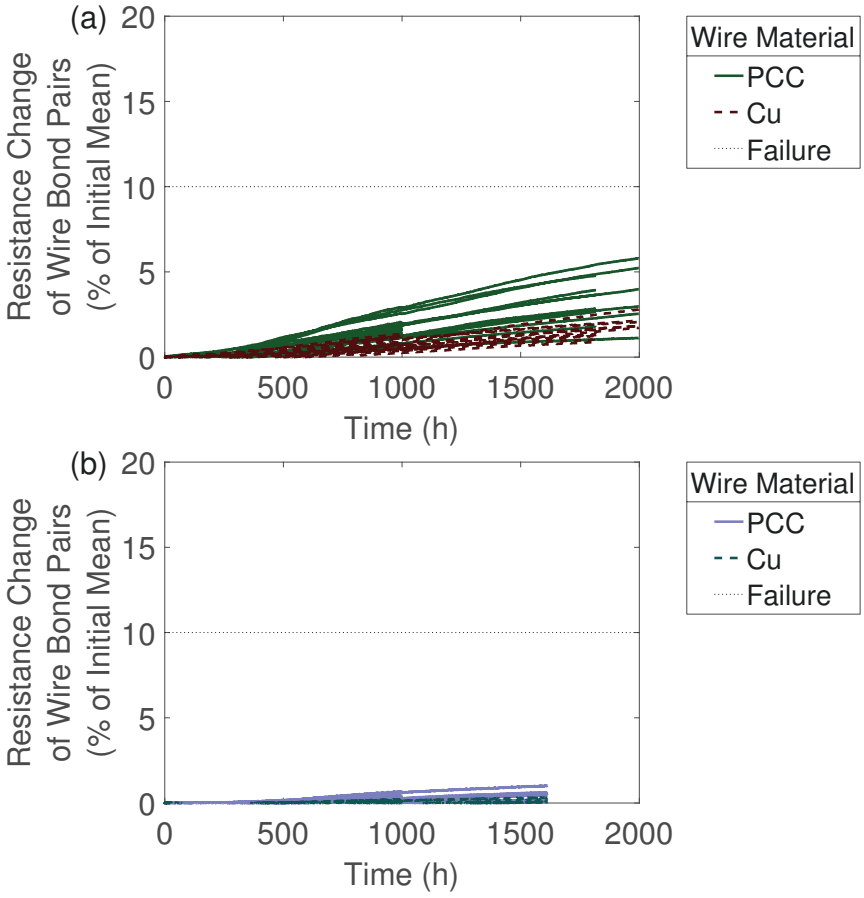

Fig. A.5: Normalized resistance changes over time for both wire types with Epoxy B and full cleaning, aged at 175 °C. (a) 800 nm pad thickness. (b) 3000 nm pad thickness.

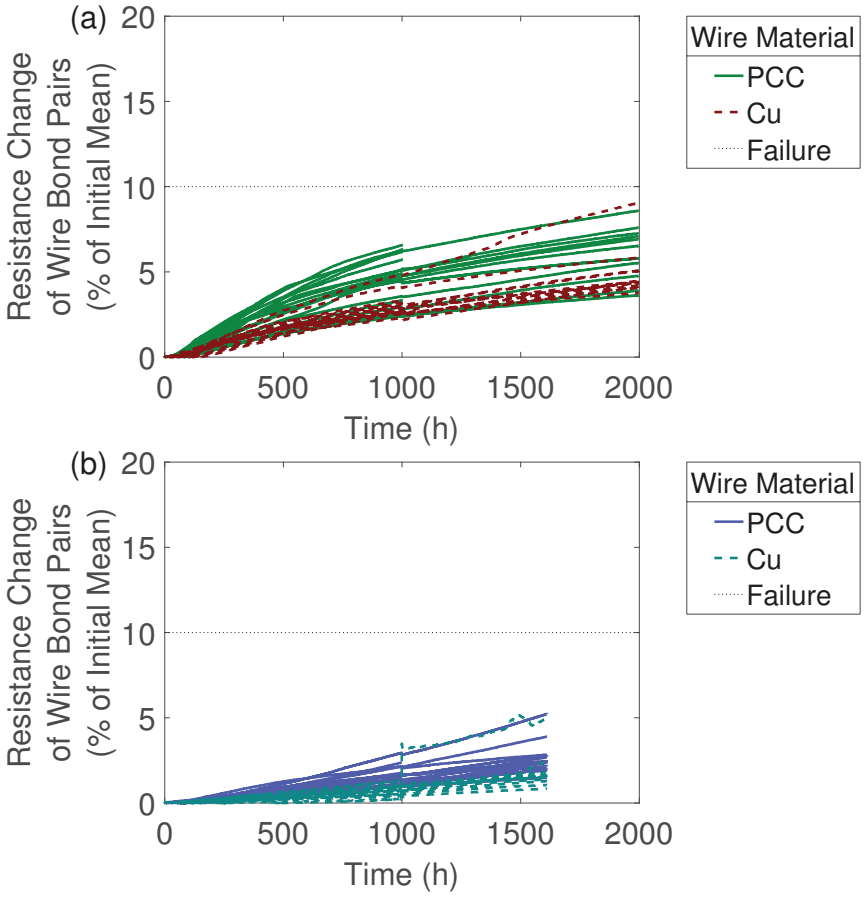

Fig. A.6: Normalized resistance changes over time for both wire types with Epoxy B and full cleaning, aged at 200 °C. (a) 800 nm pad thickness. (b) 3000 nm pad thickness.

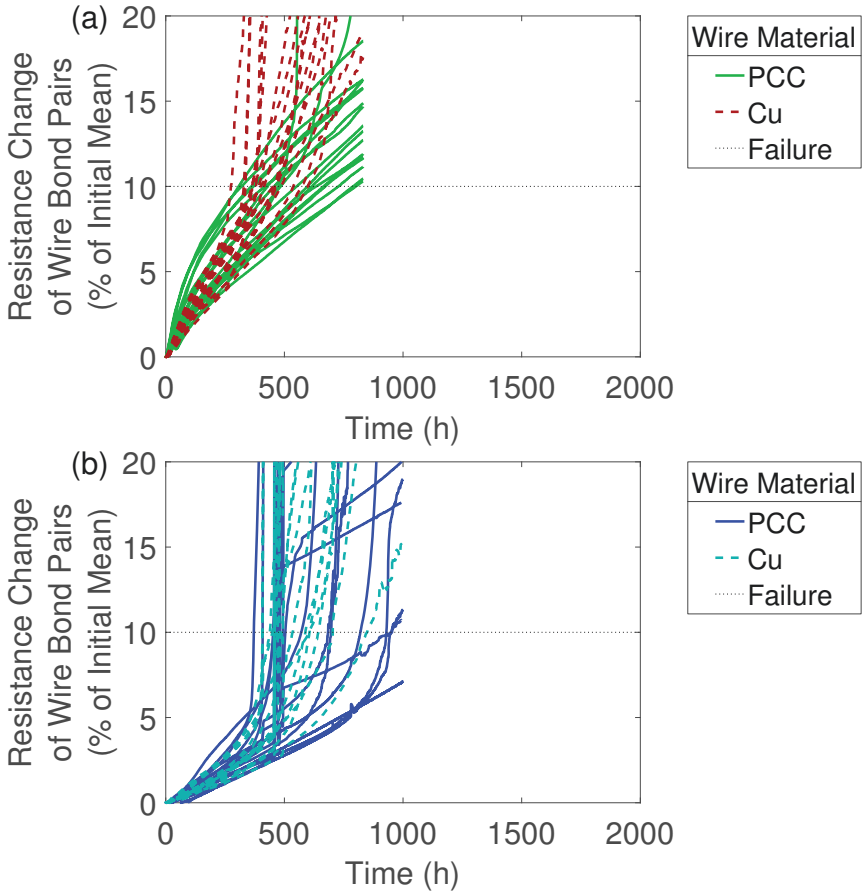

Fig. A.7: Normalized resistance changes over time for both wire types with Epoxy B and full cleaning, aged at 225 °C. Two bond pad thicknesses for each plot. (a) 800 nm pad thickness. (b) 3000 nm pad thickness.

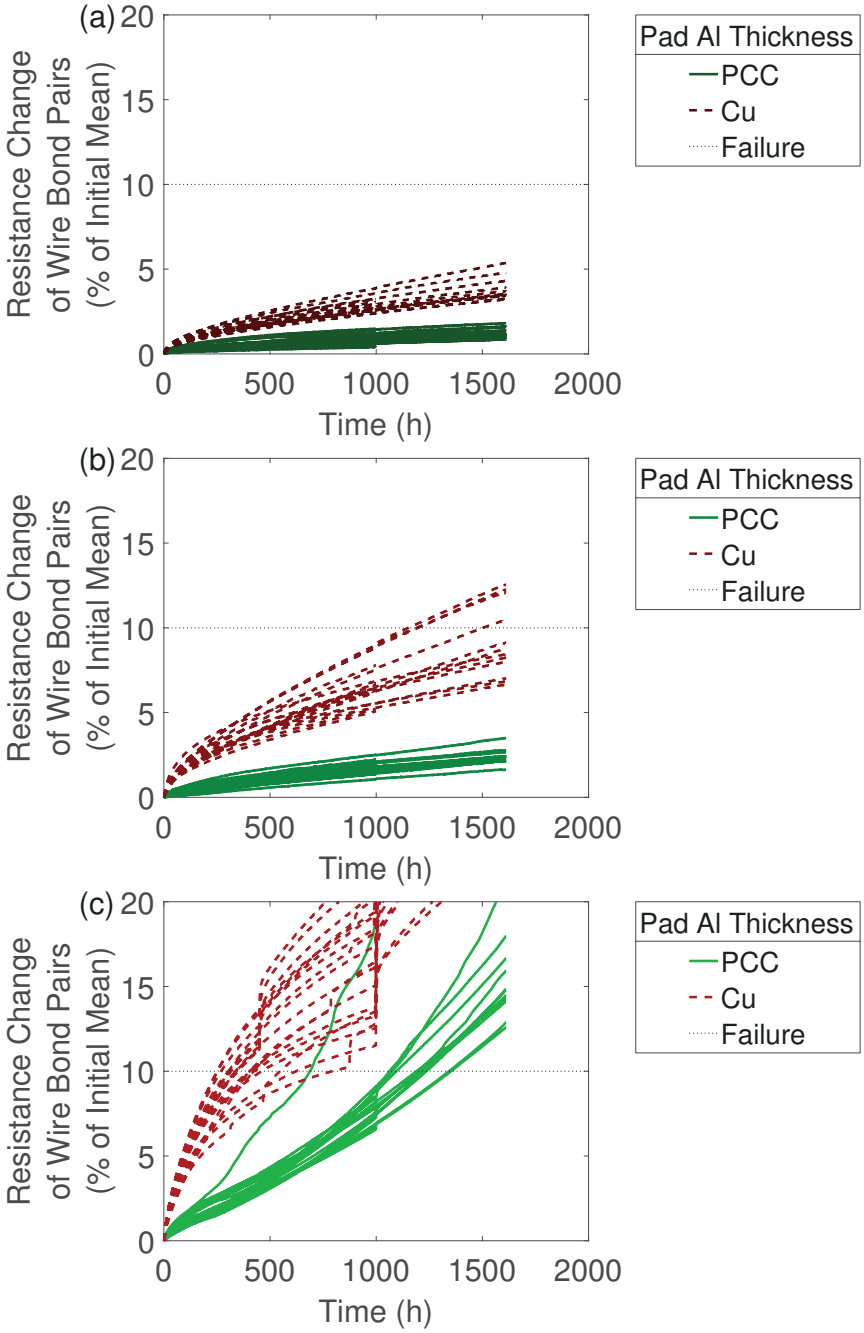

Fig. A.8: Normalized resistance changes over time for both wire types with silicone encapsulant and full cleaning on 800 nm thick pads. (a) 175 °C (b) 200 °C. (c) 225 °C.

A.2 Additional Fit Assessment Plots

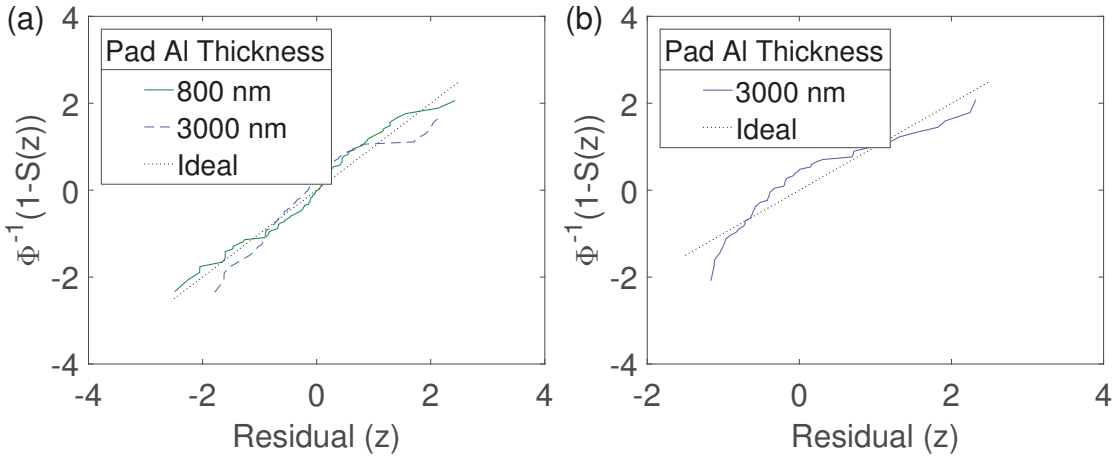

Fig. A.9: Fit assessment plots for PCC bonds with Epoxy A. (a) Limited cleaning. (b) Full cleaning.

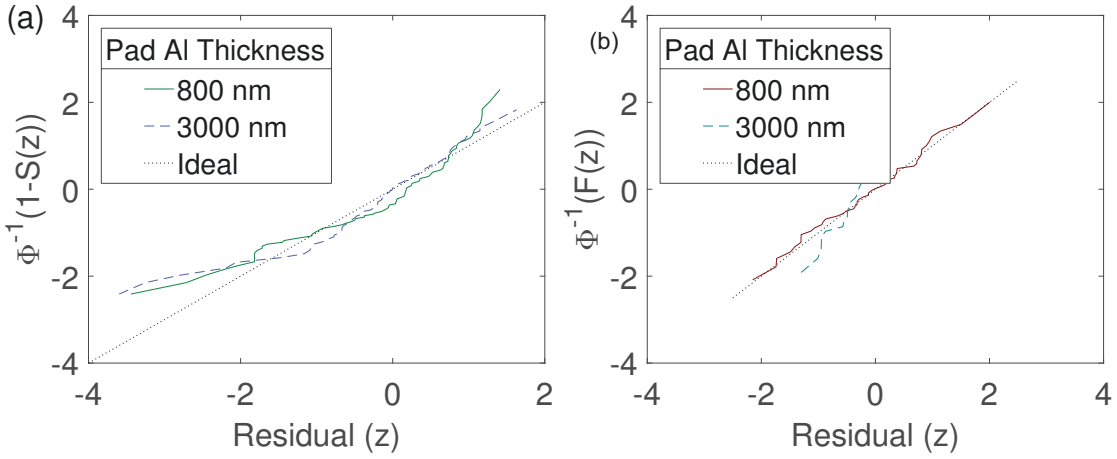

Fig. A.10: Fit assessment plots. (a) Unencapsulated PCC bonds, full cleaning. (b) Bare Cu bonds with Encapsulant B, full cleaning.

Appendix B

AutoCAD Drawings of Glycerol Cup and Cover

This appendix shows AutoCAD drawings that I submitted to the UW Engineering Machine Shop, who then produced twenty copies of each part using aluminum. All dimensions are measured in millimetres.

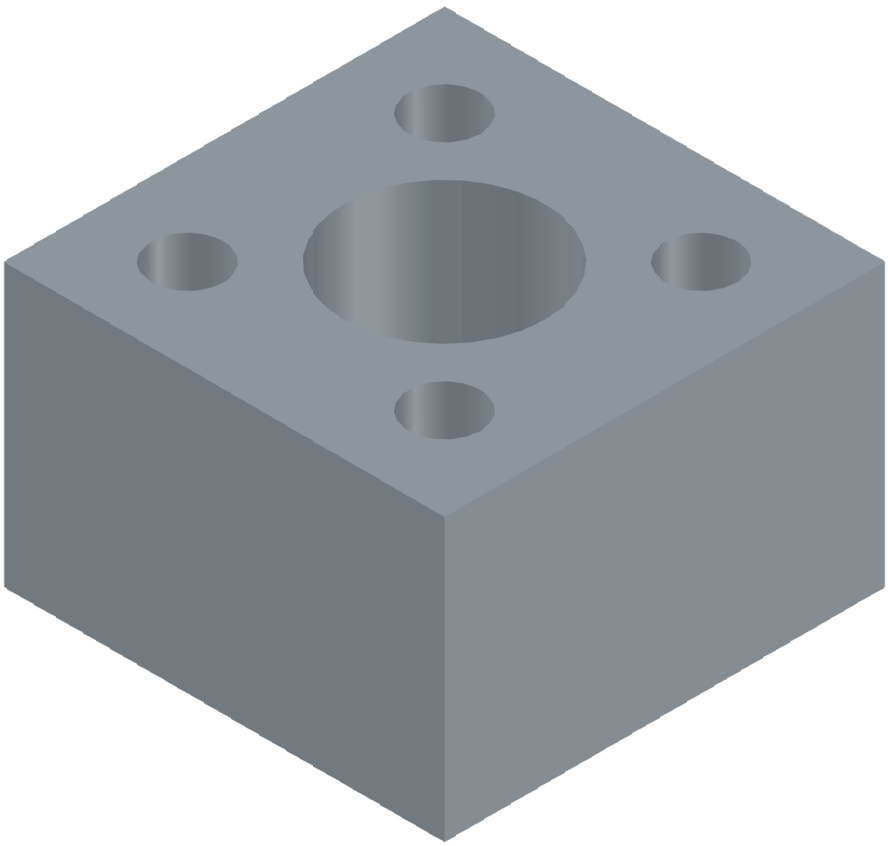

Fig. B.1: Angled view of glycerol cup. Central cavity holds glycerol solution, four peripheral holes fit #0-80 screws for clamping of silicone membrane.

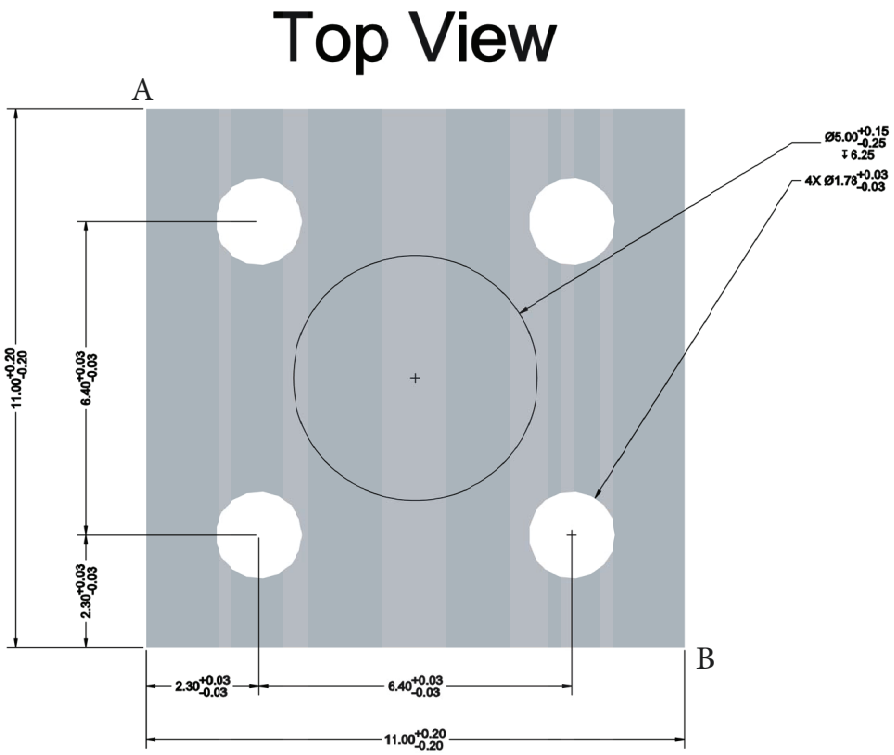

Fig. B.2: Top view of glycerol cup. Points A and B refer to corresponding locations in Fig. B.4

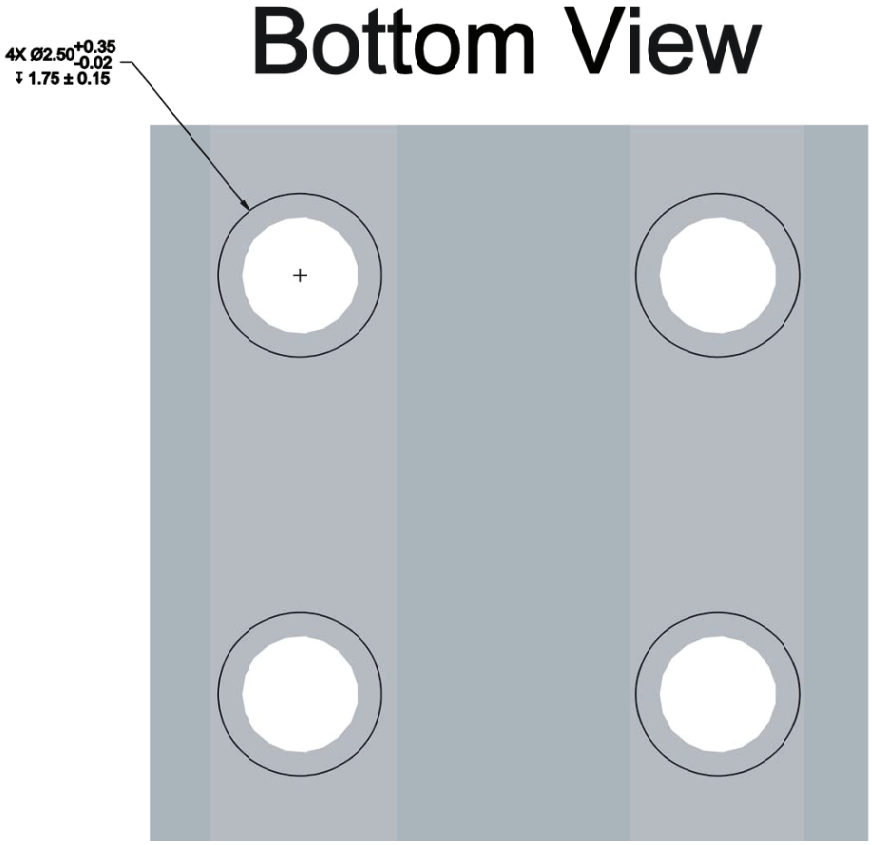

Fig. B.3: Bottom view of glycerol cup. Counterbores allow screw heads to recess into part.

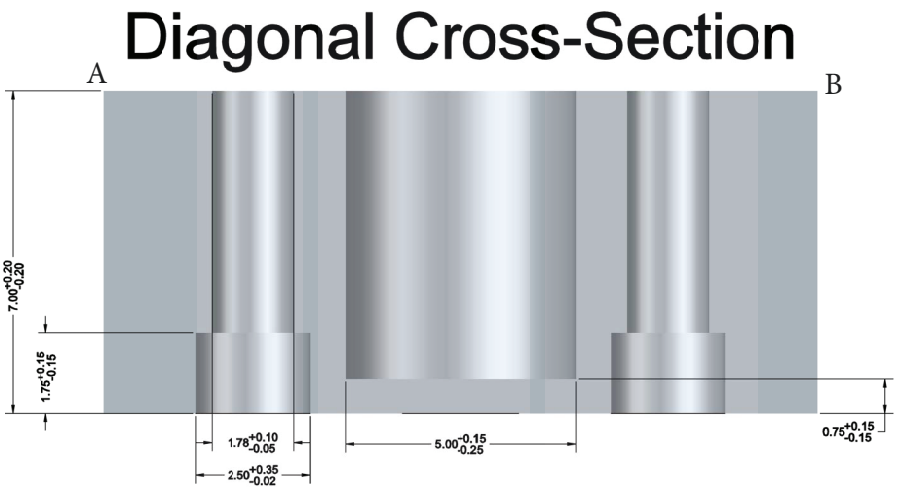

Fig. B.4: Cross-sectional view of glycerol cup. Points A and B refer to corresponding locations in Fig. B.2

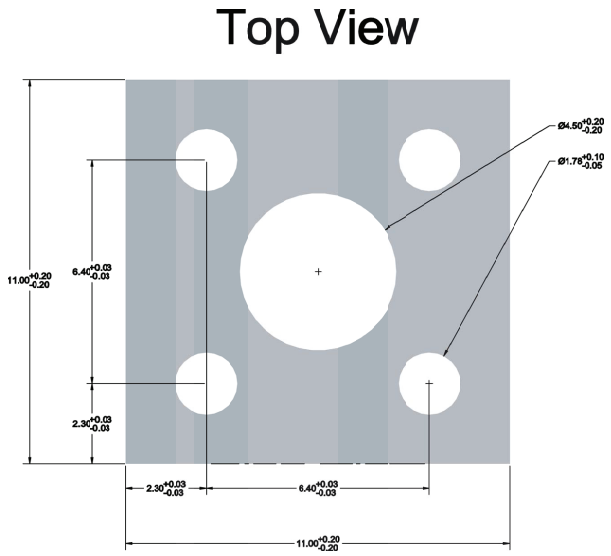

Fig. B.5: Top view of cover plate for glycerol cup.

Fig. B.6: Side view of cover plate for glycerol cup.

Appendix C

MATLAB Code

C.1 Simple Geometry Contour Plots File: DOE_Complete_Program.m

This code was created as part of [92] to generate contour plots of bonded ball geometry.

```
%2x2 DOE
n=2;
%DOE Points

IF=[];
disp('Insert IF values from lowest to highest');
for i=1:n;
    a=['IF',num2str(i),' = '];
    IF(i)=input(a);
end

t_EFO=[];
disp('Insert t_EFO values from lowest to highest');
for i=1:n;
    a=['t_EFO',num2str(i),' = '];
    t_EFO(i)=input(a);
end
```

```
BDC=[];
for i=1:n;
   for j=1:n;
       a=['BDC from IF ',num2str(IF(i)),' and t_EFO '...
    ,num2str(t_EFO(j)),' = '];
       BDC(j,i)=input(a);
   end
end

BH=[];
for i=1:n;
   for j=1:n;
       a=['BH from IF ',num2str(IF(i)),' and t_EFO '...
    ,num2str(t_EFO(j)),' = '];
       BH(j,i)=input(a);
   end
end

figure(1)
%Contour Plot

n1=50:1:90;               %contour lines for BDC
n2=[5:30];               %contour lines for BH

[hCont1,h1]=contour(IF,t_EFO,BDC,n1,'Linewidth',2,'Color','r',...
    'Linestyle',':');
hold on;
[hCont2,h2]=contour(IF,t_EFO,BH,n2,'Linewidth',2,'Color','b',...
    'Linestyle','--');
% legend('BDC','BH','location','northeastoutside');
legend('BDC','BH');
hXlabel=xlabel('IF [mN]');
hYlabel=ylabel('t_E_F_O [ms]');
set(gca,'FontName','Helvetica');
set([hXlabel, hYlabel],'FontName','AvantGarde');
set([hXlabel, hYlabel],'FontSize',12,'FontWeight','bold');
set(gca,'LineWidth',1.5,'FontSize',12);
set(gca,'box','on','LineWidth',1.5);
```

```
clabel(hCont1,'FontName','Helvetica','FontSize',12,'Color','r',...
    'FontWeight','bold');
clabel(hCont2,'FontName','Helvetica','FontSize',12,'Color','b',...
    'FontWeight','bold');
set(gcf,'color','w');

%DOE Location
for i=1:n
    for j=1:n
        plot(IF(i),t_EFO(j),'k*','markersize',12,'LineWidth',1.5);
    end
end
if n==3
    plot([IF(2),IF(2)],[t_EFO(1),t_EFO(3)],'-.','linewidth',1,...
    'color','k');
    plot([IF(1),IF(3)],[t_EFO(2),t_EFO(2)],'-.','linewidth',1,...
    'color','k');
end

%Optimized Parameter Calculation

%Target BDC and BH
a='Target BDC = ';
BDCtar=input(a);
a='Target BH = ';
BHtar=input(a);

hCont3=contourc(IF,t_EFO,BDC,[BDCtar BDCtar]);
hCont4=contourc(IF,t_EFO,BH,[BHtar BHtar]);
hCont3(:,1)=[];
hCont4(:,1)=[];
[IFopt,t_EFOopt]=...
    polyxpoly(hCont3(1,:),hCont3(2,:),hCont4(1,:),hCont4(2,:));
X=['Optimized IF = ',num2str(IFopt')];
disp(X);
X=['Optimized t_EFO = ',num2str(t_EFOopt')];
disp(X);
```

```
plot(IFopt,t_EFOopt,'gO','markersize',12,'LineWidth',1.5);
plot([IF(1),IFopt],[t_EFOopt,t_EFOopt],...
    '-','linewidth',1.5,'color','m');
plot([IFopt,IFopt],[t_EFOopt,t_EFO(1)],...
    '-','linewidth',1.5,'color','m');
```

C.2 Geometry Contour Plots with Confidence Regions File: AnalyzeGeometry.m

This code fits linear models for the geometry data from a 2×2 DOE as in Section 3.2.1, ten produces contour plots with confidence regions for the optimal IF and I_{EFO} values.

```
%Target values for diameter, height
targetBDC = 61;
targetBH = 14;

%Set to desired confidence level (%)
conf = 95;
alpha = (100 - conf)/100;

%% Machine settings
%Columns: constant,  I_EFO,         IF,      I_EFO*IF
X =         [1        65.06         500        32530
             1        65.06        1000        65060
             1         54.9         500        27450
             1         54.9        1000        54900
             1         54.9        1000        54900
             1        65.06        1000        65060
             1         54.9         500        27450
             1        65.06         500        32530
             1        65.06         500        32530
             1        65.06        1000        65060
             1         54.9        1000        54900
             1         54.9         500        27450
             1        65.06         500        32530
             1         54.9         500        27450
             1         54.9        1000        54900
             1        65.06        1000        65060
             1        65.06         500        32530
             1        65.06        1000        65060
             1         54.9         500        27450
             1         54.9        1000        54900
             1         54.9        1000        54900
             1        65.06        1000        65060
```

```
            1         54.9          500        27450
            1        65.06          500        32530
            1        65.06          500        32530
            1        65.06         1000        65060
            1         54.9         1000        54900
            1         54.9          500        27450
            1        65.06          500        32530
            1         54.9          500        27450
            1         54.9         1000        54900
            1        65.06         1000        65060];

%% Diameter measurements
D = [54.27
61.815
54.195
60.47
60.465
62.44
53.115
54.51
55.305
62.825
60.585
52.83
54.58
53.755
61.055
63.815];

%% Height measurements
H = [25
18
16
12
10
19
14
24
```

```
25
18
11
15
25
15
10
19
25
18
16
11
9
19
15
25
22
19
9
16
25
16
11
17];

%% Model inputs
X_BDC = X(1:length(D), :);
n_BDC = size(X_BDC, 1);
p_BDC = size(X_BDC, 2);
y_BDC = D;

X_BH = X(1:length(H), :);
n_BH = size(X_BH, 1);
p_BH = size(X_BH, 2);
y_BH = H;

%% Calculations
%Calculate model coefficients
```

```
beta_BDC = inv(X_BDC'*X_BDC)*X_BDC'*y_BDC;
beta_BH = inv(X_BH'*X_BH)*X_BH'*y_BH;

%Calculate sigma
SSE_BDC = y_BDC'*y_BDC - beta_BDC'*X_BDC'*y_BDC;
sigma_BDC = sqrt(SSE_BDC / (n_BDC - p_BDC));

SSE_BH = y_BH'*y_BH - beta_BH'*X_BH'*y_BH;
sigma_BH = sqrt(SSE_BH / (n_BH - p_BH));

%Create search grid of IF, EFO values
gridNum = 1000;
IF = X(:,3);
I_EFO = X(:,2);
IFEval = linspace(min(IF), max(IF), gridNum);
EFOEval = linspace(min(I_EFO), max(I_EFO), gridNum);
[IFMatrix, EFOMatrix] = meshgrid(IFEval, EFOEval);
IFVec = IFMatrix(:);
EFOVec = EFOMatrix(:);

%Calculate prediction intervals for diameter, height
x = [ones(size(EFOVec)) EFOVec IFVec EFOVec.*IFVec]';
BDC_Pred = x' * beta_BDC;
BDC_SE = sqrt(sigma_BDC^2 * sum(x .* (inv(X' * X) * x)))';
BDC_RespDev = sqrt(sigma_BDC^2 * (1+sum(x .* (inv(X' * X) * x))))';

BH_Pred = x' * beta_BH;
BH_SE = sqrt(sigma_BH^2 * sum(x .* (inv(X_BH' * X_BH) * x)))';
BH_RespDev = sqrt(sigma_BH^2 * (1+sum(x .* (inv(X_BH' * X_BH) * x))))';

%Calculate confidence regions for optimal parameters
chiSquared = ((BDC_Pred - targetBDC)./BDC_SE).^2 +...
 ((BH_Pred - targetBH)./BH_SE).^2;
reject = chi2cdf(chiSquared, 2) > conf/100;

%Find optimal parameters
totalAbsError = abs(BDC_Pred - targetBDC) + abs(BH_Pred - targetBH);
[minAbsError, optIndex] = min(totalAbsError);
```

```
optIF = IFVec(optIndex);
optEFO = EFOVec(optIndex);

%% Output
figure;
hold on;

%Output IF, I_EFO results
disp('Recommended machine parameters:');
disp(['IF: ' num2str(optIF, '%0.0f') ' mN']);
disp(['I_EFO: ' num2str(optEFO, '%0.2f') ' mA']);

%Plot confidence regions
contour(IFMatrix, EFOMatrix, reshape(~reject, gridNum, gridNum),...
 [0.5 0.5]);
xlabel('Impact Force (mN)');
ylabel('EFO Current (mA)');

%Mark intersection points
xlim = get(gca, 'xlim');
ylim = get(gca, 'ylim');
plot(optIF, optEFO, 'xg');
plot([optIF optIF], [ylim(1) optEFO], 'g-');
plot([xlim(1) optIF], [optEFO optEFO], 'g');

%Plot BDC and BH contours
[c, h] = contour(IFMatrix, EFOMatrix, ...
    reshape(BDC_Pred, gridNum, gridNum), 50:80);
clabel(c, h);
[c, h] = contour(IFMatrix, EFOMatrix, ...
    reshape(BH_Pred, gridNum, gridNum), 5:30);
clabel(c, h);
plottedGeom = true;
xlabel('Impact Force (mN)');
ylabel('EFO Current (mA)');
plot(IF, I_EFO, 'ko');
```

C.3 C_{pk} Plots File: CpkPlot.m

This code produces plots of C_{pk} as in Fig. 3.13. AnalyzeGeometry should be run first to calculate σ for BDC and BH..

```
%sigma calculated from AnalyzeGeometry.m
sigma_BDC = 0.5832;
sigma_BH = 0.91856;

%input target values
targetBDC = 54:0.1:63;
targetBH = 11:0.1:22;

%input tolerances (fractions of targets)
BDCTol = 0.05;
BHTol = 0.25;

%calculate specification limits
LSL_BDC = targetBDC - targetBDC*BDCTol;
USL_BDC = targetBDC + targetBDC*BDCTol;
LSL_BH = targetBH - targetBH*BHTol;
USL_BH = targetBH + targetBH*BHTol;

%calculate cpk
cpk_BDC = zeros(length(targetBDC),length(targetBH));
cpk_BH = zeros(length(targetBDC),length(targetBH));

for i = 1:length(targetBDC)
    for j = 1:length(targetBH)
        cpk_BDC(i,j) = min((USL_BDC(i) - targetBDC(i))./(3*sigma_BDC),...
            (targetBDC(i) - LSL_BDC(i))./(3*sigma_BDC));
        cpk_BH(i,j) = min((USL_BH(j) - targetBH(j))./(3*sigma_BH),...
            (targetBH(j) - LSL_BH(j))./(3*sigma_BH));
    end
end
```

```
[x, y] = meshgrid(targetBH, targetBDC);

%plot results
%BDC
figure;
hold on;
[c, h] = contour(y, x, cpk_BDC, 1.5:0.05:1.8);
clabel(c, 'Rotation', 0);
xlabel('Target BDC (m)');
ylabel('Target BH (m)');

%BH
figure;
hold on;
[c, h] = contour(y, x, cpk_BH, 1:0.1:2);
clabel(c, 'Rotation', 0);
xlabel('Target BDC (m)');
ylabel('Target BH (m)');

%Combined (minimum of cpk values for BDC and BH)
figure;
hold on;
[c, h] = contour(y, x, min(cpk_BDC, cpk_BH), 1:0.1:2);
clabel(c, 'Rotation', 0);
xlabel('Target BDC (m)');
ylabel('Target BH (m)');
```

C.4 Kaplan-Meier Aging Summary Plots File:KMPlot.m

This code, using PCC bonds with 832HT epoxy as an example, creates summary plots based on a Kaplan-Meier estimate, such as Fig. 4.11. The MATLAB structure DataStruct contains all the information about aging temperature, resistance data, failure times, etc. for each substrate.

```
%Plot customization
level = 0.1:0.1:20; % Range of resistance change % to plot
legendTitle = {'Pad Al Thickness,', 'Temperature'};
legendStr = {'800 nm, 175 C', '800 nm, 200 C', '800 nm, 225 C', ...
'3000 nm, 175 C', '3000 nm, 200 C', '3000 nm, 225 C'};
marker = {'-', '-', '-', '--', '--', '--'};
width = [2 2 2 2 2 2];

%Choose which samples to plot
thickness = [800 800 800 3000 3000 3000];
cleaned = [true true true true true true];
conditioned = [false false false false false false];
temp = [175 200 225 175 200 225];
encapsulant = {'832HT', '832HT', '832HT', '832HT', '832HT', '832HT'};
wire = {'PCC', 'PCC', 'PCC', 'PCC', 'PCC', 'PCC'};
BDC = {'all', 'all', 'all', 'all', 'all', 'all'};
bondType = {'Al', 'Al', 'Al', 'Al', 'Al', 'Al'};


figure;
hold on;

stdColours = ...
    [176,0,0;   0,176,0;    0,0,255;            0,176,176;
    135,0,0;    0,135,0;    73,73,255;          0,135,135;
    85,0,0;     0,85,0;     132,132,255;        0,85,85]/255;

for c = 1:length(thickness)

    %Assign colour to each line according to wire type, pad thickness,
    %and aging temperature
```

```
        colourStr = [wire{c} num2str(thickness(c)) num2str(temp(c))];

        switch colourStr
            case 'PCC800175',
                colourIndex = 10;
            case 'PCC800200',
                colourIndex = 6;
            case 'PCC800225',
                colourIndex = 2;
            case 'PCC3000175',
                colourIndex = 11;
            case 'PCC3000200',
                colourIndex = 7;
            case 'PCC3000225',
                colourIndex = 3;
            case 'Cu800175',
                colourIndex = 9;
            case 'Cu800200',
                colourIndex = 5;
            case 'Cu800225',
                colourIndex = 1;
            case 'Cu3000175',
                colourIndex = 12;
            case 'Cu3000200',
                colourIndex = 8;
            case 'Cu3000225',
                colourIndex = 4;
        end

        useColour = stdColours(colourIndex,:);

        %Identify wires and substrates corresponding the parameters chosen
    includeWire = true(size(DataStruct.bondType));
    includeWire = includeWire & ...
(strcmpi(wire{c}, 'all') | strcmpi(DataStruct.wire, wire{c}));
    if isnumeric(BDC{c})
        includeWire = includeWire & DataStruct.BDC == BDC{c};
    end
```

```
    includeWire = includeWire & strcmpi(DataStruct.bondType, bondType{c});

    includeSubst = any(includeWire, 2);
    includeSubst = includeSubst & ...
DataStruct.thickness == thickness(c);
    includeSubst = includeSubst & ...
DataStruct.cleaned == cleaned(c);
    includeSubst = includeSubst & ...
DataStruct.conditioned == conditioned(c);
    includeSubst = includeSubst & ...
DataStruct.temp == temp(c);
    includeSubst = includeSubst & ...
strcmpi(DataStruct.encapsulant, encapsulant{c});

    for i = 1:length(includeSubst)
        includeWire(i,:) = includeSubst(i) & includeWire(i,:);
    end

    for k = 1:length(level)
        timek = squeeze(DataStruct.failTimeInterp(:,:,k));
        censk = squeeze(DataStruct.cens(:,:,k));
        time = timek(includeWire);
        cens = censk(includeWire);

        timeVec = time(:);
        censVec = cens(:);

        if ~all(censVec)
            %Kaplan-Meier Estimate with Greenwood confidence bounds
            [f, x, fLo, fUp] = ecdf(timeVec, 'censoring', censVec, ...
'alpha', 0.05);
            medianIndex = find(f > 0.5, 1, 'first');
            if isempty(medianIndex)
                medianFailTime(c, k) = inf;
            else
                medianFailTime(c, k) = x(medianIndex);
            end
```

```
            % Find confidence bounds for degradation times
            lowerIndex = find(fLo > 0.5, 1, 'first');
            if isempty(lowerIndex)
                lowerFailTime(c, k) = nan;
            else
                lowerFailTime(c, k) = x(lowerIndex);
            end

            upperIndex = find(fUp > 0.5, 1, 'first');
            if isempty(upperIndex)
                upperFailTime(c, k) = nan;
            else
                upperFailTime(c, k) = x(upperIndex);
            end
        else
            medianFailTime(c, k) = inf;
            lowerFailTime(c, k) = inf;
            upperFailTime(c, k) = inf;
        end
    end

    % Plot Kaplan-Meier result with error bars
    h(c) = plot(level,  medianFailTime(c, :), marker{c}, ...
'LineWidth', width(c), 'Color', useColour);

    H = shadedErrorBar(level, medianFailTime(c, :), ...
[lowerFailTime(c, :) - medianFailTime(c, :); ...
medianFailTime(c, :) - upperFailTime(c, :)], ...
{marker{c}, 'color', useColour, 'linewidth', width(c)}, 1);

    set(H.mainLine, 'LineWidth', width(c));

end

%Add legend
if ~isempty(legendStr)
    legh = legend(h, legendStr, 'Location', 'NortheastOutside');
    if ~strcmp(legendTitle, '')
```

```
        title(legh, legendTitle, 'FontWeight', 'normal');
    end
end
xlabel({'Median Resistance Change', 'of Wire Bond Pairs', ...
'[% of Initial Mean]'});
ylabel('Time [h]');
set(gca, 'xlim', [0 20]);

%Interchange axes for more intuitive presentation
view([90 -90]);
```

C.5 Estimate Activation Energy Using Accelerated Failure Time Model File: FailureRegression.m

This code is used to estimate activation energies from bond failure times, as in Section 4.6. Here, PCC bonds on 3000 nm Al without encapsulation are used as an example.

```
condList = 1:100; % Range of failure conditions to be used (x10)
showTable = false;

% dist = 'weibull';
dist = 'lognormal';

% Plot display options
legendTitle = 'Pad Al Thickness';
legendStr = {'3000 nm'};
colour = ['std'];
marker = {'-'};
width = [3];

% Choose samples to be plotted
thickness = [3000];
cleaned = [true];
conditioned = [false];
encapsulant = {'None'};
wire = {'PCC'};
BDC = {'all'};
bondType = {'Al'};

for c = 1:size(thickness, 1)

    %Choose plot colours
    if strcmp(colour(c,:), 'std')
        colourStr = [wire{c} num2str(thickness(c)) '200'];

stdColours = ...
    [176,0,0;   0,176,0;    0,0,255;            0,176,176;
```

```
135,0,0;    0,135,0;    73,73,255;          0,135,135;
85,0,0;     0,85,0;     132,132,255;        0,85,85]/255;

    switch colourStr
        case 'PCC800175',
            colourIndex = 10;
        case 'PCC800200',
            colourIndex = 6;
        case 'PCC800225',
            colourIndex = 2;
        case 'PCC3000175',
            colourIndex = 11;
        case 'PCC3000200',
            colourIndex = 7;
        case 'PCC3000225',
            colourIndex = 3;
        case 'Cu800175',
            colourIndex = 9;
        case 'Cu800200',
            colourIndex = 5;
        case 'Cu800225',
            colourIndex = 1;
        case 'Cu3000175',
            colourIndex = 12;
        case 'Cu3000200',
            colourIndex = 8;
        case 'Cu3000225',
            colourIndex = 4;
    end

    useColour = stdColours(colourIndex,:);
else
    useColour = colour(c,:);
end

% Identify samples matching description above
includeWire = true(size(DataStruct.bondType));
includeWire = includeWire & (strcmpi(wire{c}, 'all') ...
```

```
| strcmpi(DataStruct.wire, wire{c}));
    if isnumeric(BDC{c})
        includeWire = includeWire & DataStruct.BDC == BDC{c};
    end
    includeWire = includeWire & strcmpi(DataStruct.bondType, bondType{c});

    includeSubst = any(includeWire, 2);
    includeSubst = includeSubst & ...
DataStruct.thickness == thickness(c);
    includeSubst = includeSubst & ...
DataStruct.cleaned == cleaned(c);
    includeSubst = includeSubst & ...
DataStruct.conditioned == conditioned(c);
    includeSubst = includeSubst & ...
strcmpi(DataStruct.encapsulant, encapsulant{c});
    includeSubst = includeSubst & ...
DataStruct.temp >= 175;

    for i = 1:length(includeSubst)
        includeWire(i,:) = includeSubst(i) & includeWire(i,:);
    end
    % Identify failure times
    time1 = squeeze(DataStruct.failTimeInterp(:,:,1));
    time1 = time1(includeWire);

    % Identify covariate values
    tempByWire = repmat(DataStruct.temp, size(includeWire, 2));
    tempVec = tempByWire(includeWire);
    arrCoeff = 1.602E-19./(1.38E-23*(273.15 + tempVec));
    arrCoeff = arrCoeff(~isnan(time1));

    for k = condList
        timek = squeeze(DataStruct.failTimeInterp(:,:,k));
        censk = squeeze(DataStruct.cens(:,:,k));
        time = timek(includeWire);
        cens = censk(includeWire);

        cens = cens(~isnan(time));
```

```
        time = time(~isnan(time));

        % Fit AFT model
        [param(k, :), cov, se(k, :, :), ci(k, :, :), z, p] =...
 aft(time, [ones(length(time), 1) arrCoeff],...
 cens, dist, [], [], [], showTable);
    end

    % Plot activation energy as function of failure condition
        a = param(condList, 2);
        x = 0.1*(condList)';
        figure;
        hold on;
        h1 = shadedErrorBar(x, a, ...
[(a - ci(:, 2, 1))'; (ci(:, 2, 2) - a)'], ...
{'color', useColour, 'linestyle', marker{c}}, 1);
        line(c) = h1.mainLine;

        ylabel('Activation Energy (eV)');
        xlabel({'Resistance Change', '(% of Initial Mean)'});

end

% Add legend to plot
figure;
legH = legend(line, legendStr, 'Location', 'NorthEastOutside');
title(legH, legendTitle, 'FontWeight', 'normal');
```

C.6 Assess Quality of Accelerated Failure Time Model Fitting File:AssessFit.m

This code generates plots of transformed residuals, used to assess the quality of fit of an accelerated failure time model.

```
failCond = 10;

% dist = 'weibull';
dist = 'lognormal';

% Visual elements of plot
legendTitle = 'Material';
legendStr = {'PCC', 'Cu'};
legendStr = [legendStr 'Ideal'];

colour = ['std'; 'std'];
marker = {'-', '--'};
width = [2 2];

% Choose sample groups to assess
thickness = [800 800];
cleaned = [true true];
conditioned = [false false];
encapsulant = {'Silicone', 'Silicone'};

wire = {'PCC', 'Cu'};
BDC = {'all', 'all'};
bondType = {'Al', 'Al'};
dist = 'lognormal';

for k = failCond
    figure;
    hold on;
    line = [];

    %Choose plot colours
    for c = 1:size(colour, 1)
```

```
        if strcmp(colour(c,:), 'std')
            colourStr = [wire{c} num2str(thickness(c)) '200'];

stdColours = ...
    [176,0,0;   0,176,0;    0,0,255;            0,176,176;
    135,0,0;    0,135,0;    73,73,255;          0,135,135;
    85,0,0;     0,85,0;     132,132,255;        0,85,85]/255;

            switch colourStr
                case 'PCC800175',
                    colourIndex = 10;
                case 'PCC800200',
                    colourIndex = 6;
                case 'PCC800225',
                    colourIndex = 2;
                case 'PCC3000175',
                    colourIndex = 11;
                case 'PCC3000200',
                    colourIndex = 7;
                case 'PCC3000225',
                    colourIndex = 3;
                case 'Cu800175',
                    colourIndex = 9;
                case 'Cu800200',
                    colourIndex = 5;
                case 'Cu800225',
                    colourIndex = 1;
                case 'Cu3000175',
                    colourIndex = 12;
                case 'Cu3000200',
                    colourIndex = 8;
                case 'Cu3000225',
                    colourIndex = 4;
            end

            useColour = stdColours(colourIndex,:);
        else
            useColour = colour(c,:);
```

```
        end

        % Identify samples to be included
        includeWire = true(size(DataStruct.bondType));
        includeWire = includeWire & (strcmpi(wire{c}, 'all') ...
| strcmpi(DataStruct.wire, wire{c}));
        if isnumeric(BDC{c})
            includeWire = includeWire & DataStruct.BDC == BDC{c};
        end
        includeWire = includeWire & ...
strcmpi(DataStruct.bondType, bondType{c});

        includeSubst = any(includeWire, 2);
        includeSubst = includeSubst & ...
DataStruct.thickness == thickness(c);
        includeSubst = includeSubst & ...
DataStruct.cleaned == cleaned(c);
        includeSubst = includeSubst & ...
DataStruct.conditioned == conditioned(c);
        includeSubst = includeSubst & ...
strcmpi(DataStruct.encapsulant, encapsulant{c});
        includeSubst = includeSubst & ...
DataStruct.temp >= 175;

        for i = 1:length(includeSubst)
            includeWire(i,:) = includeSubst(i) & includeWire(i,:);
        end

        % Identify covariate values
        tempByWire = repmat(DataStruct.temp, size(includeWire, 2));
        tempVec = tempByWire(includeWire);
        arrCoeff = 1.602E-19./(1.38E-23*(273.15 + tempVec));

        % Retreive failure times, censoring indicators
        timek = squeeze(DataStruct.failTimeInterp(:,:,k));
        censk = squeeze(DataStruct.cens(:,:,k));
        time = timek(includeWire);
        cens = censk(includeWire);
```

```
        if sum(isnan(time)) > 0
            disp([num2str(sum(isnan(time))) ' omitted']);
        end
        arrCoeff = arrCoeff(~isnan(time));
        cens = cens(~isnan(time));
        time = time(~isnan(time));

        % Fit AFT model
        [param, cov, se, ci, z, p] = aft(time, ...
[ones(length(time), 1) arrCoeff],...
 cens, dist, [], [], [], false);

        % Calculate residual
        z = (log(time) - param(1) - param(2)*arrCoeff)/param(3);
        [S, zS, SLo, SUp] = ecdf(z, 'censoring', cens, ...
'function', 'survivor');

        % Plot transformed residuals
        if strcmp(dist, 'lognormal');
            newLine = plot(zS, norminv(1-S), 'color', useColour, ...
'linestyle', marker{c});
            xlabel('Residual (z)');
            ylabel('\Phi^{-1}(1-S(z))');
            line = [line newLine];
        elseif strcmp(dist, 'weibull')
            newLine = plot(zS, log(-log(S)), 'color', useColour, ...
'linestyle', marker{c});
            xlabel('Residual (z)');
            ylabel('log(-log(S(z)))');
            line = [line newLine];
        end

        % Plot ideal line for comparison
        x = get(gca, 'xlim');
        y = get(gca, 'ylim');
        refLineH = plot([x(1) x(2)], [x(1) x(2)], 'k:');
        line = [line refLineH];
```

```
        % Add legend
        [legH] = legend(line, legendStr, 'Location', 'NorthWest');
        title(legH, legendTitle, 'FontWeight', 'normal');
    end
end
```

C.7 Extrapolate Lifetimes from Accelerated Failure Time Model File: LifetimeExtrapolation.m

This code is used to generate the extrapolated lifetime estimates in Section 4.11.

```
failCond = 10; %failure condition x10
extrapFactor = 100./failCond;

% Plot options
legendStr = {'50 %', '1 ppm', '12000 h'};
showTable = false;
survProb = [0.5 (1 - 1E-6)];
colour = 'std';

% dist = 'weibull';
dist = 'lognormal';

% Choose sample group
thickness = [800];
cleaned = [true];
conditioned = [false];
encapsulant = {'832HT'};
wire = {'Cu'};
BDC = {'all'};
bondType = {'Al'};

T1ppm = nan(length(survProb), length(failCond));
T50 = nan(length(survProb), length(failCond));

for k = 1:length(failCond)
    figure;
    for c = 1:size(colour, 1)

        % set up plot colours
        colourStr = [wire{c} num2str(thickness(c)) '225'];
```

```
stdColours = ...
    [176,0,0;   0,176,0;    0,0,255;            0,176,176;
    135,0,0;    0,135,0;    73,73,255;          0,135,135;
    85,0,0;     0,85,0;     132,132,255;        0,85,85]/255;

switch colourStr
    case 'PCC800175',
        colourIndex = 10;
    case 'PCC800200',
        colourIndex = 6;
    case 'PCC800225',
        colourIndex = 2;
    case 'PCC3000175',
        colourIndex = 11;
    case 'PCC3000200',
        colourIndex = 7;
    case 'PCC3000225',
        colourIndex = 3;
    case 'Cu800175',
        colourIndex = 9;
    case 'Cu800200',
        colourIndex = 5;
    case 'Cu800225',
        colourIndex = 1;
    case 'Cu3000175',
        colourIndex = 12;
    case 'Cu3000200',
        colourIndex = 8;
    case 'Cu3000225',
        colourIndex = 4;
end

% Identify samples matching specified conditions
includeWire = true(size(DataStruct.bondType));
includeWire = includeWire & (strcmpi(wire{c}, 'all') ...
    | strcmpi(DataStruct.wire, wire{c}));
if isnumeric(BDC{c})
    includeWire = includeWire & DataStruct.BDC == BDC{c};
```

```
end
includeWire = includeWire & ...
    strcmpi(DataStruct.bondType, bondType{c});

includeSubst = any(includeWire, 2);
includeSubst = includeSubst & ...
    DataStruct.thickness == thickness(c);
includeSubst = includeSubst & ...
    DataStruct.cleaned == cleaned(c);
includeSubst = includeSubst & ...
    DataStruct.conditioned == conditioned(c);
includeSubst = includeSubst & ...
    strcmpi(DataStruct.encapsulant, encapsulant{c});
includeSubst = includeSubst & ...
    DataStruct.temp >= 175;

for i = 1:length(includeSubst)
    includeWire(i,:) = includeSubst(i) & includeWire(i,:);
end

% Identify covariates
tempByWire = repmat(DataStruct.temp, size(includeWire, 2));
tempVec = tempByWire(includeWire);
arrCoeff = 1.602E-19./(1.38E-23*(273.15 + tempVec));

% Retreive failure times, censoring indicators
timek = squeeze(DataStruct.failTimeInterp(:,:,failCond(k)));
censk = squeeze(DataStruct.cens(:,:,failCond(k)));
time = timek(includeWire);
cens = censk(includeWire);

arrCoeff = arrCoeff(~isnan(time));
cens = cens(~isnan(time));
time = time(~isnan(time));

% Fit AFT model
[param, cov, se, ci, z, p] = ...
    aft(time, [ones(length(time), 1) arrCoeff], ...
```

```
    cens, dist, [], [], [], showTable);
numCens(failCond(k)) = sum(cens);

g0 = param(1);
g1 = param(2);
tau = param(3);

T = 100:0.1:225;
evalArr = 1.602E-19 ./ ((273.15 + T) * 1.38E-23);

for j = 1:length(survProb)

    % Extrapolate AFT model
    if strcmp(dist, 'lognormal')
        y = tau*norminv(1-survProb(j)) + g0 + g1*evalArr;
    elseif strcmp(dist, 'loglogistic')
        y = tau*log(1/survProb(j) - 1)+ g0 + g1*evalArr;
    elseif strcmp(dist, 'weibull')
        y = tau*log(-log(survProb(j))) + g0 + g1*evalArr;
    end
    [h(j)] = semilogy(T, extrapFactor(k)*exp(y)/365/24, '-', ...
        'color', stdColours(colourIndex+(j-1)*8,:));
    hold on;
    ylabel('Time [a]');
    xlabel('Temperature [C]');

    % Calculate confidence intervals for extrapolated lifetimes
    ySE = nan(size(y));
    for i = 1:length(evalArr)
        ySE(i) = sqrt([1 evalArr(i) norminv(1-survProb(j))] * ...
            cov * [1; evalArr(i); norminv(1-survProb(j))]);
    end
    yUpper = y + 1.96*ySE;
    yLower = y - 1.96*ySE;

    % Plot extrapolated lifetimes
    semilogy(T, extrapFactor(k)*exp(yUpper)/365/24, '--', ...
        'color', stdColours(colourIndex+(j-1)*8,:));
```

```
            semilogy(T, extrapFactor(k)*exp(yLower)/365/24, '--', ...
                'color', stdColours(colourIndex+(j-1)*8,:));

            % Identify maximum temperatures
            TIndex = find(extrapFactor(k)*exp(y) > 12000, 1, 'last');
            if ~isempty(TIndex)
                T1ppm(j, k) = T(TIndex);
            end

            TIndex = find(extrapFactor(k)*exp(y) > 12000, 1, 'last');
            if ~isempty(TIndex)
                T50(j, k) = T(TIndex);
            end

        end
    end

    xLim = [90 235];
    yLim = [1E-2 4000];
    set(gca, 'xlim', xLim);
    set(gca, 'ylim', yLim);
    set(gca, 'ytick', 10.^(-2:3));
    set(gca, 'yticklabel', {'0.01', '0.1', '1', '10', '100', '1000'});
    semilogy([T1ppm(2,k) T1ppm(2,k)], [yLim(1) 12000/365/24], 'k:');
    semilogy([T50(1,k) T50(1,k)], [yLim(1) 12000/365/24], 'k:');
    refLineH = plot([xLim(1) xLim(2)], [12000 12000]/365/24, 'k:');
    legH = legend([h refLineH], [legendStr, '12000 h'], ...
        'Location', 'Best');
    title(legH, 'Fail Prob.', 'FontWeight', 'normal');
end
```